Quantum Superpositions of Persistent Josephson Currents

Quantum Superpositions of Persistent Josephson Currents

Proefschrift

ter verkrijging van de graad van doctor
aan de Technische Universiteit Delft,
op gezag van de Rector Magnificus prof. ir. K. F. Wakker,
voorzitter van het College voor Promoties,
in het openbaar te verdedigen

op maandag 24 september 2001 te 13.30 uur

door

Caspar Heimen van der WAL

natuurkundig ingenieur
geboren te Hengelo (Ov.).

Dit proefschrift is goedgekeurd door de promotor:

Prof. dr. ir. J. E. Mooij

Samenstelling van de promotiecommissie:

Rector Magnificus, voorzitter
Prof. dr. ir. J. E. Mooij, Technische Universiteit Delft, promotor
Dr. C. J. P. M. Harmans, Technische Universiteit Delft, toegevoegd promotor
Prof. S. Lloyd, M.I.T., Verenigde Staten
Prof. A. J. Leggett, University of Illinois, Urbana, Verenigde Staten
Prof. J. Clarke, University of California, Berkeley, Verenigde Staten
Prof. Dr. G. B. J. Schön, Universität Karlsruhe, Duitsland
Dr. D. Esteve, C.E.A., Saclay, Frankrijk
Prof. dr. ir. L. P. Kouwenhoven, Technische Universiteit Delft

Het onderzoek beschreven in dit proefschrift is financieel ondersteund door de stichting voor Fundamenteel Onderzoek der Materie (FOM).

Published and distributed by: DUP Science

DUP Science is an imprint of
Delft University Press
P.O. Box 98
2600 MG Delft
The Netherlands
Telephone: +31 15 27 85 678
Telefax: + 31 15 27 85 706
E-mail: DUP@Library.TUDelft.NL

ISBN 90-407-2193-9

Keywords: Josephson effect, macroscopic quantum coherence, quantum computation

Printed in the Netherlands

Preface

This thesis presents results from four and a half years experimental research on Josephson quantum circuits in the group of Hans Mooij at Delft University of Technology. In December 1996, I started as a Ph.D. student in this group in a new project entitled *Quantum computation with solid state devices*. The project aimed at investigating whether small Josephson tunnel-junction devices could be used as basic building blocks for a quantum computer. It was financially supported by the Dutch Foundation for Fundamental Research on Matter (FOM). For fabrication of the Josephson junction circuits the cleanroom facilities of the Delft Institute for Micro Electronics and Submicron Technology (DIMES) were used. At a later stage efforts were worked out in collaboration with the groups of Terry Orlando, Seth Lloyd and Leonid Levitov at MIT. The project grew with the arrival of a few more Ph.D. students and postdocs, when the Delft *DIOC on Novel computation structures based on quantum devices* and the European *SQUBIT* program were started.

In 1996, the field of quantum computation was quickly gaining momentum after Peter Shor had discovered in 1994 that a quantum computer would be able to factorize large numbers exponentially faster than a classical computer. However, it was already clear at that point that realizing a large quantum computer would be very difficult, if not impossible. The scientific community was very uncertain about the questions whether, and how a large-scale quantum computer could be built. Since then, there has been a lot of progress in the field of quantum computation, but the basic questions about the feasibility of quantum computation are still very open today. This uncertainty has led to a wide variety of proposals for research on realizing a quantum computer. An important advantage of implementing a quantum computer in microfabricated solid-state structures is, that the step from a basic unit to a large-scale integrated computer would be much easier than for many other proposals. This thesis reports on research that investigates whether small superconducting tunnel-junction circuits can form the required basic unit for a solid-state quantum computer. In the late 1980's and

first half of the 1990's, the group of Hans Mooij has contributed significantly to research on mesoscopic tunnel-junction circuits. This provided a good basis for experimental work that aimed at demonstrating and accurately controlling quantum coherent dynamics of such circuits. While this research was inspired by the goal to realize a quantum computer, the results are often also very interesting for fundamental research on the validity of quantum mechanics and decoherence. The results in this thesis are therefore not presented with a strong emphasis on quantum computation.

What I present in the following chapters is the result of work that I did together with students, technicians and other colleagues. I like to use this preface to thank all the people that contributed to this work, and colleagues that created a pleasant and inspiring atmosphere to work in. I enjoyed working in the Quantum Transport group very much.

First of all, I thank Hans Mooij, he has been a very stimulating Ph.D. advisor who gave me a lot of freedom. It was very motivating that he was as excited about our research as I was. I benefited and learned a lot from his incredible intuition, when judging which long-term research goals were particularly interesting. During my Ph.D. work, Kees Harmans became a second Ph.D. advisor for me. With a lot of pleasure I recall many interesting discussions while working together on the new fridge. They were very important for creating a link between ideas about quantum physics, and getting results on the oscilloscope.

I enjoyed being the advisor of five M.Sc. students: I like to thank Hans Cool, Paul Kuiper, Alexander ter Haar (now a Ph.D. student in our team), Thomas Ooms and Stijn Steenbrink for their friendship an hard work. I also thank Frank Wilhelm, a theorist who had the courage to work as a postdoc in our experimental group, for learning me a lot while working out questions about the influence of the measurement process in our experiments. Many other colleagues in Delft contributed to this work with help, critical questions, stimulating discussions, and being friends during and after work. I like to mention Leo Kouwenhoven, Peter Hadley, Herre van der Zant, Ton Wallast, Alexander van Oudenaarden, Milena Grifoni, David Dixon, Pieter Heij, Hannes Majer, Adrian Lupaşcu, Irinel Chiorescu, Tjerk Oosterkamp, Sander Tans, Henk Postma, Arnold Storm, Liesbeth Venema, Alberto Morpurgo, Sara Cronenwett, Lucas van Gorkom, Allard Katan, Marlies Goorden, and the visiting researchers Kostya Likharev, Michel Devoret, Hirotaka Tanaka, Yoshihiro Shimazu and Lin Tian.

The support from several technicians in our Department has been indispens-

able for getting results. In particular, I like to mention Raymond Schouten. He deserves a lot of credit for designing and building the low-noise electronics that were a crucial part of the measurement setups. Wim Schot and Willem den Braver have provided a steady supply of liquid helium and nitrogen, and contributed significantly to setting up the new sorption-pump dilution refrigerator. Due to Bram van der Enden I never learned how to wire-bond my own sample, and he made sure that the setup for evaporating thin layers was running. I also like to thank Leo Lander, Bram Huis, Jan de Looff (stycast tricks) and Leo Dam for their work and advice on various occasions. I am indebted to the people at DIMES, in particular to Emile van der Drift, Anja van Langen, Arnold van Run and Bert de Groot, for support and advice on sample fabrication.

In our collaboration with MIT, I worked a lot with Terry Orlando. I learned a lot from his insights in Josephson physics, and like to thank him for all his help. During my visits to MIT, I enjoyed working with the members of the Orlando group, and I am very grateful for their hospitality. I also thank Seth Lloyd and Leonid Levitov at MIT for their time and interest in my research. In the Netherlands, I learned a lot on frequent visits to Philip Stamp in Utrecht, and the NMR group of Jan Schmidt in Leiden. I also like to thank Jan Schmidt and Jos Disselhorst here once more for lending microwave material to us. While traveling, I had discussions with Yasunobu Nakamura, David DiVincenzo, Daniel Esteve, Orly Alter and Yoshihisa Yamamoto, that were of great value to me.

It has been a pleasure for me to experience that not only physicists, but also friends and family can get excited about what happens at a few milliKelvin. Most notably, I like to thank my parents for always following my work with great interest. I also like to thank my partner Annet Jantien for her support. When recalling at this moment the years of my Ph.D. research, the strongest memory is that you have always been my best friend.

Caspar van der Wal
Delft, June 2001

Contents

Chapter 1

Introduction

Josephson tunnel junctions are ideal elements for research on quantum mechanical behavior of electrical circuits [1]. With modern microfabrication techniques, junctions can be realized with well-defined properties. Residual dissipative effects of the junctions freeze out at milliKelvin temperatures, and the dynamics of the junctions can be extremely underdamped. Furthermore, a Josephson tunnel junction is a non-linear circuit element. This can be used to engineer systems with an effective Hamiltonian which is, for example, equivalent to that of a spin-$\frac{1}{2}$ particle, or a particle in a periodic potential. The non-linearity of such systems does not only bring interesting physics and engineering possibilities. It is also convenient for the experimental physicist: If the non-linear circuits behave quantum mechanically, the average values of the charge and magnetic-flux coordinates do not follow the classical equations of motion. Quantum effects can thus be identified by direct measurements of the average charge or flux coordinates.

During the last twenty years several groups have convincingly demonstrated quantum effects in Josephson junction circuits [2, 3]. For example, the situation in which a flux coordinate of a circuit (often represented by a phase coordinate of a Josephson junction) is trapped in a metastable well has been extensively studied. In these experiments, decay of the metastable state by tunneling through a barrier has been observed [4, 5, 6, 7] as well as discrete energy levels in the metastable well [5, 6, 8, 9]. In circuits with a small, low-capacitance superconducting island, superpositions of single-Cooper-pair states have been observed [10, 11], and the Heisenberg uncertainty relation for charge and Josephson-phase degrees of freedom has been directly demonstrated [12]. Recently, Nakamura *et al.* reported quantum coherent oscillations of the charge on such a small superconducting island [14]. However, while these results convincingly demonstrate that quantum mechanical effects like tunneling play a role, the behavior of the

circuits is in all these experiments also strongly influenced by their coupling to degrees of freedom in the environment. In particular, the wiring that is connected to the circuit for experimental access forms an impedance that usually dominates the damping of the circuit. In many cases the material properties of the substrate below the sample and other parts of the sample volume play a role as well. In this respect, the influence of offset charges and $1/f$ charge noise in the experiments with single-Cooper-pair devices is notorious. In circuits with closed loops, the noise from flux that is trapped in nearby superconducting layers is a known problem. In experiments on Josephson quantum circuits, the observed phenomena are usually the result a complicated mixture of quantum effects in the circuits, dissipative effects in the environment, and the influence of environmental fluctuations and noise.

When comparing the research on Josephson quantum circuits to other fields that study quantum systems, it is clear that the level of experimental control over the quantum states of Josephson systems is far from what has been realized in some other fields. For example in cavity quantum-electrodynamics experiments with atoms [15], experiments with trapped ions [17], and non-linear optics [18], the coupling to the environment is very weak. In these experiments the state of the quantum system can be accurately controlled, and is for a long time accurately described by the Schrödinger equation, applied to the Hamiltonian of the isolated system. In particular the recent experiments by Nakamura *et al.* [14] indicate that techniques for similar quantum-state control of Josephson junction circuits can be developed.

This thesis presents experimental research that aimed at investigating to what extent Josephson junction circuits can be used to realize well-defined and controllable quantum systems. In particular, the work aimed at realizing an artificial spin-$\frac{1}{2}$ system, that is very well decoupled from environmental noise. Such a system would be most appropriate for testing whether these circuits can have controlled quantum coherent dynamics, with a decoherence time that is much longer than the period of the quantum oscillations of the system. Ultimately, the question would be whether it is possible to realize arbitrary quantum coherent states in circuits with multiple coupled spin-$\frac{1}{2}$ systems (i. e. entangled states, similar to Einstein-Podolsky-Rosen states for pairs of spin-$\frac{1}{2}$ particles), and whether non-classical correlations can be demonstrated. These questions were inspired by three, partly overlapping research themes that are currently of interest in the scientific community.

First of all, this work aimed at contributing to research on quantum com-

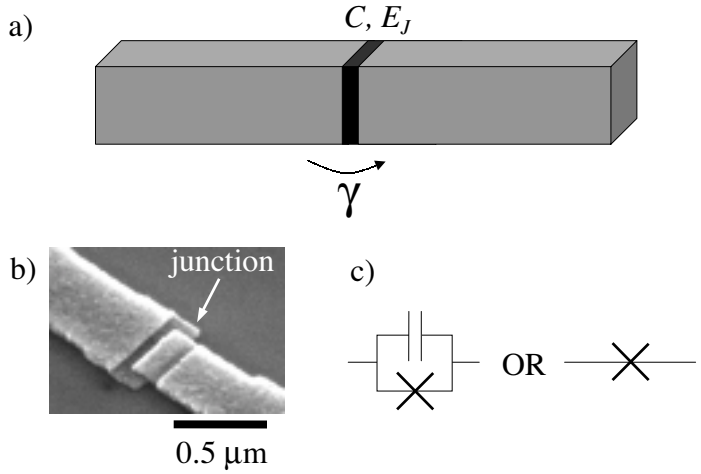

Figure 1.1: **a)** A Josephson junction consists of a thin oxide layer with a small area between two superconductors. It can be characterized by its capacitance C and Josephson coupling energy E_J. **b)** SEM picture of a Josephson junction fabricated with shadow-evaporation techniques. The arrow points to the place where two sequentially evaporated aluminum layers overlap. The layers are separated by a thin layer of aluminum oxide. **c)** The symbols used in circuit diagrams to represent a Josephson junction.

putation [16, 19, 20, 21]. If quantum coherent dynamics of Josephson junction circuits could be accurately controlled, these systems would be a promising candidate for realizing a quantum computer. The main advantage of an approach based on small Josephson junction circuits is that the technology for expanding such a system to a large-scale integrated computer is already available (Fig. 1.4 shows an example of a chip with 7,000 uncoupled quantum systems). For realizing a large quantum computer, it is desirable that the quantum bits (qubits) can be addressed individually by local control, and that qubit-qubit couplings can be controlled locally as well. Because the circuits are so much larger than quantum systems on the atomic scale, and, unlike e. g. photons, fixed in space, it is far more likely that this can be realized with Josephson circuits than with quantum systems of a much smaller size. However, the challenge here is to realize a good basic unit. The possibility to engineer and control these systems

at will goes along with the difficulty that it is very hard to decouple them from environmental noise.

Secondly, this study is of interest for research on macroscopic quantum coherence (MQC) [22]. MQC studies the consequences of extrapolating the laws of quantum mechanics to the macroscopic world, and follows directly from discussions on the Schrödinger cat paradox [23]. The current degrees of freedom of Josephson circuits are macroscopic, in the sense that they correspond to the center-of-mass motion of a very large number of microscopic charge carriers. The circuits that we used consist typically of tens of billions of aluminum atoms, and the number of Cooper pairs in the systems in the same range. Josephson junction circuits therefore rank among the best systems for testing the validity of quantum mechanics at a macroscopic scale.

Thirdly, it is very interesting that these devices are artificially fabricated quantum systems. With the technology that is applied, it is possible to engineer and control them in a wide parameter range, and to couple the systems in a controlled manner to environmental degrees of freedom. This allows for detailed research on the boundary between classical and quantum physics, and decoherence [24]. In particular, several decoherence phenomena are predicted for a macroscopic spin-$\frac{1}{2}$ system coupled to an oscillator bath [25], and a spin bath [26].

In the rest of this introductory chapter we will shortly outline the quantum physics of Josephson junction circuits, and introduce the experimental work on the two Josephson junction circuits that were studied in this research.

1.1 Josephson quantum circuits

The Josephson junction devices that are used in this research consist of micrometer-sized superconducting islands, that are interconnected by a Josephson tunnel junction: a thin insulating oxide layer between two superconductors (Fig. 1.1). We used aluminum circuits, with low-capacitance Al–Al_2O_3–Al tunnel junctions that were fabricated with electron-beam lithography and shadow evaporation techniques (for details see Ref. [27]).

The behavior of the Josephson junctions is in a first approximation determined by two macroscopic parameters. One is the junction capacitance C, which results from the parallel-plate geometry of the tunnel junctions. This capacitance dominates the capacitance between superconducting islands in circuits with Josephson junctions. For the simple circuit in Fig. 1.1a, the charge difference between the two islands (i. e. the charge on the junction capacitance) changes with $4e$ when

a single Cooper pair (with charge $2e$) tunnels from one island to the other. If the charge distribution were initially neutral, the tunnel event causes the circuit's electrostatic energy to increase with $(4e)^2/2C$. By convention, the energy scale for the charging effects in the circuits is defined as $E_C = e^2/2C$. For more complicated circuits, the electrostatic free energy can be adequately described with a capacitance-matrix formalism [28].

The second junction parameter is the junction's Josephson coupling energy E_J, which is a measure for the tunnel coupling between the two superconducting electrodes, and it determines the supercurrent that can flow through the junctions. For junctions that couple two BCS superconductors of the same type, $E_J = \frac{h}{8e^2 R_N}\Delta_s$, where Δ_s the superconducting gap and R_N the normal-state tunnel resistance of the junction. The supercurrent I_s through the junction is directly related to a phase coordinate of the junction, the gauge-invariant phase difference γ [3] (γ is in fact a flux coordinate, normalized to the superconducting flux quantum $\Phi_0 = \frac{h}{2e}$ [1]). The supercurrent $I_s = I_{co}\sin\gamma$, where $I_{co} = \frac{2e}{\hbar}E_J$ is the critical current of the junction. The Josephson coupling energy that is stored in the junction is $U_J = -E_J\cos\gamma$.

The charge and flux coordinates of circuits with Josephson junctions are conjugate variables in the sense of Hamiltonian mechanics. For example, for the simple circuit in Fig. 1.1a (isolated junction), current conservation gives $I_{co}\sin\gamma + C(dV/dt) = 0$, where V is the voltage across the junction. With the AC Josephson relation $V = \frac{\hbar}{2e}(d\gamma/dt)$, and after taking out a factor $(\frac{2e}{\hbar})$, this can be written as $E_J\sin\gamma + C(\frac{\hbar}{2e})^2(d^2\gamma/dt^2) = 0$. This is the equation of motion of a system with the Lagrangian $L = \frac{1}{2}C(\frac{\hbar}{2e})^2(d\gamma/dt)^2 + E_J\cos\gamma$. The charge difference between the two superconductors is the result of single Cooper pairs that tunnel through the junction. We therefore express the charge difference between the two superconductors as the number of Cooper pairs n on the capacitor, $-2en = CV$. The Hamiltonian of this system can then be written as $H = 4E_C n^2 - E_J\cos\gamma$, and the commutation relation $[\gamma, n] = i$ applies to these number and phase variables. The Josephson and charge effects are orthogonal: When the phase γ and the current in the junction are well-defined, the charge on the junctions has quantum fluctuations that are much larger than $2e$. Accordingly, states with a well-defined number of Cooper pairs on the islands, must have very large quantum fluctuations in the phase. In the intermediate regime, where E_J and E_C are of the same order, the eigen states of the system have comparable fluctuations in the charge and phase coordinates, and this regime is most interesting for research on quantum effects in Josephson circuits. Typical

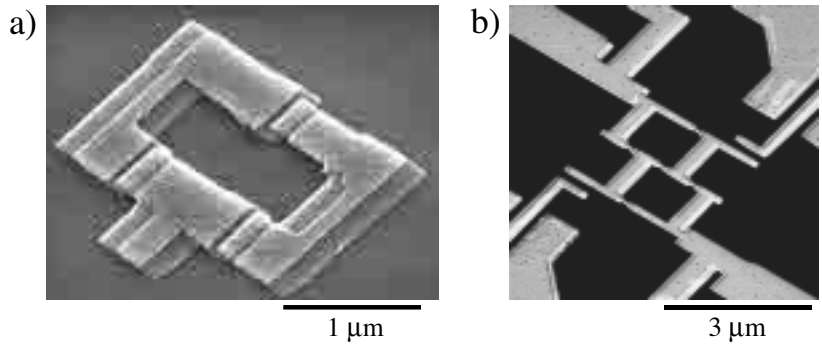

Figure 1.2: SEM pictures of the two Josephson junction circuits that have been investigated. **a)** A three-Josephson junction loop. Near a magnetic-flux bias of half a superconducting flux quantum this system has two stable classical persistent-current states of opposite polarity. The system is measured by coupling it inductively to an underdamped DC-SQUID (not present here). Microwave spectroscopy results show that this system has two low-energy quantum levels that are superpositions of the two classical persistent-current states. **b)** A small Josephson junction array with two loops. Near a flux bias of half a superconducting flux quantum this system has two stable classical persistent-current states, that correspond to the presence of a persistent current in one loop or the other loop. For a fixed flux bias, the currents of the two states flow in the same direction, but at a different location. Controlled superconducting single-charge effects are used to tune the ground-state quantum fluctuations in the array's phase and charge variables, and could be used to demonstrate a quantum superposition of the two persistent-current states.

values for E_J and E_C are close to 1 Kelvin, so that the level separation in the quantum systems is in the microwave range.

1.2 This work: Persistent-current systems

We performed experiments on two different small Josephson junction devices with closed loops, shown in Fig. 1.2. The first part of this thesis reports work on a three-Josephson junction loop (Fig. 1.2a). The last three chapters present results of experiments on a small two-dimensional Josephson junction array with two coupled loops (Fig. 1.2b). The two system have in common that they both carry

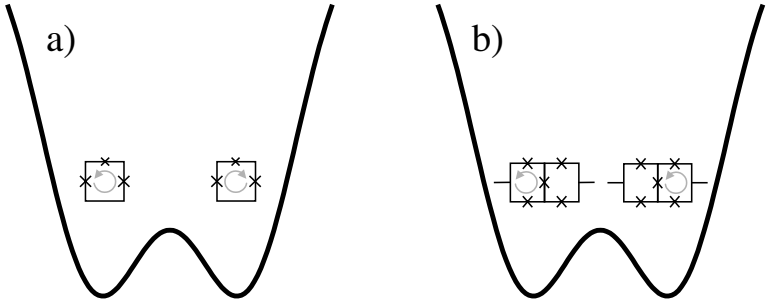

Figure 1.3: Schematic representation of the persistent-current states of the three-junction loop (a), and the small two-dimensional array (b). Close to a flux bias of $\frac{1}{2}\Phi_0$, the Josephson energy of these systems forms a double well potential, with minimums at different values of the gauge-invariant phase coordinates of the systems.

persistent currents when a small magnetic field is applied to the loops.

The persistent currents in the loops are a direct consequence of the fact that the phase of the superconducting order parameter must be single-valued on a closed loop. For a small loop with Josephson junctions, this is equivalent to the statement that the sum of the gauge-invariant phases of the junctions on the loop (all taken in the same direction) must equal $2\pi\Phi/\Phi_0$ (fluxoid quantization). Φ is here the total magnetic flux in the loop, i. e. the sum of the externally applied flux, and the flux that results from currents that flow in the loop. We worked on systems with micrometer-sized loops, and junctions with a critical current I_{co} of a few hundred nA or less. The self-generated flux is therefore very small in comparison to the flux quantum Φ_0, ($L_g I_{co} << \Phi_0$, where L_g the geometric inductance of the loop, which is approximately 1 pH per μm loop diameter). In this case, the externally applied flux is effectively equal to the total flux in the loop. Each independent condition for fluxoid quantization now acts as a constraint on the system's phase coordinates. As a consequence, the systems total Josephson energy $U_J = \sum_i -E_{J,i}\cos\gamma_i$ has for a non-zero magnetic flux in the loop minimums at non-zero values of the phases γ_i of the junctions (i is an index labeling the junctions). That is, the stable classical solutions in the Josephson potential U_J are states with a persistent current.

By engineering the values of the Josephson energy $E_{J,i}$, and by controlling the magnetic flux in the loop, the shape of the Josephson potential can thus be

controlled. For our two systems U_J forms a double well potential for flux values close to $\frac{1}{2}\Phi_0$ (Fig. 1.3). For the three-junction loop, the classical states at the bottoms of the two wells correspond to clockwise and counter-clockwise persistent currents in the loop. In the small array, the classical states at the bottoms of the two wells correspond to states with a persistent current running in only one of the two loops. Here the polarity of the two persistent-current states is the same, but the loop that carries the persistent current is different for the two states.

The three-Josephson junction loops were realized in the regime where the junctions' Josephson energy E_J was about a factor fifty larger than the charging energy E_C of the junctions. For this ratio of $E_J/E_C \approx 50$, a subtle balance is struck in this device. The system's charging effects, are still significant, and allow for quantum tunneling between two different stable persistent-current states. At the same time, the high ratio of E_J/E_C allows for engineering the system such that it is very insensitive to the influence of $1/f$ charge noise and offset charges in the solid-state environment of the loop. Making the system insensitive to offset charges was one of the main design criteria. Chapter 2 describes the physics of this system, and how it can possibly be applied as a quantum bit. Microwave spectroscopy experiments on this system are presented in Chapter 3. The experiments proof that the three-junction loop can behave as a quantum-two-level system, and that quantum superpositions of the two macroscopic persistent-current states occur in this system. Chapter 4 discusses the relaxation and dephasing rates that result from the measurement setup itself in experiments on Josephson persistent-current qubits (decoherence due to the measuring DC-SQUID, and on-chip control circuits). The experiments on the three-junction loop are performed on a single quantum system that is permanently coupled to a measurement apparatus. In such a setup there is obviously a conflict between the possibility of long quantum coherent behavior of the quantum system and an efficient measurement scheme. The development of measurement strategies where the meter can be effectively off during certain periods is discussed in Chapter 4.

An alternative approach for reducing the back action of the meter on the dynamics of the loops is shown in Fig. 1.4. This picture shows a chip with an ensemble of 7,000 loops, coupled to a single DC-SQUID magnetometer. Here an NMR like measurement scheme is employed: The meter is only weakly coupled to the loops, and the signal of an individual loop is too weak to be resolved by the measurement apparatus. Consequently, the back action from the meter is very low as well. The collective signal of synchronous dynamics of all 7,000 loops gives a signal that is strong enough to be detected. Preliminary results

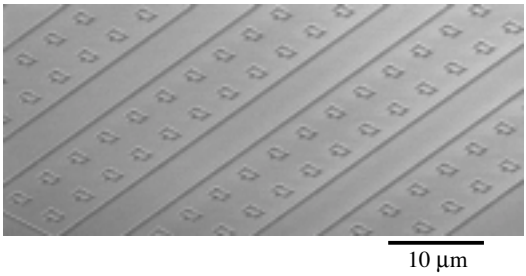

Figure 1.4: SEM picture of a chip with 7,000 Josephson junction loops inside the meandering lines of a large, damped gradiometer DC-SQUID. The coupling between the loops is here very weak (picture and sample by A. .C. Wallast and Y. Shimazu).

from this approach showed the collective reversal of the persistent currents in the loops when sweeping the flux bias in a window around $\frac{1}{2}\Phi_0$, and microwave-induced transitions to excited states [29]. This work on ensembles of loops is not addressed in this thesis.

The small two-dimensional arrays had $E_J/E_C \approx 1$. These devices are thereby very sensitive to offset charges. In the experiments on this device we used capacitively coupled gate electrodes to compensate the influence of offset charges, and for controlling the single-Cooper pair effects in this system. Chapter 5 discusses a study of controlled single-Cooper pair charging effects in this system, and presents the experimental techniques. This circuit has a self-dual geometry: It can be described as two coupled islands with a high charging energy, but also as two coupled loops that can carry a persistent current. The latter picture corresponds to that of an array, in which the meshes can contain a vortex. This array was used to study the duality between the charge and the vortex representation of Josephson junction arrays. The possibility to control both the magnetic-flux bias and the single-Cooper pair effects of this system, was used to tune the trade-off between quantum fluctuations in the phase and the charge in the ground state of this system. Chapter 6 presents how this could be used to demonstrate that superpositions of vortex and charge states occur in this system in a dual fashion. In Chapter 7, microwave spectroscopy experiments on this system are presented, which provide evidence for the excited quantum levels of the array.

References

[1] M. H. Devoret, in *Quantum fluctuations*, S. Reynaud, E. Giacobino, J. Zinn-Justin, Eds. (Elsevier Science, Amsterdam, 1997), pp. 351-386.

[2] For reviews on quantum effects in Josephson junction circuits see D. V. Averin, K. K. Likharev, in *Mesoscopic phenomena in solids*, edited by B. L. Al'tshuler, P. A. Lee, R. A. Webb (Elsevier, Amsterdam, Netherlands, 1991); *Single charge tunneling*, edited by H. Grabert, M. H. Devoret (Plenum Press, New York, 1992); *Macroscopic quantum phenomena and coherence in superconducting networks*, edited by C. Giovanella and M. Tinkham (World Scientific, Singapore, 1995); *J. Supercond.* **12**, (issue of December 1999).

[3] Text books with introductions to the physics of Josephson junctions are K. K. Likharev, *Dynamics of Josephson junctions and circuits* (Gordon and Breach Science Publishers, Philadelphia, 1984); T. P. Orlando, K. A. Delin, *Foundations of applied superconductivity* (Addison-Wesley, Reading, 1991); M. Tinkham, *Introduction to superconductivity* (McGraw-Hill, Inc., New York, ed. 2, 1996).

[4] For an interesting review on early results see K. K. Likharev, *Sov. Phys. Usp.* **26**, 87 (1983).

[5] J. M. Martinus, M. H. Devoret, J. Clarke, *Phys. Rev. B* **35**, 4682 (1987).

[6] John Clarke, Andrew N. Cleland, Michel H. Devoret, Daniel Esteve, John M. Martinus, *Science* **239**, 992 (1988).

[7] R. Rouse, S. Han, J. E. Lukens, *Phys. Rev. Lett.* **75**, 1614 (1995).

[8] S. Han, R. Rouse, J. E. Lukens, *Phys. Rev. Lett.* **76**, 3404 (1996).

[9] P. Silvestrini, V. G. Palmieri, B. Ruggiero, M. Russo, *Phys. Rev. Lett.* **79**, 3046 (1997).

[10] Y. Nakamura, C. D. Chen, J. S. Tsai, *Phys. Rev. Lett.* **79**, 2328 (1997).

[11] V. Bouchiat, D. Vion, P. Joyez, D. Esteve, M. H. Devoret, *Phys. Scr.* **T76**, 165 (1998).

[12] W. J. Elion, M. Matters, U. Geigenmuller, J. E. Mooij, *Nature* **371**, 594 (1994);

[13] M. Matters, W. J. Elion, J. E. Mooij, *Phys. Rev. Lett.* **75**, 721 (1995).

[14] Y. Nakamura, Yu. A. Pashkin, J. S. Tsai, *Nature* **398**, 786 (1999).

[15] See for example S. Haroche, *Phys. Today* **51**, 36 (July 1991).

[16] *Quantum computing*, edited by S. Braunstein (Wiley-VCH, Weinhein, 1999).

[17] For reviews on trapped ion experiments see R. J. Hughes *et al.* and D. H. Wineland *et al.* in Ref. [16], p. 23-84.

[18] See for example D. Bouwmeester *et al.*, *Nature* **390**, 575 (1997)

[19] For a discussion of design criteria for qubits, related to mesoscopic physics, see D. P. DiVincenzo in *Mesoscopic electron transport*, L. L. Sohn, L. P. Kouwenhoven, and G. Schon, Eds. (Kluwer Academic Publishers, Dordrecht, 1997), p. 657; quant-ph/0002077.

[20] For a review on solid-state qubits see Y. Makhlin, G. Schön, A. Shnirman, submitted to *Rev. Mod. Phys.* (2000); cond-mat/0011269.

[21] For a text book see M. A. Nielsen and I. L. Chuang, *Quantum computation and quantum information* (Cambridge University Press, Cambridge, 2000).

[22] A. J. Leggett, *Prog. Theor. Phys. Suppl.* **69**, 80 (1980); A. J. Leggett, A. Garg, *Phys. Rev. Lett.* **54**, 857 (1985); C. D. Tesche, *Phys. Rev. Lett.* **64**, 2358 (1990); The essays of A. Leggett and A. Shimony in *Quantum measurement: Beyond paradox*, R. A. Healey, G. Hellman, Eds. (University of Minnesota Press, Minneapolis, 1998), pp. 1-31; A. J. Leggett, *J. Supercond.* **12**, 683 (1999); T. Leggett, *Phys. World* **12**, 73 (December 1999).

[23] E. Schrödinger, *Naturwissenschaften* **23**, 807-812, 823-828, 844-849 (1935), reprinted in English in *Quantum theory and measurement*, edited by J. A. Wheeler and W. H. Zurek (Princeton, 1983).

[24] W. H. Zurek, *Phys. Today* **44**, 36 (October 1991).

[25] A. J. Leggett *et al.*, *Rev. Mod. Phys.* **59**, 1 (1987) and *Rev. Mod. Phys.* **67**, 725(E) (1995); M. Grifoni, P. Hänggi, *Phys. Rep.* **304**, 229 (1998).

[26] N. Prokof'ev, P. Stamp, *Rep. Prog. Phys.* **63**, 669 (2000); cond-mat/0001080.

[27] E. H. Visscher, S. M. Verbrugh, J. Lindeman, P. Hadley, J. E. Mooij, *Appl. Phys. Lett.* **66**, 305 (1995).

[28] P. Lafarge, Ph.D. thesis, Université Paris 6 (1993), Appendix 1.

[29] Y. Shimazu and A. C. Wallast, internal report, Delft University of Technology (2000).

Chapter 2

Josephson Persistent-Current Qubit

Abstract

A qubit has been designed that can be fabricated with conventional electron-beam lithography and is suited for integration into a large quantum computer. The qubit consists of a micrometer-sized loop with three or four Josephson junctions; the two qubit states have persistent currents of opposite direction. Quantum superpositions of these states are obtained by pulsed microwave modulation of the enclosed magnetic flux by currents in control lines. A superconducting flux transporter allows for controlled transfer between qubits of the flux that is generated by the persistent currents, leading to entanglement of qubit information.

In a quantum computer, information is stored on quantum variables such as spins, photons or atoms [1, 2, 3, 4]. The elementary unit is a two-state quantum system called a qubit. Computations are performed by the creation of quantum superposition states of the qubits and by controlled entanglement of the information on the qubits. Quantum coherence must be conserved to a high degree during these operations. For a quantum computer to be of practical value, the number of qubits must be at least 10^4. Qubits have been implemented in cavity quantum electrodynamics systems [5], ion traps [6] and nuclear spins of large numbers of identical molecules [7]. Quantum coherence is high in these systems, but it seems difficult or impossible to realize the desired high number of interacting qubits. Solid-state circuits lend themselves to large scale integration, but the multitude of quantum degrees of freedom leads in general to short decoherence times. Proposals have been put forward for future implementation of qubits with spins of individual donor atoms in silicon [8], with spin states in quantum

This chapter is based on Refs. 2 and 3 on p. 111.

dots [9] and with d-wave superconductors [10]; here the technology for practical realization still needs to be developed.

In superconductors all electrons are condensed in the same macrosopic quantum state, separated by a gap from the many quasiparticle states. This gap is a measure for the strength of the superconducting effects. Superconductors can be weakly coupled with Josephson tunnel junctions (regions where only a thin oxide separates them). The coupling energy is given by $E_J(1-\cos\gamma)$, where the Josephson energy E_J is proportional to the gap of the superconductors divided by the normal-state tunnel resistance of the junction, and γ is the gauge-invariant phase difference of the order parameters. The current through a Josephson junction is equal to $I_{co}\sin\gamma$ with $I_{co} = \frac{2e}{\hbar}E_J$. In a Josephson junction circuit with small electrical capacitance, the numbers of excess Cooper pairs on islands n_i, n_j and the phase differences γ_i, γ_j are related as non-commuting conjugate quantum variables [11]. The Heisenberg uncertainty between phase and charge, and the occurrence of quantum superpositions of charges as well as phase excitations (vortex-like fluxoids) have been demonstrated in experiments [12, 13, 14]. Coherent charge oscillations in a superconducting quantum box have recently been observed [15]. Qubits for quantum computing based on charge states have been suggested [16, 17, 18, 19]. However, in actual practice fabricated Josephson circuits exhibit a high level of static and dynamic charge noise due to charged impurities. In contrast, the magnetic background is clean and stable. Here, we present the design of a qubit with persistent currents of opposite sign as its basic states. The qubits can be driven individually by magnetic microwave pulses; measurements can be made with superconducting magnetometers (SQUIDs). They are decoupled from charges and electrical signals, and the known sources of decoherence allow for a decoherence time of more than 1 ms. Switching is possible at a rate of 100 MHz. Entanglement is achieved by coupling the flux, that is generated by the persistent current, to a second qubit. The qubits are small (of order 1 micrometer), can individually be addressed and be integrated into large circuits.

Our qubit in principle consists of a loop with three small-capacitance Josephson junctions in series (Fig. 2.1a) that encloses an applied magnetic flux $f\Phi_0$ (Φ_0 is the superconducting flux quantum $h/2e$); f is slightly smaller than 0.5. Two of the junctions have equal Josephson coupling energy E_J; the coupling in the third junction is βE_J, with $0.5 < \beta < 1$. Useful values are $f = 0.495$ and $\beta = 0.75$ (as chosen in Fig. 2.1a). This system has two stable classical states with persistent circulating currents of opposite sign. For $f = 0.5$ the energies

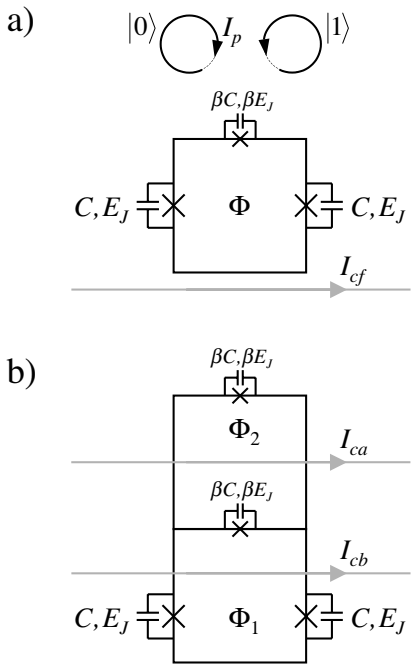

Figure 2.1: Persistent current qubit. **a)** Three-junction qubit. A superconducting loop with three Josephson junctions. The junctions are indicated with the parallel combination of the junction capacitance and the Josephson tunnel element (represented by the crosses). The loop encloses a flux that is supplied by an external magnet. The flux is $f\Phi_0$, where Φ_0 is the superconducting flux quantum and f is 0.495 here. Two junctions have a Josephson coupling energy E_J, the third junction βE_J, where $\beta = 0.75$ here. This system has two (meta)stable states $|0\rangle$ and $|1\rangle$ with opposite circulating persistent current I_p. The level splitting is determined by the offset from $\frac{1}{2}\Phi_0$ of the flux. The barrier between the states depends on the value of β. The qubit is operated by resonant microwave modulation of the enclosed magnetic flux by a superconducting control line (indicated in gray). **b)** Four-junction qubit. The top junction of of the circuit in a) is replaced by a parallel junction (DC-SQUID) circuit. There are two loops with equal areas; a magnet supplies a static flux $0.330\,\Phi_0$ to both. Qubit operations are performed with currents in superconducting control lines (indicated in gray) on top of the qubit, separated by a thin insulator. The microwave current I_{ca} couples only to the bottom loop and performs qubit operations as the circuit in a). I_{cb} couples to both loops; it is used for qubit operations with suppressed σ_z action and for an adiabatic increase of the tunnel barrier between qubit states to facilitate the measurement.

of the two states are the same; the offset from 0.5 determines the level splitting. The barrier for quantum tunnelling between the states depends strongly on the value of β. The four-junction version (Fig. 2.1b) allows modulating this barrier in situ. Here, the third junction has been converted into a parallel circuit of two junctions with each a coupling energy βE_J. The four-junction qubit behaves as the three-junction circuit of Fig. 2.1a, with an enclosed flux $(f_1 + \frac{1}{2}f_2)\Phi_0$ and a third-junction (SQUID) strength $2\beta E_J \cos(f_2\pi)$. The constant fluxes $f\Phi_0$, $f_1\Phi_0$, $f_2\Phi_0$ are supplied by an external static, homogeneous magnetic field. Control lines on a separate fabrication level couple inductively to individual qubit loops. All operations on qubits are performed using currents in the control lines.

When γ_1 and γ_2 are the gauge-invariant phase differences across the left and right junctions, the total Josephson energy U_J of the four-junction qubit is:

$$\begin{aligned}\frac{U_J}{E_J} = {} & 2 + 2\beta - \cos\gamma_1 - \cos\gamma_2 \\ & - 2\beta\cos(f_2\pi)\cos(2f_1\pi + f_2\pi + \gamma_1 - \gamma_2)\end{aligned} \tag{2.1}$$

In this expression the self-generated flux has been neglected. Although this flux will be used for coupling of qubits, it is much smaller than the flux quantum and only slightly changes the picture here. U_J is 2π-periodic in γ_1 and γ_2 (Fig. 2.2a) for the parameter values $\beta = 0.75$ and $f_1 = f_2 = 0.330$. Each unit cell has two minima L_{ij} and R_{ij} with left and right-handed circulating currents of about $0.75\, I_{co}$ at approximate γ_1, γ_2 values of $\pm 0.27\,\pi$. The minima would have been symmetric for $2f_1 + f_2 = 1$, which corresponds to a three-junction loop enclosing half a flux quantum. The set of all L minima yields one qubit state, the set of R minima the other. In γ_1–γ_2 space there are saddle-point connections between L and R minima as indicated with solid white (intra-cell, in) and dashed white lines (inter-cell, out). Along such trajectories the system can tunnel between its macroscopic quantum states. The Josephson energy along the trajectories is plotted in Fig. 2.2b. The saddle point energies U_{in} and U_{out} depend on β and f_2, lower SQUID coupling gives lower U_{in} but higher U_{out}. For $2\beta\cos(f_2\pi) < 0.5$ the barrier for intra-cell tunnelling has disappeared and there is only one minimum with zero circulating current.

Motion of the system in γ_1–γ_2 space can be discussed in analogy with motion of a mass-carrying particle in a landscape with periodic potential energy. Motion in phase space leads to voltages across junctions. The kinetic energy is the associated Coulomb charging energy of the junction capacitances. The mass is proportional to the junction capacitance C because other capacitance

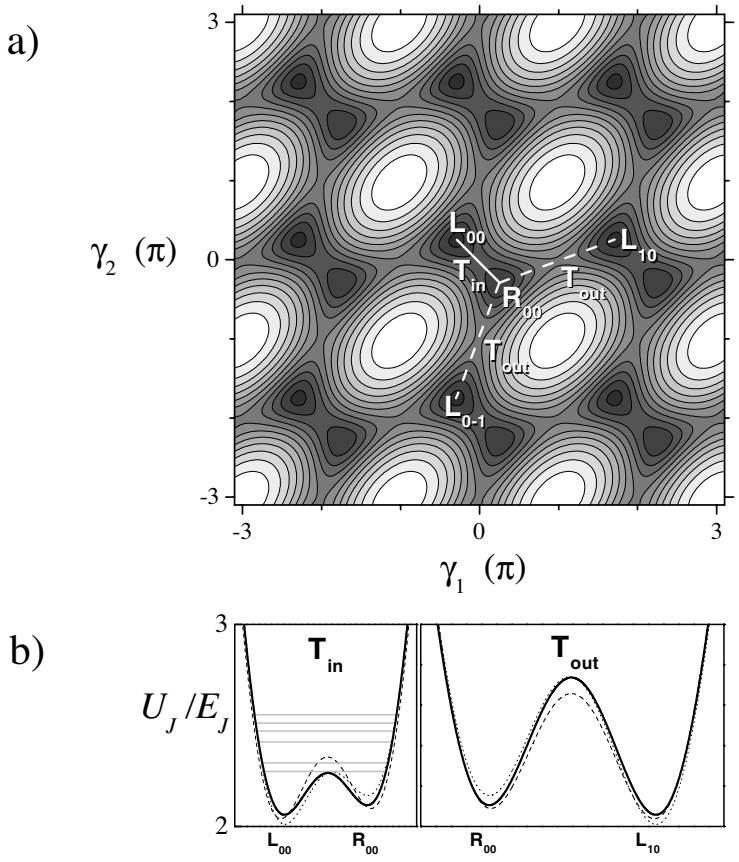

Figure 2.2: Josephson energy of qubit in phase space. **a)** Energy plotted as a function of the gauge-invariant phase differences γ_1 and γ_2 across the left and right junctions of Fig. 2.1a. The energy is periodic with period 2π. There are two minima in each unit cell, for the center cell indicated with L_{00} and R_{00}. The trajectory between L_{00} and R_{00} is indicated with the solid white line, the trajectories between R_{00} and minima in next-neighbor cells L_{10} and L_{0-1} are indicated with the dashed white lines. **b)** Energy along the solid and dashed trajectory of Fig. 2.2a. For the parameters chosen, the T_{out} saddle point is significantly higher than the T_{in} saddle point. As a result, tunnelling from cell to cell is suppressed and the qubit is decoupled from electrical potentials. Solid lines: $I_{ca} = I_{cb} = 0$ (see Fig. 2.1b). Dotted lines: Control current I_{cb} reduces the flux in the SQUID loop by $\delta_2 = -0.02$ times the flux quantum. Dashed lines: When β is increased from 0.75 the T_{in} saddle point goes up, while the T_{out} saddle point goes down (here drawn for $\delta_1 = -0.01$).

elements are small. The effective mass tensor has principal values M_a and M_b in the $\gamma_1 - \gamma_2 = 0$ and $\gamma_1 + \gamma_2 = 0$ directions. For the chosen values of the circuit parameters these principal values are $M_a = \hbar^2/(4E_C)$ and $M_b = \hbar^2/(E_C)$, where the charging energy is defined as $E_C = e^2/2C$. The system will perform plasma oscillations in the potential well with frequencies $\hbar\omega_b \approx 1.3\sqrt{E_C E_J}$ and $\hbar\omega_a \approx 2.3\sqrt{E_C E_J}$. The tunnelling matrix elements can be estimated by calculation of the action in the Wentzel-Kramers-Brillouin (WKB) approximation. For tunnelling within the unit cell between the minima L and R, the matrix element is $T_{in} \approx \hbar\omega_b \exp(-0.64\sqrt{E_J/E_C})$, for tunnelling from cell to cell $T_{out} \approx 1.6\hbar\omega_b \exp(-1.5\sqrt{E_J/E_C})$. For the qubit a subtle balance has to be struck: the plasma frequency must be small enough relative to the barrier height to have well-defined states with a measurable circulating current, but large enough (small enough mass) to have significant tunnelling. The preceding qualitative discussion has been confirmed by detailed quantitative calculations in phase space and in charge space [20]. From these calculations the best parameters for qubits can be determined. In practice it is possible to controllably fabricate aluminum tunnel junctions with chosen E_J and E_C values in a useful range.

It is strongly desirable to suppress the inter-cell tunnelling T_{out}. This leads to independence from electrical potentials, even if the charges on the islands are conjugate quantum variables to the phases. The qubit system in phase space is then comparable to a crystal in real space with non-overlapping atomic wave functions. In such a crystal the electronic wave functions are independent of momentum; similarly charge has no influence in our qubit.

Mesoscopic aluminum junctions can reliably be fabricated by shadow evaporation with critical current densities up to $500\,\mathrm{A/cm^2}$. In practice, a junction of 100 nm by 100 nm has E_J around 25 GHz and E_C around 20 GHz. A higher E_J/E_C ratio can be obtained by increasing the area, to which E_J is proportional and E_C inversely proportional. A practical qubit would for example have junctions with an area of 200 nm by 400 nm, $E_J \approx 200\,\mathrm{GHz}$, $E_J/Ec \approx 80$, level splitting $\Delta E \approx 10\,\mathrm{GHz}$, barrier height around 35 GHz, plasma frequency around 25 GHz, tunnelling matrix element $T_{in} \approx 1\,\mathrm{GHz}$. The matrix element for undesired tunnelling T_{out} is smaller than 1 MHz. The qubit size would be of order $1\,\mu$m; with an estimated inductance of 5 pH the flux generated by the persistent currents is about $10^{-3}\,\Phi_0$.

To calculate the dependence of the level splitting on f_1 and f_2 we apply a linearized approximation in the vicinity of $f_1 = f_2 = \frac{1}{3}$, defining F as the change of U_J away from the minimum of $U_J(\gamma_1, \gamma_2)$. This yields $F/E_J \approx 1.2(2(f_1 - \frac{1}{3}) +$

$(f_2 - \frac{1}{3})$). The level splitting without tunnelling would be 2F. With tunnelling, symmetric and anti-symmetric combinations are created; the level splitting is now $\Delta E = 2\sqrt{(F^2 + T_{in}^2)}$. As long as $F \gg T_{in}$, the newly formed eigen states are localized in the minima of $U_J(\gamma_1, \gamma_2)$.

We discuss qubit operations for the four-junction qubit. They are driven by the currents I_{ca} and I_{cb} in the two control lines (Fig. 2.1b). The fluxes induced in the two loops, normalized to the flux quantum, are $\delta_1 = (L_{a1}I_{ca} + L_{b1}I_{cb})/\Phi_0$, $\delta_2 = (L_{a2}I_{ca} + L_{b2}I_{cb})/\Phi_0$. The control line positions are chosen such that $L_{a2} = 0$ and $L_{b2} = -2L_{b1}$. When the two loops have equal areas, $f_1 = f_2$ for zero control current. We assume that the qubit states are defined with zero control current, and that δ_1, δ_2 act as perturbations to this system. The effective Hamiltonian operator in terms of Pauli spin matrices σ_x and σ_z for the chosen parameters is approximately

$$H_{op}/\Delta E \approx (80\delta_1 + 42\delta_2)\sigma_z - (9.2\delta_1 + 8.3\delta_2)\sigma_x \tag{2.2}$$

The numerical prefactors follow from the variational analysis of the influence of δ_1 and δ_2 on the tunnel barrier and the level splitting. The terms that contain σ_x can be used to induce Rabi oscillations between the two states, applying microwave pulses of frequency $\Delta E/h$. There are two main options, connected to one of the two control lines. Control current I_{ca} changes δ_1, which leads to a Rabi oscillation (σ_x term) as well as a strong modulation of the Larmor precession (σ_z term). As long as the Rabi frequency is far enough below the Larmor frequency, this is no problem. For $\delta_1 = 0.001$, the Rabi frequency is 100 Mhz. This mode is the only one available for the three-junction qubit and is most effective near the symmetry point $f = 0.5$ or $f_1 = f_2 = \frac{1}{3}$. Control current I_{cb} is used to modulate the tunnel barrier. Here the σ_z action is suppressed by means of the choice $L_{b2}/L_{b1} = \delta_2/\delta_1 = -2$. However, a detailed analysis shows that with δ_2 modulation it is easy to excite the plasma oscillation with frequency ω_b. One has to restrict δ_2 to remain within the two-level system. Values of 0.001 for δ_1 or δ_2 correspond to about 50 pW microwave power at 10 GHz in the control line. These numbers are well within practical range.

Two or more qubits can be coupled by means of the flux that the circulating persistent current generates. The current is about 0.3 μA, the self-inductance of the loop about 5 pH and the generated flux about $10^{-3}\,\Phi_0$. When a superconducting closed loop (a flux transporter) with high critical current is placed on top of both qubits, the total enclosed flux is constant. A flux change in qubit

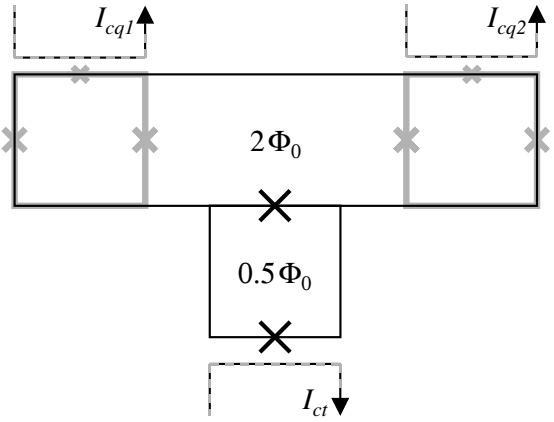

Figure 2.3: Switchable qubit coupler. A superconducting flux transporter (black) is placed on top of two qubits (gray), separated by a thin insulator. The transporter is a closed loop that contains two Josephson junctions in parallel (DC-SQUID) with high critical current. In the off state, the two loops of the transporter contain an integer number of flux quantums (main loop) and half a flux quantum (DC-SQUID loop), supplied by a permanent magnet. The current response to a flux change is very small. In the on state, the flux in the DC-SQUID loop is made integer by means of a control current I_{ct} (black-gray). As the transporter attempts to keep the flux in its loop constant, a flux change induced by qubit 1 is transmitted to qubit 2. As shown here, the two three-junction qubits experience $\sigma_z \otimes \sigma_z$ type coupling. The flux values have to be adjusted for the influence of circulating currents.

1 is transmitted approximately by half to qubit 2. One can choose to couple the flux, generated in the main loop of qubit 1, to the main loop of qubit 2 (i. e. $\sigma_z \otimes \sigma_z$ coupling) or to the SQUID loop of qubit 2 (i. e. $\sigma_z \otimes \sigma_x$ coupling). A two-qubit gate operation is about as efficient as a single qubit operation driven with $\delta_1 = 0.001$. An example of a possible controlled-NOT operation with fixed coupling runs as follows: The level splitting of qubit 2 depends on the state of qubit 1, the values are ΔE_{20} and ΔE_{21}. When Rabi microwave pulses, resonant with ΔE_{21}, are applied to qubit 2, it will only react if qubit 1 is in its $|1\rangle$ state. In principle qubits can be coupled at larger distances. An array scheme as proposed by Lloyd [1], where only nearest-neighbor qubits are coupled, is also very feasible. It is possible to create a flux transporter that has to be switched on by a control current (Fig. 2.3).

The typical switching times for our qubit are 10 to 100 ns. To yield a practical quantum computer, the decoherence time should be at least 100 μs. We can estimate the influence of known sources of decoherence for our system, but it is impossible to determine the real decoherence time with certainty, except by measurement. We discuss some decohering influences here. All quasiparticle states in the superconductor have to remain unoccupied. In equilibrium, the number is far below one at temperatures below 30 mK. Extreme care must be taken to shield the sample from photons. Even 4 K blackbody photons have enough energy to break a Cooper pair. Adequate shielding is possible on the time scale of our computer. Inductive coupling to bodies of normal metal has to be avoided. By decoupling the qubit from electrical potentials, we have eliminated coupling to charged defects in substrate or tunnel barriers. The aluminum nuclei have a spin that is not polarized by the small magnetic fields at our temperature of 25 mK. Statistical fluctuations will occur, but their time constant is very long due to the absence of electronic quasiparticles. The net effect will be a small static offset of the level splitting, within the scale of the variations due to fabrication. The dephasing time that results from unintended dipole-dipole coupling of qubits is longer than 1 ms if the qubits are further apart than 1 μm. Emission of photons is negligible for the small loop. Overall, the sources of decoherence that we know allow for a decoherence time above 1 ms.

Requirements for a quantum computer are that the qubits can be prepared in well-defined states before the start of the computation and that their states can be measured at the end. Initialization will proceed by cooling the computer to below 50 mK and having the qubits settle in the ground state. For the measurement, a generated flux of $10^{-3}\,\Phi_0$ in an individual qubit can be detected with a SQUID if enough measuring time is available. A good SQUID has a sensitivity of $10^{-5}\,\Phi_0/\sqrt{\mathrm{Hz}}$, so that a time of 100 μs is required. Usual SQUIDs have junctions that are shunted with normal metal. The shunt introduces severe decoherence in a qubit when the SQUID is in place, even if no measurement is performed. We are developing a non-shunted SQUID that detects its critical current by discontinuous switching. For a measurement at the end of a quantum computation scheme, the qubit can be frozen by an adiabatic increase of the tunnel barrier between the two qubit states. As Fig. 2.2 indicates, we can increase the barrier by a change of control current. A similar procedure as suggested by Shnirman *et al.* [19] for charge qubits can be followed.

The proposed qubit should be of considerable interest for fundamental studies of macroscopic quantum coherence, apart from its quantum computing potential.

Compared with the RF SQUID systems that have been used in attempts to observe such effects [21, 22] and also have been suggested as possible qubits for quantum computation [23], the much smaller size of the qubit decouples it significantly better from the environment.

We thank J. J. Mazo, C. J. P. M. Harmans, A. C. Wallast and H. Tanaka for important discussions. This work is partially supported by ARO grant DAAG55-98-1-0136, by the Dutch FOM, NSF Award 67436000IRG and by NEDO.

References

[1] S. Lloyd, *Science* **261**, 1569 (1993).

[2] C. H. Bennett, *Physics Today* **48**, 24 (October 1995).

[3] D. P. Divincenzo, *Science* **270**, 255 (1995).

[4] S. Lloyd, *Scientific American* **273**, 140 (April 1995).

[5] Q. A. Turchette, C. J. Hood, W. Lange, H. Mabuchi, H. J. Kimble, *Phys. Rev. Lett.* **75**, 4710 (1995).

[6] C. Monroe, D. M. Meekhof, B. E. King, W. M. Itano, D. J. Wineland, *Phys. Rev. Lett.* **75**, 4714 (1995).

[7] N. A. Gershenfeld, I. L. Chuang, *Science* **275**, 350 (1997).

[8] B. Kane, *Nature* **393**, 133 (1998).

[9] D. Loss, D. Divincenzo, *Phys. Rev. A* **57**, 120 (1998).

[10] L. B. Ioffe, V. B. Geshkenbein, M. V. Feigel'man, A. L. Fauchère, G. Blatter, *Nature* **398**, 679 (1999).

[11] D. V. Averin, K. K. Likharev, in *Mesoscopic Phenomena in Solids*, by B. L. Al'tshuler, P. A. Lee, R. A. Webb (Elsevier, Amsterdam, Netherlands, 1991).

[12] W. J. Elion, M. Matters, U. Geigenmuller, J. E. Mooij, *Nature* **371**, 594 (1994).

[13] L. S. Kuzmin, D. B. Haviland, *Phys. Rev. Lett.* **67**, 2890 (1991).

[14] P. Joyez, P. Lafarge, A. Filipe, D. Esteve, M. H. Devoret, *Phys. Rev. Lett.* **72**, 2458 (1994).

[15] Y. Nakamura, Yu. A. Pashkin, J. S. Tsai, *Nature* **398**, 786 (1999).

[16] A. Shnirman, G. Schön, Z. Hermon, *Phys. Rev. Lett.* **79**, 2371 (1997).

[17] D. V. Averin, *Solid State Commun.* **105**, 659 (1998).

[18] Yu. Makhlin, G. Schön, A. Shnirman, *Nature* **398**, 305 (1999).

[19] A. Shnirman, G. Schön, *Phys. Rev. B* **57**, 15400 (1998).

[20] T. P. Orlando *et al.*, *Phys. Rev. B.* **60**, 15398 (1999).

[21] C. D. Tesche, *Phys. Rev. Lett.* **64**, 2358 (1990).

[22] R. Rouse, S. Han, J. E. Lukens, *Phys. Rev. Lett.* **75**, 1614 (1995).

[23] M. F. Bocko, A. M. Herr, M. J. Feldman, *IEEE Trans. Appl. Supercond.* **7**, 3638 (1997).

Chapter 3

Quantum Superposition of Macroscopic Persistent-Current States

Abstract

Microwave-spectroscopy experiments have been performed on two quantum levels of a macroscopic superconducting loop with three Josephson junctions. The level separation between the ground state and first excited state shows an anti-crossing where two classical persistent-current states with opposite polarity are degenerate. This is evidence for symmetric and anti-symmetric quantum superpositions of two macroscopic states; the classical states have persistent currents of 0.5 μA and correspond to the center-of-mass motion of millions of Cooper pairs. A study of the thermal occupancies of the two quantum levels shows that the loop is at low temperatures in a non-equilibrium state.

3.1 Introduction

When a small magnetic field is applied to a superconducting loop a persistent current is induced, also when the loop contains Josephson tunnel junctions. The current is clockwise or counter-clockwise, thereby either reducing or enhancing the applied flux to approach an integer number of superconducting flux quanta Φ_0 [1]. In particular when the enclosed magnetic flux is close to half integer values of Φ_0, the loop may have multiple stable persistent-current states, with at least two of opposite polarity. The weak coupling of the Josephson junctions then allows

This chapter is based on Refs. 6 and 7 on p. 111.

for transitions between the states. Previous theoretical work [2, 3, 4] proposed that a persistent current in a loop with Josephson junctions corresponds to the center-of-mass motion of all the Cooper pairs in the system, and that quantum mechanical behavior of such persistent-current states would be a manifestation of quantum mechanical behavior of a macroscopic object. In a micrometer-sized loop millions of Cooper pairs are involved. At very low temperatures, excitations of individual charge carriers around the center of mass of the Cooper-pair condensate are prohibited by the superconducting gap. As a result the coupling between the dynamics of persistent supercurrents and many-body quasi-particle states is very weak. Josephson junction loops therefore rank among the best objects for experimental tests of the validity of quantum mechanics for systems containing a macroscopic number of particles [3, 5, 6] (loss of quantum coherence results from coupling to an environment with many degrees of freedom [7]) and for research on the border between classical and quantum physics. The potential for quantum coherent dynamics has stimulated research aimed at applying Josephson junction loops as basic building blocks for quantum computation (qubits) [8, 9, 10, 11].

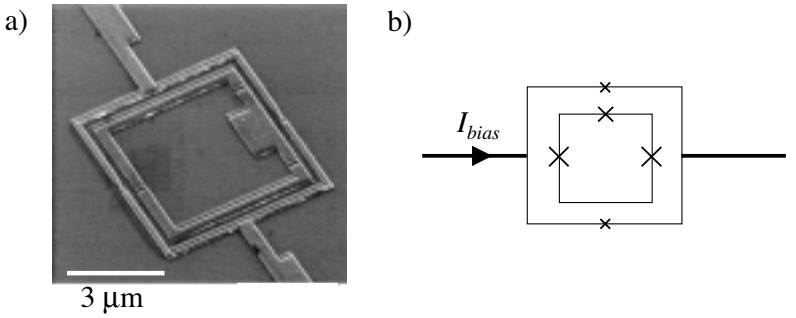

Figure 3.1: SEM-image **(a)** and schematic **(b)** of the small superconducting loop with three Josephson junctions (denoted by the crosses). The loop is inductively coupled to an underdamped DC-SQUID which is positioned around the loop. The DC-SQUID can be used as a magnetometer by applying a bias current I_{bias} to it.

We present microwave-spectroscopy experiments that demonstrate quantum superpositions of two macroscopic persistent-current states in a small loop with three Josephson junctions (Fig. 3.1). At an applied magnetic flux of $\frac{1}{2}\Phi_0$ the system behaves as a particle in a double-well potential, where the classical states in each well correspond to persistent currents of opposite sign. The two classical

states are coupled via quantum tunneling through the barrier between the wells, and the loop is a macroscopic quantum two-level system (Fig. 3.2a) [12]. The energy levels vary with the applied flux as shown (Fig. 3.2b). Classically, the levels cross at $\frac{1}{2}\Phi_0$. Tunneling between the wells leads to quantum mechanical eigen states that at $\frac{1}{2}\Phi_0$ are symmetric and anti-symmetric superpositions of the two classical persistent-current states. The symmetric superposition state is the quantum mechanical ground state with an energy lower than the classical states, the anti-symmetric superposition state is the loop's first excited state with an energy higher than the classical states. The superposition states thus manifest themselves as an anti-crossing of the loop's energy levels near $\frac{1}{2}\Phi_0$. Our spectroscopy results show the expected anti-crossing at $\frac{1}{2}\Phi_0$ (Fig. 3.4) [13]. We also studied the resonance-line shapes and found behavior similar to microscopic quantum two-level systems [15, 16] (Fig. 3.5). A study of the thermal broadening of the transition between the two states at $\frac{1}{2}\Phi_0$ shows that the loop is at low temperatures in a non-equilibrium state (Fig. 3.6).

In our experiments, the magnetic flux generated by the loop's persistent current was measured with an inductively coupled direct-current superconducting quantum interference device (DC-SQUID, see Figs. 3.1 and 3.3), while low-amplitude microwaves were applied to induce transitions between the levels. We observed narrow resonance lines at magnetic field values where the level separation ΔE was resonant with the microwave frequency. The DC-SQUID performs a measurement on a single quantum system. Thus we should expect that the measurement process limits the coherence of our system. While the system is pumped by the microwaves, the SQUID actively measures the flux produced by the persistent currents of the two states. Detecting the quantum levels of the loop is still possible as the meter is only weakly coupled to the loop. The flux signal needs to be built up by averaging over many repeated measurements on the same system (Fig. 3.3b), such that effectively an ensemble average is determined. We measure the level separation, i. e. energy, rather than flux, as we perform spectroscopy, and we observe a change in averaged flux when the microwaves are resonant with the level separation (the peaks and dips in Figs. 3.3b and 3.4a). We also chose to work with an extremely underdamped DC-SQUID with unshunted junctions to minimize damping of the quantum system via the inductive coupling to the SQUID.

Similar observations were recently made by Friedman *et al.* [17] who performed spectroscopy on excited states in a loop with a single Josephson junction (radio-frequency SQUID). Previous experiments with single-junction loops have

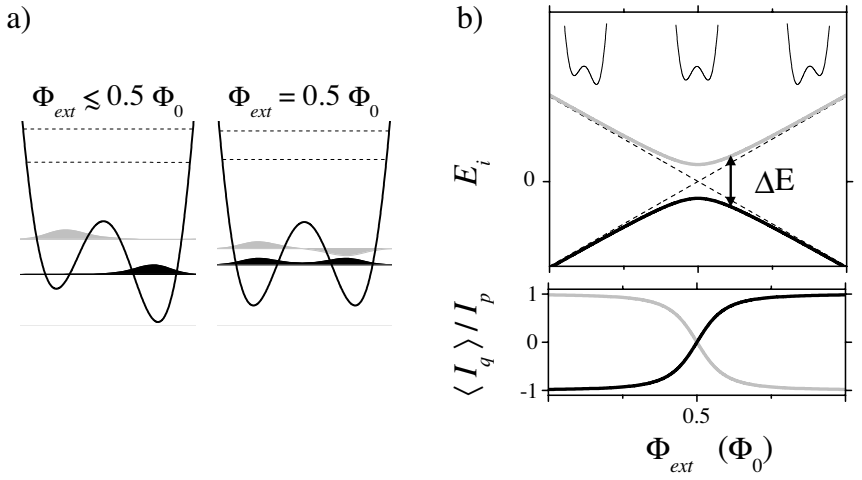

Figure 3.2: a) Schematic presentation of the loop's double-well potential with energy levels [12] for an applied flux Φ_{ext} below $\frac{1}{2}\Phi_0$ (left) and at $\frac{1}{2}\Phi_0$ (right). The vertical axis is energy, the horizontal axis is a Josephson phase coordinate. In the vicinity of $\Phi_{ext} = \frac{1}{2}\Phi_0$ the loop is a double-well system in which the two minimums correspond to classical states with persistent currents of equal magnitude I_p, but with opposite polarity. Quantum mechanically, the system has two low-energy eigen states (black and gray) that are well separated in energy from higher excited states (dashed lines), such that it is effectively a quantum two-level system. The shape of the wave function of the ground state (black) and first excited state (gray) is shown at the energy level. For Φ_{ext} below or above $\frac{1}{2}\Phi_0$ the two lowest eigen states are well localized on either side of the barrier, and correspond (apart from zero-point energy) to the classical persistent-current states. When quantum tunneling between the wells is possible, the loop's eigen states are at $\Phi_{ext} = \frac{1}{2}\Phi_0$ symmetric and anti-symmetric superpositions of the two persistent-current states. The schematic plots show a distribution of the levels in the potential that is typical for the device parameters mentioned in the text. **b)** Energy levels and persistent currents of the loop as a function of applied flux Φ_{ext}. The insets of the top plot show again the double-well potential, for Φ_{ext} below $\frac{1}{2}\Phi_0$ (left), at $\frac{1}{2}\Phi_0$ (middle), and above $\frac{1}{2}\Phi_0$ (right). The energies of the two localized persistent-current states are indicated with the dashed lines, and they cross at $\Phi_{ext} = \frac{1}{2}\Phi_0$. The quantum levels (solid lines) show an anti-crossing near $\Phi_{ext} = \frac{1}{2}\Phi_0$, and are separated in energy by ΔE. The bottom plot shows the quantum mechanical expectation value $\langle I_q \rangle = -\partial E_i / \partial \Phi_{ext}$ of the persistent current in the loop, for the ground state E_0 and the excited state E_1, plotted in units of the classical magnitude of the persistent currents I_p.

demonstrated resonant tunneling between discrete quantum states in two wells [18, 19] and microwave-induced transitions between the wells [20, 21]. Other observations that have been related to macroscopic superposition states are tunnel splittings observed with magnetic molecular clusters [22, 23] and quantum interference of C_{60} molecules [24]. In quantum dots [25] and superconducting circuits where charge effects dominate over the Josephson effect [26, 27, 28] superpositions of charge states have been observed, as well as quantum coherent charge oscillations [29].

Our quantum system is a low-inductance loop intersected by three Josephson tunnel junctions (Fig. 3.1) [10, 11]. The Josephson junctions are extremely underdamped, and are characterized by their Josephson coupling E_J and charging energy $E_C = e^2/2C$, where C is the junction capacitance and e the electron charge. The critical current of a junction is $I_{C0} = \frac{2e}{\hbar}E_J$, where $\hbar = \frac{h}{2\pi}$ is Planck's reduced constant. One of the junctions in the loop has E_J and C smaller by a factor $\beta \approx 0.8$. At an applied flux Φ_{ext} close to $\frac{1}{2}\Phi_0$ the total Josephson energy forms a double well potential. The classical states at the bottom of each well have persistent currents of opposite sign, with a magnitude I_p very close to I_{C0} of the weakest junction, and with energies $E = \pm I_p(\Phi_{ext} - \frac{1}{2}\Phi_0)$ (dashed lines in Fig. 3.2b) [30]. The system can be pictured as a particle with a mass proportional to C in the Josephson potential; the electrostatic energy is the particle's kinetic energy. The charging effects are conjugate to the Josephson effect. For low-capacitance junctions (small mass) quantum tunneling of the particle through the barrier gives a tunnel coupling t between the persistent-current states. In the presence of quantum tunneling and for E_J/E_C values between 10 and 100, the system should have two low-energy quantum levels E_0 and E_1, which can be described using a simple quantum two-level picture [10, 11], $E_{0(1)} = -(+)\sqrt{t^2 + \left(I_p(\Phi_{ext} - \frac{1}{2}\Phi_0)\right)^2}$. The loop's level separation $\Delta E = E_1 - E_0$ is then

$$\Delta E = \sqrt{(2t)^2 + \left(2I_p(\Phi_{ext} - \frac{1}{2}\Phi_0)\right)^2}. \tag{3.1}$$

3.2 Experimental realization

The system was realized by microfabricating an aluminum micrometer-sized loop with unshunted Josephson junctions (Fig. 3.1a). The sample consisted of a 5 x 5 μm^2 aluminum loop with aluminum-oxide tunnel junctions, microfabricated with e-beam lithography and shadow-evaporation techniques on a SiO_2 substrate. The

electrodes of the loop were 450 nm wide and 80 nm thick. The DC-SQUID magnetometer was fabricated in the same layer around the inner loop, with a 7 x 7 μm^2 loop and smaller Josephson junctions that were as underdamped as the junctions of the inner loop. The DC-SQUID had an on-chip superconducting shunt capacitance of 2 pF and superconducting leads in four-point configuration. The sample was mounted in a dilution refrigerator, inside a microwave-tight copper measurement box, magnetically shielded by two mu-metal and one superconducting shield. All spectroscopy measurements were taken with the temperature stabilized at 30 ± 0.05 mK. Microwaves were applied to the sample by a coaxial line, which was shorted at the end by a small loop of 5 mm diameter. This loop was positioned parallel to the sample plane at about 1 mm distance. Switching currents were measured with dedicated electronics, with repetition rates up to 9 kHz and bias currents ramped at typically 1 μA/ms (further details of the fabrication and experimental techniques can be found in Ref. [31]). Loop parameters estimated from test junctions fabricated on the same chip and electron-microscope inspection of the measured device give give $I_{C0} = 570 \pm 60$ nA and $C = 2.6 \pm 0.4$ fF for the largest junctions in the loop and $\beta = 0.82 \pm 0.1$, giving $E_J/E_C = 38 \pm 8$ and $I_p = 450 \pm 50$ nA. Due to the exponential dependence of the tunnel coupling t on the mass (C) and the size of the tunnel barrier, these parameters allow for a value for t/h between 0.2 and 5 GHz. The parameters of the DC-SQUID junctions were $I_{C0} = 109 \pm 5$ nA and $C = 0.6 \pm 0.1$ fF. The self inductance of the inner loop and the DC-SQUID loop were numerically estimated to be 11 ± 1 pH and 16 ± 1 pH respectively, and the mutual inductance between the loop and the SQUID was 7 ± 1 pH.

The flux in the DC-SQUID is measured by ramping a bias current through the DC-SQUID and recording the current level I_{SW} where the SQUID switches from the supercurrent branch to a finite voltage (Fig. 3.3a). Traces of the loop's flux signal were recorded by continuously repeating switching-current measurements while slowly sweeping the flux Φ_{ext} (Fig. 3.3b). The measured flux signal from the inner loop will be presented as $\tilde{I}_{SW}$, which is an averaged value directly deduced from the raw switching-current data, as described in the following three points:

1) Because the variance in I_{SW} was much larger than the signature from the loop's flux (Fig. 3.3a) we applied low-pass FFT-filtering in Φ_{ext}-space (over 10^7 switching events for the highest trace, and $2 \cdot 10^8$ events for the lowest trace in Fig. 3.4a). We checked that the cut-off frequency was chosen high enough not to influence any parameters deduced from the data.

2) By applying Φ_{ext} we also apply flux directly to the DC-SQUID. The resulting

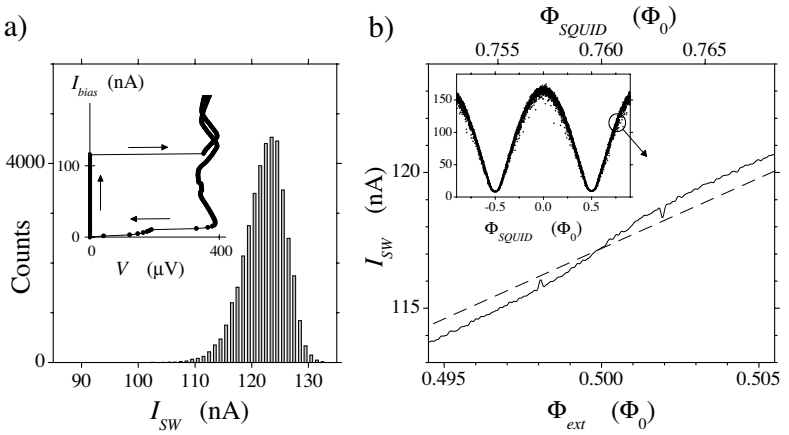

Figure 3.3: a) Current-voltage characteristic (inset) and switching-current histogram of the underdamped DC-SQUID. The plot with bias current I_{bias} versus voltage V is strongly hysteretic. The I_{bias} level where the SQUID switches from the supercurrent branch to a finite voltage state –the switching current I_{SW}– is a measure for the flux in the loop of the DC-SQUID. Switching to the voltage state is a stochastic process. The histogram in the main plot shows that the variance in I_{SW} is much larger than the flux signal of the inner loop's persistent current, which gives a shift in the averaged I_{SW} of about 1 nA (see Fig. 3.3b). **b)** Switching-current levels of the DC-SQUID versus applied flux. The inset shows the modulation of I_{SW} versus the flux Φ_{SQUID} applied to the DC-SQUID loop (data not averaged, one point per switching event). The main figure shows the averaged level of I_{SW} (solid line) near $\Phi_{SQUID} = 0.76\,\Phi_0$. At this point the flux in the inner loop $\Phi_{ext} \approx \frac{1}{2}\Phi_0$. The rounded step at $\Phi_{ext} = \frac{1}{2}\Phi_0$ indicates the change of sign in the persistent current of the loop's ground state. Symmetrically around $\frac{1}{2}\Phi_0$ the signal shows a peak and a dip, which are only observed with measurements in the presence of continuous-wave microwaves (here 5.895 GHz). The peak and dip are due to resonant transitions between the loop's two quantum levels (see Fig. 3.4). The background signal of the DC-SQUID that results from flux directly applied to its loop (dashed line) is subtracted from the data presented in Figs. 3.4a, 3.5a and 3.6a.

background signal (dashed line in Fig. 3.3b) was subtracted. We checked that the estimated dip and peak positions in Fig. 3.4b did not depend significantly on subtracting a background signal.

3) Applying microwaves and changing the sample temperature influenced the switching current levels significantly. To make the flux signal of all data sets

comparable we scaled all data sets to $I_{SW} = 100$ nA at $\Phi_{ext} = \frac{1}{2}\Phi_0$. Any uncertainty coming from this scaling is accounted for in the error bars in Figs. 3.4–3.6. Data taken in the presence of microwaves could only be obtained at specific frequencies where I_{SW} was not strongly suppressed by the microwaves. At temperatures above 300 mK drift in the I_{SW}-level due to thermal instabilities of the refrigerator obscured the signal.

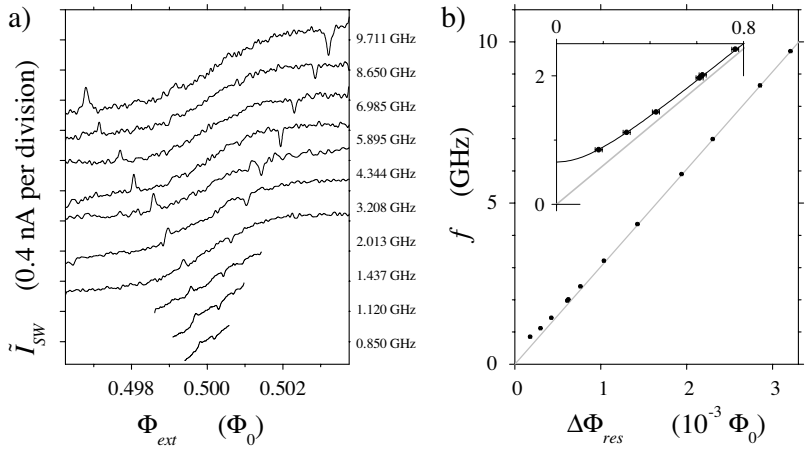

Figure 3.4: **a)** Resonance lines in traces of the scaled switching current $\tilde{I}_{SW}$ versus Φ_{ext}, measured at different microwave frequencies f (labels on the right). **b)** Half the distance in Φ_{ext} between the resonant peak and dip $\Delta\Phi_{res}$ at different microwave frequencies f. Peak and dip positions are determined from traces as in Fig. 3.4a. The inset zooms in on the low frequency data points. The grey line is a linear fit through the high frequency data and zero. The black line is a fit of (1).

3.3 Results

Fig. 3.4a shows the flux signal of the inner loop, measured in the presence of low-amplitude continuous-wave microwaves at different frequencies f. The rounded step in each trace at $\frac{1}{2}\Phi_0$ is due to the change in direction of the persistent current of the loop's ground state (see also Fig. 3.2b). Symmetrically around $\Phi_{ext} = \frac{1}{2}\Phi_0$ each trace shows a peak and a dip, which were absent when no microwaves were applied. The positions of the peaks and dips in Φ_{ext} depend

on microwave frequency but not on amplitude. The peaks and dips result from microwave-induced transitions to the state with a persistent current of opposite sign. These occur when the level separation is resonant with the microwave frequency, $\Delta E = hf$.

In Fig. 3.4b half the distance in Φ_{ext} between the resonant peak and dip $\Delta\Phi_{res}$ is plotted for all the frequencies f. The relation between ΔE and Φ_{ext} is linear for the high-frequency data. This gives $I_p = 484 \pm 2$ nA, in good agreement with the predicted value. At lower frequencies $\Delta\Phi_{res}$ significantly deviates from this linear relation, demonstrating the presence of a finite tunnel splitting at $\Phi_{ext} = \frac{1}{2}\Phi_0$. A fit to Eq. 1 yields $t/h = 0.33 \pm 0.03$ GHz, in agreement with the estimate from fabrication parameters. The level separation very close to $\frac{1}{2}\Phi_0$ could not be measured directly since at this point the expectation value for the persistent current is zero for both the ground state and the excited state (Fig. 3.2b). Nevertheless, the narrow resonance lines allow for an accurate mapping of the level separation near $\frac{1}{2}\Phi_0$, and the observed tunnel splitting gives clear evidence for quantum superpositions of the persistent-current states. The large uncertainty in the predicted t value does not allow for a quantitative analysis of a possible suppression of t due to a coupling between our two-level system and a bosonic environment [33] or a spin-bath environment [34, 35]. However, the fact that we see a finite tunnel splitting indicates that the damping of our quantum system by environmental degrees of freedom is weak. The dimensionless dissipation parameter α introduced by Leggett *et al.* [33] must be $\alpha < 1$.

In Fig. 3.5 we show the dependence of the dip shape at 5.895 GHz on applied microwave amplitude. The dip amplitude and the full width at half the maximum amplitude ($FWHM$) were estimated for different microwave amplitudes by fitting a Lorentzian peak shape to the data. Fig. 3.5b shows that the dip amplitude increases rapidly for microwave amplitudes up to $V_{AC} \approx 2$ a. u., followed by a saturation for larger microwave amplitudes. The saturated dip amplitude is $\approx$ 0.25 nA, which is close to half the full step height of the rounded step at $\frac{1}{2}\Phi_0$ ($\approx$ 0.4 nA) in Fig. 3.4a. This indicates that on resonance the energy levels are close to being equally populated, as expected for pumping with continuous-wave microwaves.

Fig. 3.5c shows a linear dependence between the $FWHM$ and the microwave amplitude. Qualitatively this dependence of the line shape on microwave amplitude agrees with spectroscopy results on microscopic quantum two-level systems. For negligible decoherence, spectroscopy on quantum two-level systems yields a Lorentzian line shape and transitions between the levels occur by coherent Rabi

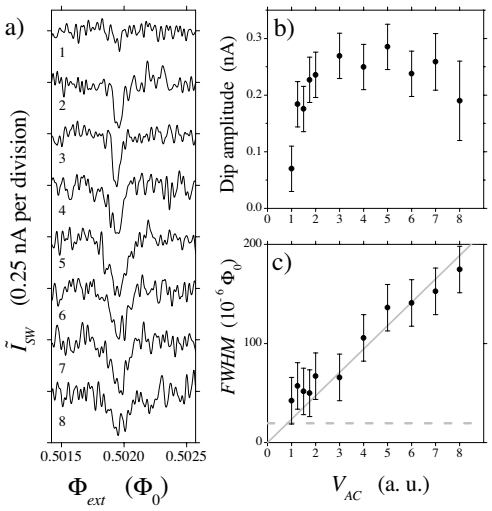

Figure 3.5: **a)** The influence of the microwave amplitude on the shape of the resonance dip in the scaled switching current $\tilde{I}_{SW}$, measured at 5.895 GHz (the labels on the left give the amplitude V_{AC} in a. u.)). **b)** The dip amplitude first increases with microwave amplitude V_{AC}, but saturates at $V_{AC} > 2$ a. u. **c)** The full-width-half-max ($FWHM$) of the dips increases with V_{AC}. The linear fit through the highest data points and zero is a guide to the eye. The horizontal dashed line is at a flux value that corresponds to the shift in effective flux bias Φ_{ext} that is induced when the bias current is ramped through the DC-SQUID. This acts as a flux instability with an amplitude of $\approx 20 \cdot 10^{-6}\,\Phi_0$. Resonance lines with a $FWHM$ below this value cannot be observed. The loss of dip amplitude in Fig. 3.5b when lowering $V_{AC} < 2$ a. u. sets in where the $FWHM \lesssim 20 \cdot 10^{-6}\,\Phi_0$. The flux shift from the SQUID is calculated using the I_{bias} interval (the $FWHM$ of the switching-current histogram is used) where the SQUID typically switches.

oscillations. The $FWHM$ of the Lorentzian resonance line is two times the Rabi frequency and is proportional to the amplitude of the monochromatic perturbation [15]. The linear dependence of the $FWHM$ on microwave amplitude in Fig. 3.5c suggests that the line width is for $V_{AC} > 2$ a. u. dominated by the frequency of microwave-induced Rabi transitions. Transitions occur then by a few quantum coherent Rabi cycles. Using the linear relation between ΔE and Φ_{ext} for Φ_{ext} values away from $\frac{1}{2}\Phi_0$, the observed $FWHM$ in Φ_{ext} units can be expressed

in frequency units. This indicates a Rabi frequency of for example 150 MHz at $V_{AC} = 4$ a. u. However, we do not consider these results as proof for coherent quantum dynamics as other scenarios with weak decoherence give similar results [36].

The loss of dip amplitude and the apparent saturation of the $FWHM$ at low V_{AC} is either caused by variations in the flux bias Φ_{ext} (corresponding to inhomogeneous broadening for the ensemble average [16]) or by an intrinsic dephasing mechanism. The effective dephasing time T_2^* [16] can be deduced from the $FWHM$ at low V_{AC}. The $FWHM$ (expressed in energy units) of a resonance-line shape that is dominated by a finite dephasing time corresponds to $\frac{2\hbar}{T_2^*}$ [16, 15]. Using once more the linear relation between ΔE and Φ_{ext} for Φ_{ext} values away from $\frac{1}{2}\Phi_0$ to express the $FWHM$ at $V_{AC} \lesssim 2$ a. u. in energy units, gives $T_2^* \approx 10$ ns. As will be discussed later this can be fully explained by variations in the applied magnetic flux that originate from the measuring DC-SQUID.

The DC-SQUID performs a weak measurement on the loop. It has two macroscopic phase degrees of freedom. One is associated with the circulating current in the SQUID's loop (internal degree of freedom), the other is associated with the bias current through the SQUID (external degree of freedom). As the bias current is ramped up, the coupling between these two degrees of freedom increases strongly, due to the non-linearity of the SQUID's current-phase relations [1]. The external variable is coupled to a dissipative environment, and the associated effective mass (i. e. the capacitance across the SQUID) is very large. The internal degree of freedom has no intrinsic damping and the associated mass (i. e. the capacitance of the junctions of the SQUID) is very small. As a consequence this variable exhibits quantum behavior. The classical external degree of freedom of the SQUID performs a measurement on the SQUID's inner quantum variable, which in turn is weakly coupled to our quantum loop. We therefore expect that the SQUID contributes dominantly to the loop's dephasing and damping with the present setup. The choice for an underdamped DC-SQUID resulted in very wide switching-current histograms. The width of the histogram corresponds to a standard deviation in the flux read out of $11 \cdot 10^{-3}\,\Phi_0$. The uncertainty in flux read out is much is larger than the flux signal from the inner loop $2MI_p \approx 3 \cdot 10^{-3}\,\Phi_0$. As a consequence, we can only detect the loop's signal by averaging over many switching events (Fig. 3.3).

The loss of dip amplitude in Fig. 3.5 is probably due to a small contribution to the effective Φ_{ext} from the circulating current in the DC-SQUID. The SQUID is operated at 0.76 Φ_0 in its loop, where its circulating current depends on the

bias current due to its non-linear behavior [1]. This means that data recorded by switching events on the low I_{bias} side of the $FWHM$ of the I_{SW} histogram in Fig. 3.3a differs in flux bias on the inner loop from that of the high side by $20 \cdot 10^{-6}\,\Phi_0$. Resonance lines at low V_{AC} (i. e. with a $FWHM < 20 \cdot 10^{-6}\,\Phi_0$) cannot be observed as the peaks and dips smear out when averaging over many switching events. The loss of dip amplitude and the apparent saturation of the $FWHM$ at low V_{AC} is probably dominated by this mechanism for inhomogeneous line broadening.

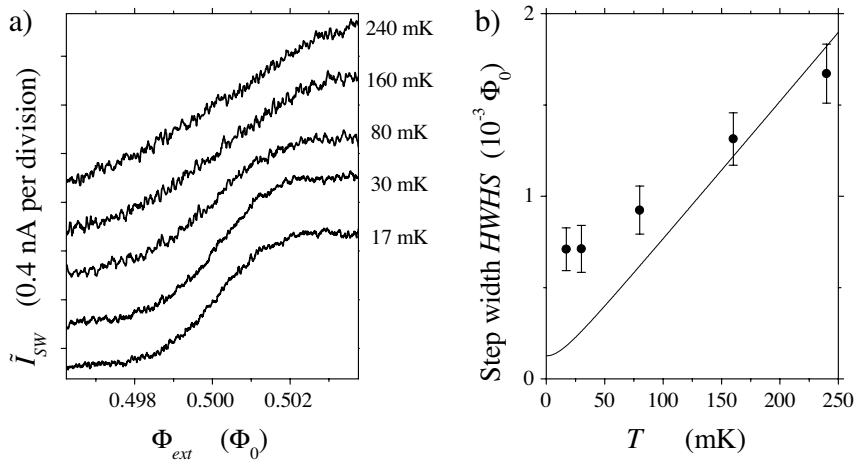

Figure 3.6: a) $\tilde{I}_{SW}$ versus Φ_{ext}, measured at different temperatures T (labels on the right). No microwaves were applied. The step in $\tilde{I}_{SW}$ broadens with temperature. **b)** The width of the step as a function of temperature. The half-width-half-step (HWHS) is defined as the distance in Φ_{ext} from $\frac{1}{2}\Phi_0$ to the point where the amplitude of the step is half completed. The solid line is the calculated HWHS for thermally mixed levels, using (1) and the I_p and t-value from the spectroscopy results, with a saturating width on the scale of t at low temperatures.

The width of the rounded steps in the measured flux in Figs. 3.4a is much broader than expected from quantum rounding on the scale of the value of t that was found with spectroscopy (see also Fig. 1c). We checked the temperature dependence of the step width, measured in the absence of microwaves. The temperature dependence of the step width presented in Fig. 3.6 confirms that the step width HWHS (defined in the caption of Fig. 3.6b) is too wide at low

temperatures T. At temperatures above 100 mK the step width is in agreement with the thermally averaged expectation value for the persistent current $< I_{th} >= I_p \tanh\left(\frac{\Delta E}{2k_B T}\right)$ (k_B is Boltzmann's constant), where we use the level separation ΔE and I_p found with spectroscopy. However, when lowering the temperature the observed step width saturates at an effective temperature of about 100 mK. We checked that the effective temperature for the SQUID's switching events did not saturate at the lowest temperatures. The high effective temperature of the loop is a result of the loop being in a non-equilibrium state. Cooling the sample longer after the dissipative switching events did not make the step narrower. The step width at $T = 30$ mK was measured with 100 μs and 50 ms dead time between switching events, but no significant differences were found. This indicates that the out-of-equilibrium population of the excited state is caused by the measurement process with the SQUID or other weakly coupled external processes, in combination with a long time scale for cooling the system to equilibrium (as can be expected since it is very well isolated from the environment). Note that the observed line width and the level separation near $\frac{1}{2}\Phi_0$ are small compared to the effective temperature of 100 mK. Silvestrini *et al.* [37] showed that this can be the case in a Josephson junction system when the transitions between the levels occur much faster than the thermal mixing time, a phenomena that is also well known from e. g. room-temperature NMR on liquids [16].

3.4 Concluding remarks and future prospects.

The data presented here provides clear evidence that a small Josephson junction loop can behave as a macroscopic quantum two-level system. The application of an underdamped DC-SQUID for measuring the loop's magnetization is a useful tool for future work on quantum coherent experiments with Josephson junction loops. The present results also demonstrate the potential of three-junction persistent-current loops for research on macroscopic quantum coherence and for use as qubits in a quantum computer. This requires quantum state control with pulsed microwaves and development of measurement schemes that are less invasive. Circuits that contain multiple qubits with controlled inductive coupling are within reach using present-day technology.

We thank J. B. Majer, A. C. Wallast, L. Tian, D. S. Crankshaw, J. Schmidt, A. Wallraff, L. Levitov and D. Esteve for help and stimulating discussions. This work was financially supported by the Dutch Foundation for Fundamental Research on Matter (FOM), the European TMR research network on superconduct-

ing nanocircuits (SUPNAN), the USA Army Research Office (grant DAAG55-98-1-0369) and the NEDO joint research program (NTDP-98).

References

[1] M. Tinkham, *Introduction to Superconductivity* (McGraw-Hill, Inc., New York, ed. 2, 1996).

[2] P. W. Anderson, in *Lectures on the Many-Body Problem*, E. R. Caianiello, Ed. (Academic Press, New York, 1964), vol. 2, pp. 113-135.

[3] A. J. Leggett, *Prog. Theor. Phys. Suppl.* **69**, 80 (1980).

[4] K. K. Likharev, *Sov. Phys. Usp.* **26**, 87 (1983).

[5] A. J. Leggett, A. Garg, *Phys. Rev. Lett.* **54**, 857 (1985).

[6] A. J. Leggett, *J. Supercond.* **12**, 683 (1999).

[7] W. H. Zurek, *Phys. Today* **44**, 36 (October 1991).

[8] M. F. Bocko, A. M. Herr, M. J. Feldman, *IEEE Trans. Appl. Supercond.* **7**, 3638 (1997).

[9] L. B. Ioffe, V. B. Geshkenbein, M. V. Feigel'man, A. L. Fauchère, G. Blatter, *Nature* **398**, 679 (1999).

[10] J. E. Mooij *et al.*, *Science* **285**, 1036 (1999).

[11] T. P. Orlando *et al.*, *Phys. Rev. B.* **60**, 15398 (1999).

[12] The double-well potential that is shown in Fig. 3.2a is the relevant potential for the tunnel transitions between the system's two persistent-current states. The potential is the sum of the Josephson energies of all the junctions and the zero-point energy of a Josephson phase degree of freedom that is perpendicular to the tunnel direction between the two wells [10, 11]. This zero-point energy is nearly constant along the tunnel trajectory between the wells, and has a plasma frequency much higher than the level separation between the lowest to quantum levels. It should therefore be included in the effective potential for transitions between the two wells. For the sample parameters mentioned in the text the lowest two quantum levels are well below the top of the effective tunnel barrier.

[13] We acknowledge that the results presented here do not exclude alternative theories for quantum mechanics (e. g. macro-realistic theories [14]). This would require a type of experiment as proposed by Leggett *et al.* [5].

[14] For an in depth discussion on macro-realism see the essays of A. J. Leggett and A. Shimony in *Quantum Measurement: Beyond Paradox*, R. A. Healey, G. Hellman, Eds. (University of Minnesota Press, Minneapolis, 1998), pp. 1-31.

[15] C. Cohen-Tannoudji, B. Diu, F. Laloë, *Quantum Mechanics* (John Wiley & Sons, New York, 1977), vol. 1, pp. 443-454.

[16] A. Abragam, *Principles of Nuclear Magnetism* (Oxford University Press, Oxford, 1961), pp. 39-57.

[17] J. R. Friedman, V. Patel, W. Chen, S. K. Tolpygo, J. E. Lukens, *Nature* **406**, 43 (2000).

[18] R. Rouse, S. Han, J. E. Lukens, *Phys. Rev. Lett.* **75**, 1614 (1995).

[19] C. Cosmelli *et al.*, *Phys. Rev. Lett.* **82**, 5357 (1999).

[20] S. Han, R. Rouse, J. E. Lukens, *Phys. Rev. Lett.* **76**, 3404 (1996).

[21] S. Han, R. Rouse, J. E. Lukens, *Phys. Rev. Lett.* **84**, 1300 (2000).

[22] W. Wernsdorfer, R. Sessoli, *Science* **284**, 133 (1999).

[23] E. del Barco *et al.*, *Europhys. Lett.* **47**, 722 (1999).

[24] M. Arndt *et al.*, *Nature* **401**, 680 (1999).

[25] T. H. Oosterkamp *et al.*, *Nature* **395**, 873 (1998).

[26] Y. Nakamura, C. D. Chen, J. S. Tsai, *Phys. Rev. Lett.* **79**, 2328 (1997).

[27] V. Bouchiat, D. Vion, P. Joyez, D. Esteve, M. H. Devoret, *Phys. Scr.* **T76**, 165 (1998).

[28] D. J. Flees, S. Han, J. E. Lukens, *J. Supercond.* **12**, 813 (1999).

[29] Y. Nakamura, Yu. A. Pashkin, J. S. Tsai, *Nature* **398**, 786 (1999).

[30] The small self-generated flux due to the persistent currents leads to a constant lowering of the energies. The crossing remains at $\frac{1}{2}\Phi_0$. In the discussion we take Φ_{ext} to be the total flux in the loop.

[31] C. H. van der Wal, J. E. Mooij, *J. Supercond.* **12**, 807 (1999).

[32] The inductances were estimated numerically from the geometry with a finite-element method FASTHENRY, developped at MIT. The value for M is in agreement with the flux signal from the inner loop (estimated from the step height in flux units in Fig. 3.3b) divided by I_p.

[33] A. J. Leggett *et al.*, *Rev. Mod. Phys.* **59**, 1 (1987).

[34] N. Prokof'ev, P. Stamp, *Rep. Prog. Phys.* **63**, 669 (2000); cond-mat/0001080.

[35] Lin Tian *et al.*, to appear in *Quantum Mesoscopic Phenomena and Mesoscopic Devices in Microelectronics, Proceedings of a NATO-ASI workshop*; cond-mat/9910062.

[36] M. Grifoni, P. Hängi, *Phys. Rep.* **304**, 229 (1998).

[37] P. Silvestrini *et al.*, *Phys. Rev. Lett.* **79**, 3046 (1997).

Chapter 4

Engineering decoherence in Josephson persistent-current qubits: Measurement apparatus and other electromagnetic environments

Abstract

We discuss the relaxation and dephasing rates that result from the measurement setup itself in experiments on Josephson persistent-current qubits. For control and measurement of the qubit state, the qubit is inductively coupled to electromagnetic circuitry. We show how this system can be mapped on the spin-boson model, and how the spectral density of the bosonic bath can be derived from the electromagnetic impedance that is coupled to the qubit. Part of the electromagnetic environment is a measurement apparatus (DC-SQUID), that is permanently coupled to the single quantum system that is studied. Since there is an obvious conflict between long coherence times and an efficient measurement scheme, the measurement process is analyzed in detail for different measurement schemes. Parameters that can be realized in experiments today are used for a quantitative evaluation, and it is shown that the relaxation and dephasing rates that are induced by the measurement setup can be made low enough for a time-resolved study of the quantum dynamics of Josephson persistent-current qubits.

This chapter is based on Ref. 10 on p. 111.

4.1 Introduction

The founders of the quantum mechanical theory already recognized the conflict between a straight forward extrapolation of quantum mechanics to a macroscopic scale, and the intuitions we have about the laws that govern the macroscopic world. In particular, this concerned the possibility of quantum superpositions of collective coordinates (i. e. center-of-mass-like coordinates) of objects that are much bigger than the atomic scale. These difficulties were first presented by Schrödinger [1], and are now known as Schrödinger's cat paradox. Schrödinger's discussion of the cat in the box was clearly meant as a *gedanken* experiment. Only several decades later, after the discovery of the Josephson effect, it was recognized that the validity of quantum mechanics for a macroscopic degree of freedom could be tested in *real* experiments [2].

In 1980, Leggett pointed out that cryogenic and microfabrication technologies had advanced to a level where macroscopic Schrödinger's cat states could possibly be realized in small superconducting loops that contain Josephson tunnel junctions [3]. In such systems, the Josephson phase (or equivalently, the persistent supercurrent in the loop) is a collective coordinate for the Cooper-pair condensate, and it is conjugate to a variable which describes the charge difference across the Josephson tunnel junction. However, while the analysis of the isolated quantum system shows that superpositions of the macroscopic coordinates might very well occur in these loops, it is by no means obvious that such behavior can also be demonstrated experimentally. Just as for microscopic quantum systems, such superposition states are extremely fragile. Besides decoherence from a weak coupling to the degrees of freedom in the system's solid-state environment, also the fact that the loop is not isolated but permanently placed in an experimental setup might hinder attempts to study macroscopic quantum coherence. Nevertheless, interesting results with evidence for macroscopic quantum tunneling and energy level quantization were obtained with systems where the Josephson phase coordinate is trapped in a metastable well (for an overview see [4, 5, 6, 7]). More recently, quantum superposition states of persistent currents in Josephson junction loops have been demonstrated spectroscopically [8, 9], but time-resolved experiments that proof quantum-coherent dynamics of the persistent current, and experiments that could give formal evidence for macroscopic quantum coherence [10], have not been realized yet.

Whether such experiments can be realized at all has been intensively discussed in the literature [11], without concencus being reached. However, a detailed

analysis with estimates based on measurement techniques that can be realized in experiments *today*, has been discussed very little. In recent experiments on Josephson junction systems where charge effects dominate over the Josephson effect, quantum coherent dynamics has been demonstrated [12], which indicates that it might be possible to obtain similar experimental results with Josephson persistent-current loops. Efforts in this direction were stimulated by the prospect that it should be possible to realize a quantum computer with superconducting Josephson devices [13, 14, 15, 16]. An important advantage of a Josephson quantum computer would be that, if accurate quantum coherent control of elementary units would be possible at all, it would be a system that can be extended to one containing a very large number of quantum bits (qubits). The large size of the qubits might allow for individual (local) control and readout of the qubits and qubit-qubit couplings.

In this chapter we analyze the feasibility of demonstrating quantum coherent dynamics with Josephson persistent currents, using experimental techniques that can be realized in the laboratories *today* (i. e. assuming the available techniques for device fabrication, cryogenics, microwave applications and electronic filtering). Neglecting for the moment new measurement techniques that might become available in the future, such mesoscopic solid-state experiments suffer from the difficulty that one cannot avoid that an electronic measuring device is permanently coupled to the *single* quantum system that is studied [18]. A meter must be present in any useful experiment, and, unlike experiments with for instance photons, this means that a measuring device must be permanently located very close to the solid-state quantum bit (e. g. fabricated on the same chip). With such a setup, there is obviously a conflict between an efficient measurement scheme with a strong measurement, and long decoherence times in the quantum system that is studied. For successful experiments in this direction, a detailed understanding of the measurement scheme is therefore needed such that the decoherence that is induced by the setup itself can be reduced to an acceptable level. Obviously, there exist many other sources of decoherence for Josephson qubits that one should worry about as well. For instance, it has been stressed that a very high number of spin degrees of freedom is usually present in the solid state environment. Coupling to such a spin-bath might limit the dephasing times of Josephson qubits (see e. g. the review and recent work by Prokof'ev and Stamp [21, 22]), and these effects themselves are very interesting for further study. Also here it is clear that a study of for example the dephasing due to spin impurities remains impossible as long a reliable measurement scheme for the loop's quantum

dynamics is not available. Therefore, we will concentrate here on dephasing and mixing due to the experimental wiring and the measurement scheme itself.

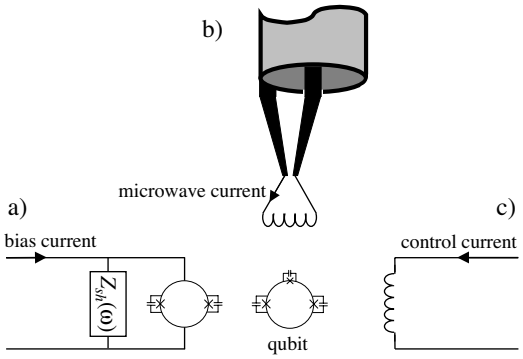

Figure 4.1: Experimental setup for measurements on a Josephson persistent-current qubit. The qubit (center) is a superconducting loop that contains three Josephson junctions. It is inductively coupled to a DC-SQUID (a), and superconducting control lines for applying magnetic fields at microwave frequencies (b) and static magnetic fields (c). The DC-SQUID is realized with an on-chip shunt circuit with impedance Z_{sh}. The circuits a)-c) are connected to filtering and electronics (not drawn).

Our analysis mainly focuses on experiments with the three-junction persistent-current qubit proposed by Mooij *et al.*, [16, 17, 9], in a setup where they are measured by underdamped DC-SQUID magnetometers (in this chapter we will reserve the word SQUID for the measuring DC-SQUID (Fig. 4.1a), and not use it for the three-junction qubit (Fig. 4.1center)). The decohering influence of the inductively coupled DC-SQUID is analyzed as well as decoherence that results from inductive coupling to on-chip control lines for applying microwave signals and local magnetic fields. Model descriptions of the experimental setup up will be mapped on the spin-boson model, such that we can use expressions for the relaxation and dephasing rates from the spin-boson literature. The results will be worked out quantitatively, and we will evaluate whether we can realize mixing and dephasing rates that are compatible with measurement schemes based on DC-SQUIDs. This work should also be of interest for experiments on loops with a single Josephson junction [8], and for similar experiments on quantum circuits where the charge degree of freedom is measured, as Josephson charge quantum

bits [15] and quantum dots [19]. In a more general context the value of this work is that it presents in detail an interesting example of a measurement process on a single quantum system in which the decoherence enhances with increasing measurement strength. The issues discussed here are an example of experimental difficulties that will unavoidably play a role in many realizations of quantum computers.

4.1.1 Outline

In section 2 we will summarize a theoretical description of the Josephson persistent current qubit, and the spin-boson theory that will be applied in our analysis. Section 3 presents a description of the measurement process with the DC-SQUIDs, and a typical scheme for coupling the qubit to the on-chip control lines. In section 4 we work out the qubit's relaxation and dephasing rate that result from the coupling to a switching DC-SQUID. This is worked out quite extensively and the definitions presented in this section are also valid for the consecutive sections. Two measurement scenarios with different types of electromagnetic shunt circuits for the DC-SQUID will be compared. A short analysis of the decoherence due to the coupling to on-chip control lines is presented in section 5.

4.2 Qubit Hamiltonian and theory for relaxation and dephasing

This work aims at calculating relaxation (mixing) rates and dephasing (decoherence) rates for a Josephson persistent-current qubit which result from its inductive coupling to the measurement setup. The measurement setup is formed by a DC-SQUID and control lines, which are attached to leads and coupled to filters and electronics (Fig. 4.1). This setup will be modeled as a macroscopic quantum two-level system that is coupled to an electromagnetic impedance $Z_t(\omega)$, where ω the angular frequency. The impedance $Z_t(\omega)$ can be described by a set of LC oscillators. This allows for mapping the problem on the spin-boson model: a central spin-$\frac{1}{2}$ system that is coupled to a bosonic bath [20, 41]. In this section we will first introduce the qubit Hamiltonian and physical properties of the qubit, and then summarize the spin-boson expressions for relaxation and dephasing.

4.2.1 Qubit properties and Hamiltonian

The three-Josephson junction qubit [16, 17, 9] is a low-inductance superconducting loop which contains three Josephson tunnel junctions (Fig. 4.1). By applying an external flux Φ_q a persistent supercurrent can be induced in the loop. For values where Φ_q is close to a half-integer number of superconducting flux quantums Φ_0, two states with persistent currents of opposite sign are nearly degenerate but separated by an energy barrier. We will assume here that the system is operated near $\Phi_q = \frac{1}{2}\Phi_0$. Classically, the persistent currents have here a magnitude I_p. Tunneling through the barrier causes a weak coupling between the two states, and the loop can be described by a Hamiltonian in the form of a two-level system,

$$H_q = \frac{\varepsilon}{2}\sigma_z + \frac{\Delta}{2}\sigma_x, \tag{4.1}$$

where σ_z and σ_x are Pauli spin operators. The two eigen vectors of σ_z correspond to states that have a left or a right circulating current and will be denoted as $|L\rangle$ and $|R\rangle$. The energy bias $\varepsilon = 2I_p(\Phi_q - \frac{1}{2}\Phi_0)$ is controlled by the externally applied field Φ_q. We follow [23] and define Δ as the tunnel splitting at $\Phi_q = \frac{1}{2}\Phi_0$, such that $\Delta = 2W$ with W the tunnel coupling between the persistent-current states. This system has two energy eigen values $\pm\frac{1}{2}\sqrt{\Delta^2 + \varepsilon^2}$, such that the level separation ν gives (see also Fig. 3.2).

$$\nu = \sqrt{\Delta^2 + \varepsilon^2}. \tag{4.2}$$

In the experiments Φ_q can be controlled by applying a magnetic field with a large superconducting coil at a large distance from the qubit, but for local control one can apply currents to superconducting control lines, fabricated on-chip in the direct vicinity of the qubit. The qubit's quantum dynamics will be controlled with resonant microwave pulses (i. e. by Rabi oscillations). The proposed operation point is at $\varepsilon \approx 5\Delta$. For optimal microwave control the qubit will be placed in a small cavity, and the microwave signals will be applied through on-chip superconducting control lines (i. e. the magnetic component of the fields from microwave currents will be used). The qubit has a magnetic dipole moment as a result of the clockwise or counter-clockwise persistent current, which commutes with σ_z. In the experiments this signal will be used for measuring the qubit states. Our system also has electric dipole moments, that commute with σ_x. However, the coupling to the DC-SQUID and the control lines is mainly inductive, and we will therefore neglect couplings between the environment and the electric dipole moments in the analysis presented here.

4.2.2 Spin-boson theory for dephasing and relaxation

For defining the relaxation and dephasing rates, the state of the qubit is described with a reduced density matrix $\overline{\rho}$, in the basis which is spanned by the eigen vectors of σ_z in (4.1).

$$\overline{\rho} = \begin{pmatrix} \rho_{L,L} & \rho_{R,L} \\ \rho_{L,R} & \rho_{R,R} \end{pmatrix}. \tag{4.3}$$

The relaxation rate Γ_r is the rate at which the populations (diagonal elements) of $\overline{\rho}$ go to their equilibrium values (Boltzmann factors in the eigen state basis). The dephasing rate Γ_ϕ is the rate at which the coherences (off-diagonal elements) of $\overline{\rho}$ go to zero. For estimating Γ_r and Γ_ϕ we will work from an article by Grifoni *et al.* [23], which covers recent theoretical progress for the spin-boson theory. Grifoni *et al.* calculated expressions for Γ_r and Γ_ϕ for a spin-boson system in which the coupling to the environment is dominated by bilinear coupling terms between σ_z and the bath coordinates. This is a good approximation for a quantum two-level system that is only weakly damped by the environment. In our case the bath is formed by the impedance $Z_t(\omega)$, and can be described by a set of LC oscillators with flux coordinates Φ_i, conjugate charge coordinates Q_i, and Hamiltonian $H_{bath} = \sum_i (\Phi_i^2/2L_i + Q_i^2/2C_i)$. The flux produced by the qubit will shift the flux Φ_i in each LC oscillator. The coupling Hamiltonian is $H_{q-bath} = \frac{\sigma_z}{2} \sum_i c_i \Phi_i$, where c_i is the coupling strength to the i-th oscillator. In this model the influence of the oscillator bath on the qubit can be captured in the environmental spectral density function

$$J(\omega) = \frac{\pi}{2\hbar} \sum\nolimits_i \left(c_i^2/C_i\omega_i\right) \delta(\omega - \omega_i), \tag{4.4}$$

where ω_i the resonance frequency of the i-th oscillator. The high number of degrees of freedom in the electromagnetic environment allows for treating $J(\omega)$ as a continuous function.

The relaxation rate Γ_r (and relaxation time τ_r) are determined by environmental spectral density $J(\omega)$ at the frequency of the level separation ν of the qubit [23]

$$\Gamma_r = \tau_r^{-1} = \frac{1}{2} \left(\frac{\Delta}{\nu}\right)^2 J(\nu/\hbar) \coth\left(\frac{\nu}{2k_B T}\right), \tag{4.5}$$

where T is the temperature of the bath. The dephasing rate Γ_ϕ (and dephasing time τ_ϕ) is [23]

$$\Gamma_\phi = \tau_\phi^{-1} = \frac{\Gamma_r}{2} + \left(\frac{\varepsilon}{\nu}\right)^2 \alpha\, 2\pi \frac{k_B T}{\hbar}. \tag{4.6}$$

The second term only contributes for an Ohmic environment (i. e. for $J(\omega) \propto \omega$). Here α is a dimensionless dissipation parameter. It is determined by the slope of $J(\omega)$ at low frequencies

$$\alpha = \lim_{\omega \to 0} \frac{J(\omega)}{2\pi\omega}, \tag{4.7}$$

which can usually be taken as $\alpha = \frac{1}{2\pi}\frac{\partial J(\omega)}{\partial \omega}$ at $\omega \approx 0$. These expressions for relaxation and dephasing have also been found by studying the Hamiltonian of our qubit coupled to a damped oscillator, using a Markovian master equation approach by Tian *et al.* [24] (based on work by Garg *et al.* [25]).

The expressions (4.5) and (4.6) have prefactors $\left(\frac{\Delta}{\nu}\right)^2$ and $\left(\frac{\varepsilon}{\nu}\right)^2$ that depend on the tunnel splitting Δ and the energy bias ε. These factors account for the effect that the qubit's magnetic dipole radiation is strongest where the flux in the qubit $\Phi_q = \frac{1}{2}\Phi_0$ (i. e. $\left(\frac{\Delta}{\nu}\right)$ maximal), and that the level separation ν is insensitive to flux noise at this point (i. e. $\frac{\partial\nu}{\partial\varepsilon} = \left(\frac{\varepsilon}{\nu}\right) \approx 0$). One should know and control $J(\omega)$ at the frequency $\nu/\hbar$ for controlling the relaxation, and at low frequencies for controlling the dephasing. In this chapter we will calculate the noise properties of a few typical experimental environments, and calculate how the noise couples to the qubit. This can be used to define $J(\omega)$ for our specific environments.

4.3 Measurement setup

This section describes an experimental setup for measurements on Josephson persistent-current qubits. Only the parts that are most strongly coupled to the qubit will be worked out (Fig. 4.1). The first part describes a DC-SQUID magnetometer that is used by measuring its switching current, the second part addresses the use of on-chip superconducting lines for applying magnetic fields to the qubit.

4.3.1 Switching DC-SQUID

SQUIDs are the most sensitive magnetometers, and they can be operated at very low power consumption [26]. We will consider here the use of a DC-SQUID with a hysteretic current-voltage characteristic (IV), and unshunted junctions that are extremely underdamped. It is used by ramping a current through it and recording the switching current: the bias current at which it switches from the supercurrent branch to a nonzero voltage in its IV (Fig. 4.2). The switching current is a measure for the magnetic flux in the loop of the SQUID. An important advantage of

this scheme is that the SQUID produces before readout very little noise. As long as the SQUID is on the supercurrent branch, it does not produce any shot noise or Josephson oscillations. If the external noise and interference can be suppressed by filtering, there is only Johnson-Nyquist noise from the low-temperature leads and filtering that the SQUID is connected to. At low frequencies this residual noise has little power since the device is superconducting. Moreover, we will show in section 4 that at low bias currents the effective coupling between this meter and the quantum system is very weak. In comparison, damped non-hysteretic SQUIDs have the problem that the shunt resistors at the junctions also provide a damping mechanism for the qubit. In a hysteretic SQUID there is more freedom to engineer the effective impedance seen by the qubit, and it also has the advantage that the voltage jump at the switching current is much larger [31]. The Saclay group has presented a similar scheme with a superconducting single-charge device, that can be operated as a switching electrometer [27]. Voltage biased single-electron transistors for quantum measurements have been analyzed in Refs. [28, 29].

For qualitative insight in the measurement process we will present here a simplified description of the SQUIDs noise and dynamics (valid for a DC-SQUID with symmetric junctions and a loop with negligible self inductance). In section 4 it will be worked out in more detail. The supercurrent through the SQUID with a flux Φ in its loop is

$$I_{sq} = 2I_{co} \cos f \ \sin \varphi_{ext}, \tag{4.8}$$

where $f = \pi\Phi/\Phi_0$, I_{co} the critical current of the junctions, and φ_{ext} a Josephson phase coordinate (it will be distinguished from the applied bias current I_{bias}, as part of the bias current may go into circuitry shunting the SQUID). Insight in the SQUID's response to a bias current is achieved by recognizing that (4.8) gives steady state solutions ($\partial U/\partial\varphi_{ext} = 0$) for a particle with coordinate φ_{ext}, trapped on a tilted washboard potential (Fig. 4.3)

$$U = -\frac{\hbar}{2e}\left(2I_{co} \cos f \ \cos \varphi_{ext} + I_{sq}\varphi_{ext}\right). \tag{4.9}$$

In this picture, the average slope of the potential is proportional to the bias current, and the supercurrent branch of the SQUID's IV corresponds to the particle being trapped in a well. The Josephson voltage across the SQUID $V = \frac{\hbar}{2e}\frac{d\varphi_{ext}}{dt}$ is nonzero for the particle in a running mode. In absence of noise and fluctuations, the SQUID will switch to the running mode at the critical current

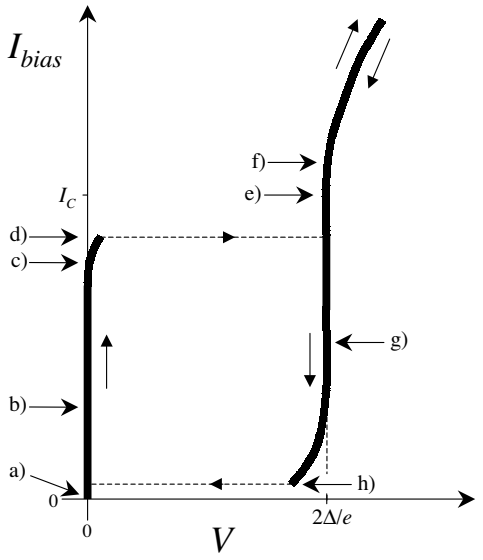

Figure 4.2: Sketch of a typical hysteretic current-voltage characteristic (IV) for a current-biased Josephson junction or small DC-SQUID. The IV is hysteretic; arrows indicate which of the two branches is followed at an increase or decrease of the bias current. When the bias current I_{bias} is ramped up from zero (a), the voltage V first remains zero. The circuit is here on the supercurrent branch of the IV (b). When I_{bias} approaches the critical current I_C, a slow diffusive motion of the phase φ_{ext} leads to a very small voltage across the system (c). At slightly higher current (d), but always below I_C (e), the system switches to a running mode for φ_{ext}, and the voltage jumps to a value set by quasiparticle tunneling over the superconducting gap, $V = 2\Delta/e$ (this current level (d) is the switching current I_{SW}). At further increase of the current (f) the IV approaches an Ohmic branch, where transport is dominated by quasiparticle tunneling through the normal tunnel resistance of the junctions. When lowering the bias current the system follows the running mode (g) down to a low bias current where it retraps on the supercurrent branch (at the level I_{retrap}, indicated by (h)). See also the corresponding washboard potential model, in Fig. 4.3.

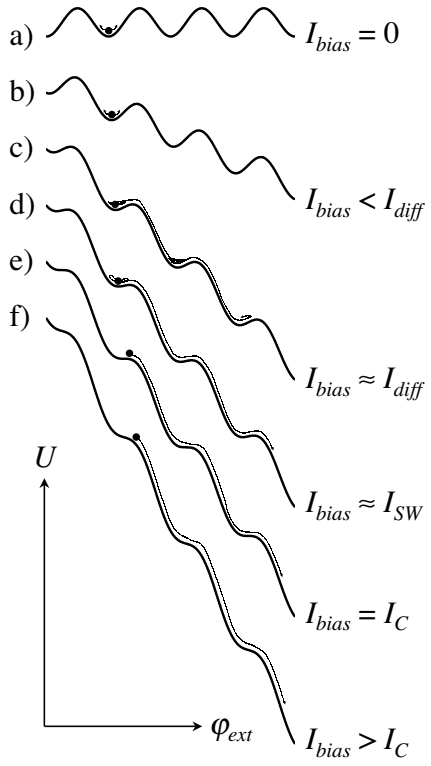

Figure 4.3: The dynamics of a current-biased DC-SQUID, modeled as a particle with coordinate φ_{ext} in a one-dimensional tilted washboard potential U. The labeling a)-f) corresponds to that of Fig. 4.2. At zero (a) and small bias currents (b), the particle is trapped in a well of the washboard. Apart from the small plasma oscillations at the bottom of the well, the particle's coordinate φ_{ext} is fixed. When increasing the slope of the washboard, the particle will start to have a slow, on average downwards, diffusive dynamics, with rare excursions to one of the neighboring wells (c). At the switching current I_{SW} there is a high probability that the trapped particle will escape to a running mode (d), with effectively zero probability for retrapping. Here the loss of potential energy exceeds the dissipation when the particle moves one period down the washboard, and the particle builds up a high kinetic energy. Due to thermal fluctuations, external noise, and in certain cases quantum fluctuations, this occurs below the critical current I_C: the slope where all local minimums in the washboard potential disappear (e). At currents higher than this slope (f), the particle will always be in a running mode. The retrapping process when lowering the bias current follows similar dynamics.

I_C

$$I_C = 2I_{co}\,|\cos f|\,. \tag{4.10}$$

A DC-SQUID can thus be regarded as a single Josephson junction with a flux-tunable critical current. In practice, noise and fluctuations of φ_{ext} will cause the SQUID to switch before the bias current reaches I_C. This current level will be denoted as the switching current I_{SW} to distinguish it from I_C. It is a stochastic variable, but averaging over repeated recordings of I_{SW} allows for determining f with great accuracy. This naive description can be used to illustrate three important properties of the measurement process with the SQUID.

In the experiment, the electronics for recording the SQUID's IV obtains information about f when the SQUID switches. However, rewriting (4.8) as

$$\varphi_{ext} = \sin^{-1}\left(\frac{I_{sq}}{2I_{co}\cos f}\right) \tag{4.11}$$

shows that the SQUID's coordinate φ_{ext} is already correlated with the flux f at current values below I_{SW}. Small voltage fluctuations that result from small plasma oscillations and translations of φ_{ext} will cause dissipation in the electromagnetic environment of the SQUID, which damps the dynamics of φ_{ext}. This means, that in a quantum mechanical sense, the position of φ_{ext}, and thereby f, is measured by the degrees of freedom that form the electromagnetic impedance that is shunting the SQUID (i. e. the leads and filtering between the SQUID and the readout electronics), and that the measurement may in fact take place before it is recorded by a switching event.

Secondly, (4.11) shows that the SQUID's coordinate φ_{ext} is independent of the flux in the loop ($\partial\varphi_{ext}/\partial f = 0$) for $I_{sq} = 0$. Therefore, in absence of fluctuations of φ_{ext} and current noise, the meter is at zero current effectively off. In practice this can of course not be realized, but it illustrates that the decoherence from the SQUID may be strongly reduced at low bias currents.

Thirdly, for bias currents well below I_C, the coordinate φ_{ext} is trapped in a potential that is for small oscillations close to harmonic. The SQUID can in this case be regarded as an inductance

$$L_J = \frac{\hbar}{2e}\frac{1}{\sqrt{4I_{co}^2\cos^2 f - I_{sq}^2}} \tag{4.12}$$

(see also (4.24) below). The noise from the SQUID can here be described by the Johnson-Nyquist noise from the SQUID's Josephson inductance (4.12) in

parallel with the SQUID's environmental impedance (Fig. 4.3a, b). For high bias currents very close to I_C, the spectrum will have more power and calculating the noise properties will be more complicated. Here non-harmonic terms in the trapping potential become important, and there maybe additional noise from a diffusive motion of φ_{ext} to neighboring wells (Fig. 4.3c). For hysteretic SQUIDs this regime with diffusive motion of φ_{ext} and switching currents very close to I_C will only occur in SQUIDs with a very specific electromagnetic shunt [30, 31]. In many realizations of hysteretic DC-SQUIDs φ_{ext} will escape to a running mode without retrapping in lower wells (Fig. 4.3d), and I_{SW} can be much lower than I_C. In this case the approximation using (4.12) should be valid for description of the noise before a switching event.

The statistics of I_{SW} readouts depend strongly on the damping of the dynamics of φ_{ext} by the impedance that is shunting the SQUID. Experimental control over the damping, requires the fabrication of a shunt circuit in the direct vicinity of the SQUID, such that its impedance is well defined up to the frequency of the SQUID's plasma oscillations (microwave frequencies). The shunt circuit is therefore preferably realized on-chip (Z_{sh} in Fig. 4.1a). The escape from the well may be thermally activated, but for underdamped systems with low-capacitance junctions quantum tunneling through the barrier can dominate the escape rate at low temperatures. The influence of the damping circuitry on the I_{SW} statistics [5, 30, 31] is now well understood. A SQUID with very underdamped dynamics usually has I_{SW} values much below I_C, and histograms of a set of I_{SW} recordings will be very wide. This means that one needs to average over many repeated measurements to achieve the required resolution in readout. Thereby, averaging also needs to take place over many repeated experiments on the qubit, such that only a time-ensemble average can be measured. With a shunt that provides high damping at the plasma frequency very narrow switching currents can be realized [30, 31], that might allow for single-shot readout in qubit experiments. However, in such a scheme the SQUID's noise will also be enhanced.

The main disadvantage of the switching SQUID is that it is not very efficient. During each cycle through the hysteretic IV it is only measuring for a short time. Moreover, the IV is very nonlinear, such that the repetition frequency must be an order lower than the bandwidth of the filters. The filtering that is required for realizing low effective temperatures and the SQUID's shunt circuit have typically a bandwidth well below 1GHz, and the accurate readout electronics set a similar limit to the bandwidth. In practice this limits the repetition frequency to values in the range of 10 kHz [9, 42] to 1 MHz [7, 40]. A more efficient readout may

be realized by placing the SQUID in an inductance bridge, described in the next section.

The slow operation of the switching DC-SQUID sets requirements for the mixing rate Γ_r of the qubit. It needs be longer than the time required to perform a switching current measurement, which requires a time in the range 1 μs to 100 μs. One could go to shorter times by setting the SQUID ready at a high bias current when an experiments on the qubit is started, but it is also needed to have the mixing time longer than the time it takes to ramp the bias current through the range of the switching current histogram. At the same time we should realize that the quantum system is prepared by waiting for it to relax to the ground state, so relaxation times very much longer than 100 μs will prohibit a high repetition frequency. A high repetition frequency is needed if the signal can only be build up by averaging over many switching events.

The experiments aim at working with many coherent Rabi oscillations with a period of about 10 ns [16], We therefore aim at engineering SQUIDs that cause a dephasing time that is much longer than 10 ns. The dephasing and relaxation times turn out to be shortest at high bias currents through the SQUID. Unless mentioned otherwise, we will make in this chapter worst case estimates for the dephasing and relaxation times using bias current values near the switching current.

4.3.2 On-chip control lines

An attractive feature of macroscopic qubits is that one can address individual qubits with control signals from microfabricated lines (see also Fig. 4.1b,c). For persistent-current qubits, for example, a supercurrent through a line that is mainly coupled to one specific qubit can be used for tuning this qubit's energy bias ε. Also, it is convenient to provide the microwave signals for control of the qubit's quantum dynamics using local superconducting lines. If this is realized in a microwave cavity with its first resonance well above the applied microwave frequency, one can apply microwave bursts with fast switch times without being hindered by high-Q electromagnetic modes in the volume that is formed by the cold metallic shielding that surrounds the sample.

Microwave signals can be applied using external microwave sources at room temperature. Alternatively, on-chip oscillators for example based on Josephson junction circuits [32, 33] can be applied. High microwave currents in the control lines are achieved by shorting the microwave coax or wave guide close to the qubit

with an inductance that has an impedance much lower than the source's output impedance (Fig. 4.1b). For external microwave sources, the typical level for the output impedance will be that of the available coax technology, typically 50 Ω. With on chip Josephson oscillators the typical output impedance is one order lower. In both cases, it is in practice very tedious to engineer these impedance levels and our analysis below will show that this forms a severe constraint for qubit experiments: long decoherence times are in conflict with the wish for local qubit control and low power levels of the applied microwave signals.

If one uses external microwave sources at room temperature it is harder than for the quasi DC signals to filter out the high temperature noise. Low effective temperatures can be achieved by a combination of narrow-band microwave filters and strong attenuators at low temperatures.

4.4 Relaxation and dephasing from a switching DC-SQUID

4.4.1 Current-phase relations for the DC-SQUID

The DC-SQUID has two phase degrees of freedom, the gauge-invariant phases γ_r and γ_l of the junctions. They are related to the supercurrents through the left and the right junction,

$$\begin{aligned} I_l &= (I_{co} + \tfrac{\Delta I_{co}}{2}) \sin \gamma_l, \\ I_r &= (I_{co} - \tfrac{\Delta I_{co}}{2}) \sin \gamma_r. \end{aligned} \tag{4.13}$$

Here I_{co} is the average of the critical current of the two junctions. A small asymmetry in the junctions' critical currents is accounted for by $\Delta I_{co} \ll I_{co}$ (typically a few percent). We will work here with the sum and difference phase coordinates φ_{int} and φ_{ext}, which are related by a linear transformation

$$\begin{array}{ll} \varphi_{ext} = \frac{\gamma_l + \gamma_r}{2} & \gamma_l = \varphi_{ext} + \varphi_{int} \\ \varphi_{int} = \frac{\gamma_l - \gamma_r}{2} & \gamma_r = \varphi_{ext} - \varphi_{int} \end{array} \quad \Leftrightarrow \quad . \tag{4.14}$$

The new phase coordinates are related with the current passing through the SQUID I_{sq} and the circulating current in the SQUID I_{cir}

$$\begin{array}{ll} I_{sq} = I_l + I_r & I_l = \frac{1}{2} I_{sq} + I_{cir} \\ I_{cir} = \frac{I_l - I_r}{2} & I_r = \frac{1}{2} I_{sq} - I_{cir} \end{array} \quad \Leftrightarrow \quad , \tag{4.15}$$

yielding the following current-phase relation for I_{sq} and I_{cir}

$$I_{sq} = 2I_{co}\cos\varphi_{int}\sin\varphi_{ext} + \Delta I_{co}\sin\varphi_{int}\cos\varphi_{ext}, \tag{4.16}$$

$$I_{cir} = I_{co}\sin\varphi_{int}\cos\varphi_{ext} + \frac{1}{2}\Delta I_{co}\cos\varphi_{int}\sin\varphi_{ext}. \tag{4.17}$$

Up to time scales much faster than $\frac{\hbar}{\nu}$ the internal phase follows the flux adiabatically , so below we will use

$$\varphi_{int} = \pi\frac{\Phi}{\Phi_0} \stackrel{def}{=} f. \tag{4.18}$$

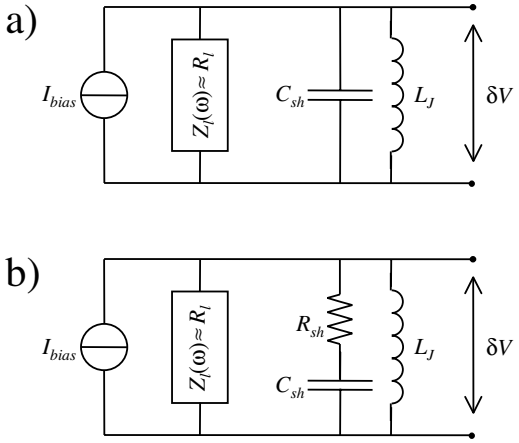

Figure 4.4: Circuit models for the C-shunted DC-SQUID (a) and the RC-shunted DC-SQUID (b). The SQUID is modeled as an inductance L_J. A shunt circuit, the superconducting capacitor C_{sh} or the R_{sh}-C_{sh} series, is fabricated on chip very close to the SQUID. The noise that couples to the qubit results from Johnson-Nyquist voltage noise δV from the circuit's total impedance Z_t. Z_t is formed by a parallel combination of the impedances of the leads Z_l, the shunt and the SQUID, such that $Z_t = (1/Z_l + 1/(R_{sh} + 1/i\omega C_{sh}) + 1/i\omega L_j)^{-1}$, with $R_{sh} = 0$ for (a).

4.4.2 Noise on the qubit from the DC-SQUID resulting in $J(\omega)$

The noise that is induced by the measuring SQUID results from Johnson-Nyquist noise of the total impedance $Z_t(\omega)$ between the leads that are attached to the

SQUID. The impedance $Z_t(\omega)$ is formed the SQUID's impedance in parallel with the impedance of the wiring and circuitry that the SQUID is connected to (see the circuit models in Fig. 4.4). At bias currents well below the critical current I_C the SQUID can be modeled as an inductor L_J. The coupling of φ_{ext} to the SQUID's inner degree of freedom and thereby to the qubit slightly alter the effective value for L_J, but the correction it is so small that it can be neglected. The power spectrum $\langle \delta V \ \delta V \rangle_\omega$ of the Johnson-Nyquist voltage fluctuations δV across the SQUID is [41, 34]

$$\langle \delta V \ \delta V \rangle_\omega = \hbar\omega \mathrm{Re}\{Z_t(\omega)\} \coth\left(\frac{\hbar\omega}{2k_B T}\right). \tag{4.19}$$

We will now calculate how this voltage noise leads to fluctuations $\delta\varepsilon$ of the energy bias on the qubit. The current-phase relations for I_{sq} and I_{cir} can be used for expressing the current fluctuations. The first term of (4.16) gives

$$\frac{dI_{sq}}{dt} = i\omega I_{sq} \approx 2I_{co}\cos f \cos\bar{\varphi}_{ext}\frac{d\varphi_{ext}}{dt} = 2I_{co}\cos f\cos\bar{\varphi}_{ext}\frac{2e}{\hbar}V, \tag{4.20}$$

where we used $\bar{\varphi}_{ext}$ for the time average of φ_{ext}. With a similar expression for the second term of (4.16) the current fluctuations in I_{sq} are

$$\delta I_{sq} \approx (2I_{co}\cos f\cos\bar{\varphi}_{ext} - \Delta I_{co}\sin f\sin\bar{\varphi}_{ext})\ \delta\varphi_{ext}. \tag{4.21}$$

The SQUID is usually operated in regions where the average external flux in its loop is between an integer and half-integer number of Φ_0. At these points $|\cos f| \approx |\sin f|$. Therefore, the second term in (4.21) can be neglected unless $|I_{co}\cos\bar{\varphi}_{ext}| \lessapprox |\Delta I_{co}\sin\bar{\varphi}_{ext}|$. That is, it can be neglected unless the bias current is very high, for which for which $\sin\bar{\varphi}_{ext}$ approaches 1. For most purposes we can thus use

$$\delta I_{sq} \approx 2I_{co}\cos f\cos\bar{\varphi}_{ext}\,\delta\varphi_{ext}. \tag{4.22}$$

This is also used to define L_J by expressing

$$V = L_J\frac{dI_{sq}}{dt}, \tag{4.23}$$

such that with (4.20), (4.18) and (4.16) L_J should be defined as

$$L_J = \frac{\hbar}{2e}\frac{1}{2I_{co}\cos f\cos\bar{\varphi}_{ext}} = \frac{\hbar}{2e}\frac{1}{\sqrt{4I_{co}^2\cos^2 f - I_{sq}^2}}. \tag{4.24}$$

For I_{cir} we get a similar expression as (4.21)

$$\delta I_{cir} \approx (-I_{co} \sin f \sin \bar{\varphi}_{ext} + \frac{1}{2} \Delta I_{co} \cos f \cos \bar{\varphi}_{ext})\ \delta\varphi_{ext}. \tag{4.25}$$

Using again that the SQUID is operated where $|\cos f| \approx |\sin f|$ shows that the second term in (4.25) can be neglected unless $|I_{co} \sin \bar{\varphi}_{ext}| \lessapprox |\Delta I_{co} \cos \bar{\varphi}_{ext}|$. For δI_{cir} the second term only plays a role at low bias currents in the SQUID for which $\bar{\varphi}_{ext} \approx 0$, and for most purposes we can use

$$\delta I_{cir} \approx -I_{co} \sin f \sin \bar{\varphi}_{ext}\ \delta\varphi_{ext}. \tag{4.26}$$

In the above we used $\bar{\varphi}_{ext}$ for the time average of φ_{ext}, but at places where it is not confusing it will be simply denoted as φ_{ext}.

Both noise in I_{sq} and I_{cir} can couple to the qubit, but will assume that the qubit is mainly sensitive to noise in I_{cir} (as in the experiments in [9], where the qubit was placed symmetrically inside the SQUID's loop) and neglect an inductive coupling to noise in I_{sq}. For a more general approach, coupling to noise in I_{sq} can be treated on a similar footing as noise in I_{cir}, but for all useful sample geometries it should give a contribution to relaxation and dephasing rates that is at most on the same order as that of I_{cir}.

With $i\omega\delta I_{cir} = -\frac{2e}{\hbar} I_{co} \sin f \sin \varphi_{ext}\ \delta V$ follows for the fluctuations δI_{cir}

$$\langle \delta I_{cir}\ \delta I_{cir} \rangle_\omega = \left(\frac{2e}{\hbar}\right)^2 \frac{1}{\omega^2} I_{co}^2 \sin^2 f \sin^2 \varphi_{ext}\ \langle \delta V\ \delta V \rangle_\omega \quad . \tag{4.27}$$

The fluctuations in the imposed qubit flux are $\delta\Phi_q = M\delta I_{cir}$, where M the mutual inductance between the SQUID loop and the qubit loop. This then yields the fluctuations in the energy bias with $\delta\varepsilon = 2I_p\delta\Phi_q$,

$$\langle \delta\varepsilon\ \delta\varepsilon \rangle_\omega = \left(\frac{2e}{\hbar}\right)^2 \frac{4}{\omega^2} M^2 I_p^2 I_{co}^2 \sin^2 f \sin^2 \varphi_{ext}\ \langle \delta V\ \delta V \rangle_\omega. \tag{4.28}$$

Using (4.16) and (4.19) and filling in $\frac{\hbar}{2e} = \Phi_0$ this can be written as

$$\langle \delta\varepsilon\ \delta\varepsilon \rangle_\omega = \hbar\,(2\pi)^2 \frac{1}{\omega} \left(\frac{MI_p}{\Phi_0}\right)^2 I_{sq}^2 \tan^2 f\ \mathrm{Re}\{Z_t(\omega)\} \coth\left(\frac{\hbar\omega}{2k_BT}\right) \tag{4.29}$$

The fluctuations $\langle \delta\varepsilon\ \delta\varepsilon \rangle_\omega$ are the result of the coupling to the oscillator bath, as in (4.4). This can be used to define $J(\omega)$ for our specific environment,

$$J(\omega) = \frac{(2\pi)^2}{\hbar} \frac{1}{\omega} \left(\frac{MI_p}{\Phi_0}\right)^2 I_{sq}^2 \tan^2 f\ \mathrm{Re}\{Z_t(\omega)\}. \tag{4.30}$$

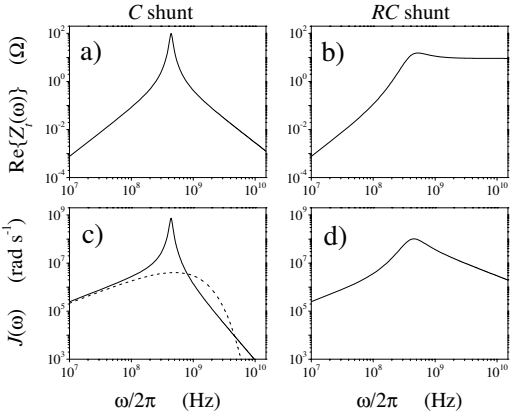

Figure 4.5: A typical $\mathrm{Re}\{Z_t(\omega)\}$ for the C-shunted SQUID (a) and the RC-shunted SQUID (b), and corresponding $J(\omega)$ in (c) and (d) respectively. For comparison, the dashed line in (c) shows a simple Ohmic spectrum (4.41) with exponential cut off $\omega_c/2\pi = 0.5$ GHz and $\alpha = 0.00062$. The parameters used here are $I_p = 500$ nA and $T = 30$ mK. The SQUID with $2I_{co} = 200$ nA is operated at $f = 0.75\,\pi$ and current biased at 120 nA, a typical value for switching of the C-shunted circuit (the RC-shunted circuit switches at higher current values). The mutual inductance $M = 8$ pH (i. e. $\frac{MI_p}{\Phi_0} = 0.002$). The shunt is $C_{sh} = 30$ pF and for the RC shunt $R_{sh} = 10\ \Omega$. The leads are modeled by $R_l = 100\ \Omega$.

4.4.3 Relaxation times

With (4.5) and (4.30) follows the SQUID's contribution to the relaxation rate. It is here expressed as a function of the resonance frequency $\omega_{res} = \nu/\hbar$ at which the qubit is operated,

$$\Gamma_r = \left(\frac{\Delta/\hbar}{\omega_{res}}\right)^2 \frac{(2\pi)^2}{2\hbar} \frac{1}{\omega_{res}} \left(\frac{MI_p}{\Phi_0}\right)^2 I_{sq}^2 \tan^2 f\ \mathrm{Re}\{Z_t(\omega_{res})\} \coth\left(\frac{\hbar\omega_{res}}{2k_BT}\right). \tag{4.31}$$

In this formula one can recognize a dimensionless factor $\left(\frac{MI_p}{\Phi_0}\right)^2$ which is a scale for how strongly the qubit is coupled to the measuring SQUID. A dissipation factor in the form I^2R can be recognized in $I_{sq}^2 \tan^2 f\ \mathrm{Re}\{Z_t(\omega)\}$. The dissipation scales with the absolute value of the current fluctuations, so with I_{sq}, and the expression is independent of critical current of the SQUID junctions I_{co} (unless

$\mathrm{Re}\{Z_t(\omega)\}$ depends on I_{co}). A weak measurement scheme in which the inductive coupling to a DC-SQUID $(MI_p/\Phi_0)^2 << 1$ can yield relaxation rates that are very low when compared to a scheme in which leads are directly attached to the loop [35]. A measurement of such a scheme's switching current could also be used for probing the qubit, but the influence of the voltage noise would be dramatically worse.

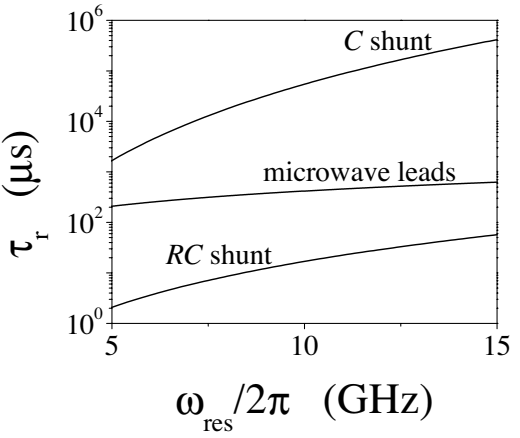

Figure 4.6: Typical relaxation times due to the C-shunted SQUID, the RC-shunted SQUID, and coupling the microwave leads as a function of the resonance frequency at which the qubit is operated. The example of the microwave leads contribution is for a mutual inductance M_{mw} to the coaxial line of $M_{mw} = 0.1$ pH. Parameters are further as described in the caption of Fig. 4.5.

With the result (4.31) the relaxation rate for typical sample parameters will be calculated. Sample parameters similar to our recent experiment [9] are $\omega_{res} =$ 10 GHz, $\Delta = 2$ GHz, $\frac{MI_p}{\Phi_0} = 0.002$. It is assumed that a SQUID with $2I_{co} =$ 200 nA is operated at $f = 0.75\ \pi$ and biased near the switching current, at $I_{sq} = 120$ nA. For $T = 30$ mK the relaxation rate per Ohm environmental impedance is then

$$\tau_r = \Gamma_r^{-1} \approx \frac{150\ \mu\mathrm{s}\,\Omega}{\mathrm{Re}\{Z_t(\omega_{res})\}}. \tag{4.32}$$

4.4.4 Engineering $\mathrm{Re}\{Z_t(\omega)\}$

In practice the SQUID's resolution is improved by building an on-chip electromagnetic environment. We will consider here a large superconducting capacitive shunt (Fig. 4.4a, as in our recent experiment [9]). This scheme will be denoted as the C-shunted SQUID. As an alternative we will consider a shunt that is a series combination of a large capacitor and a resistor (Fig. 4.4b). This will be denoted as the RC-shunted SQUID. The C shunt only makes the effective mass of the SQUID's external phase φ_{ext} very heavy. The RC shunt also adds damping at the plasma frequency of the SQUID, which is needed for realizing a high single-readout resolution of the SQUID (i. e. for narrow switching-current histograms) [31]. The total impedance $Z_t(\omega)$ of the two measurement circuits are modeled as in Fig. 4.4. We assume a perfect current source I_{bias} that ramps the current through the SQUID. The fact that the current source is non-ideal, and that the wiring to the SQUID chip has an impedance is all modeled by the impedance Z_l. We can engineer the wires such that for a very wide frequency range the impedance Z_l is on the order of the vacuum impedance, and can be modeled by its real part R_l. It typically has a value of 100 Ω. On chip we have the Josephson inductance L_J in parallel with the shunt circuit (C_{sh}, or the series combination of R_{sh} and C_{sh}). We thus assume that the total impedance $Z_t(\omega)$ can be described as

$$Z_t(\omega) = \left(\frac{1}{i\omega L_J} + \frac{1}{\frac{1}{i\omega C_{sh}} + R_{sh}} + \frac{1}{R_l} \right)^{-1}, \tag{4.33}$$

where R_{sh} should be taken zero for the C shunt scenario.

The circuits in Fig. 4.4 are damped LC resonators. It is clear from (4.5) and (4.30) that one should keep the LC-resonance frequency $\omega_{LC} = 1/\sqrt{L_J C_{sh}}$, where $\mathrm{Re}\{Z_t(\omega)\}$ has a maximum, away from the qubit's resonance $\omega_{res} = \nu/\hbar$. For practical values this requires $\omega_{LC} \ll \omega_{res}$ [For Aluminum technology, with a Niobium based chip as at MIT can be realized with $\omega_{LC} \gg \omega_{res}$]. This then gives the circuits a $\mathrm{Re}\{Z_t(\omega)\}$ and $J(\omega)$ as plotted in Fig. 4.5. For the circuit with the C shunt

$$\mathrm{Re}\{Z_t(\omega)\} \approx \begin{array}{ll} \frac{\omega^2 L_J^2}{R_l}, & \text{for } \omega \ll \omega_{LC} \\ R_l, & \text{for } \omega = \omega_{LC} \\ \frac{1}{\omega^2 C_{sh}^2 R_l}, & \text{for } \omega \gg \omega_{LC} \end{array} \tag{4.34}$$

For the circuit with the RC shunt

$$\mathrm{Re}\{Z_t(\omega)\} \approx \begin{array}{ll} \frac{\omega^2 L_J^2}{R_l}, & \text{for } \omega \ll \omega_{LC} \\ \lesssim R_l, & \text{for } \omega = \omega_{LC} \ll \frac{1}{R_{sh}C_{sh}} \\ R_l//R_{sh}, & \text{for } \omega = \omega_{LC} \gg \frac{1}{R_{sh}C_{sh}} \\ R_l//R_{sh}, & \text{for } \omega \gg \omega_{LC} \end{array} \tag{4.35}$$

The difference mainly concerns frequencies $\omega > \omega_{LC}$, where the C-shunted circuit has a $\mathrm{Re}\{Z_t(\omega)\}$, and thereby a relaxation rate, that is several orders lower than for the RC-shunted circuit.

For a C-shunted circuit with $\omega_{LC} \ll \omega_{res}$ the $\mathrm{Re}\{Z_t(\omega_{res})\} \approx \frac{1}{\omega_{res}^2 C_{sh}^2 R_l}$. This yields for $J(\omega)$ at $\omega > \omega_{LC}$

$$J(\omega) \approx \frac{(2\pi)^2}{\hbar}\frac{1}{\omega^3}\left(\frac{MI_p}{\Phi_0}\right)^2 I_{sq}^2 \tan^2 f \, \frac{1}{C_{sh}^2 R_l} \tag{4.36}$$

The factor $1/\omega^3$ provides a natural cut off for $J(\omega)$ (much of the literature [20, 23] introduces an artificial cut off to prevent an ultraviolet divergence with an Ohmic bath). The RC-shunted circuit has softer cut off $1/\omega$. The mixing rate for the C-shunted circuit is then

$$\Gamma_r \approx \frac{(\Delta/\hbar)^2}{\omega_{res}^5}\frac{(2\pi)^2}{2\hbar}\left(\frac{MI_p}{\Phi_0}\right)^2 I_{sq}^2 \tan^2 f \, \frac{1}{C_{sh}^2 R_l} \coth\left(\frac{\hbar\omega_{res}}{2k_B T}\right). \tag{4.37}$$

Fig. 4.6 presents mixing times τ_r vs ω_{res} for typical sample parameters (here calculated with the non-approximated version of $\mathrm{Re}\{Z_t(\omega)\}$). With the C-shunted circuit it seems possible to get τ_r values that are very long. They are compatible with the ramp times of the SQUID, but too slow for fast repetition rates. In Fig. 4.5 one can directly see from the values of $J(\omega)$ that an RC-shunted circuit with otherwise similar parameters yields at $\omega_{res}/2\pi = 10$ GHz relaxation times that are about four orders shorter. For the parameters used here they are in the range of 15 μs. When considering that this does not yet account for the fact that the switching currents will be higher, and that the corresponding noise properties will be worse, this seems on the low side.

4.4.5 Comparing the C shunt and the RC shunt scenario

The estimate (4.32) shows that to be on the safe side for reasonable relaxation rates in a typical measurement scheme, one should have at ω_{res} an impedance with $\mathrm{Re}\{Z_t(\omega_{res})\} \lesssim 1\ \Omega$. It also shows that one could allow for a higher $\mathrm{Re}\{Z_t(\omega_{res})\}$ (and thereby possibly narrower switching current histograms) by

making M smaller. Taking half the value of M allows for a four times higher $\mathrm{Re}\{Z_t(\omega_{res})\}$ (resulting in the same mixing time), but also requires (at fixed histogram width) four times more samples (the SQUID resolution is proportional to the square root of the number of switching events). So, if a higher $\mathrm{Re}\{Z_t(\omega_{res})\}$ goes along with substantial narrowing of the histograms one can improve the measurement efficiency. However, the SQUID will then also switch at higher I_{sq}, (say at 0.95 instead of 0.7 of the critical current, such that it reduces τ_r again, but only by a factor $\left(\frac{0.7}{0.95}\right)^2 \approx 0.54$). Moreover, our description here assumes noise from a linearized Josephson inductance. This may not be valid for bias currents close to the critical current, and it seems that the real noise would lead to stronger dephasing and mixing than estimated here [44, 36] due to noise from the dynamics of $\cos\varphi$ instead of φ for the diffusive washboard motion near switching. An advantage of the RC shunt would be that it will give a better defined environment experimentally. It is possible to reliably control the values of C_{sh} and R_{sh}, such that one has in a wide frequency range a very well defined and "zero-fit parameter" environment.

4.4.6 Dephasing times

At low frequencies $\omega < \omega_{LC}$ the C-shunted and RC-shunted scheme have $\mathrm{Re}\{Z_t(\omega)\} \approx \frac{\omega^2 L_J^2}{R_l}$ such that with (4.30) and (4.7)

$$J(\omega) \approx \frac{(2\pi)^2}{\hbar}\omega \left(\frac{MI_p}{\Phi_0}\right)^2 I_{sq}^2 \tan^2 f \, \frac{L_J^2}{R_l}, \tag{4.38}$$

$$\alpha \approx \frac{2\pi}{\hbar} \left(\frac{MI_p}{\Phi_0}\right)^2 I_{sq}^2 \tan^2 f \, \frac{L_J^2}{R_l}. \tag{4.39}$$

The environment at low frequencies Ohmic since we have $J(\omega) \propto \omega$. For our sample parameters the second term in (4.6) dominates, such that with (4.39) and for the qubit operated where $\varepsilon \approx \nu$

$$\Gamma_\phi \approx \frac{(2\pi)^2}{\hbar^2} \left(\frac{MI_p}{\Phi_0}\right)^2 I_{sq}^2 \tan^2 f \, \frac{L_J^2}{R_l} \, k_B T. \tag{4.40}$$

Note in (4.24) that $L_J \propto 1/I_{co}$, such that the dephasing rate (4.40) does not depend on the absolute value of the current, but on the ratio I_{sq}/I_C. For the typical sample parameters as used in Fig. 4.5 the dephasing time is about 10 ns, which is too short. However, we can gain a few orders (if Γ_r is low enough) by

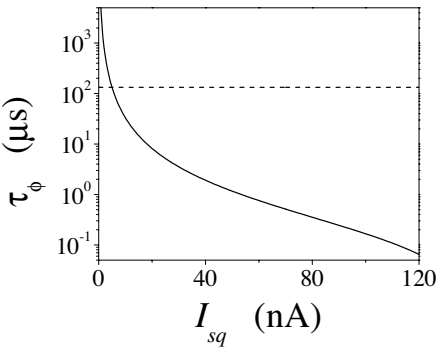

Figure 4.7: The dephasing time (4.40) as a function of the bias current I_{sq} through the SQUID, calculated for a relevant environmental frequency scale $\omega_\alpha/2\pi < 10^7$ Hz (solid line). The dashed line shows τ_ϕ for $I_{sq} = 5$ nA, a typical minimum value for the effective bias current for a SQUID with a few percent asymmetry between its junctions. At this point $\tau_\phi = 131$ μs, and $\alpha = 1 \cdot 10^{-7}$. Parameters are further as described in the caption of Fig. 4.5.

the fact that we can do the quantum coherent control at low I_{sq} (the previous estimate was calculated for $I_{sq} = 120$ nA, in the switching region). At $I_{sq} = 0$ we find $\Gamma_\phi = 0$ in this linear approximation for the SQUID inductance. At $I_{sq} = 0$ we should therefore estimate the dephasing due to second order terms. However, in practice the dephasing is probably dominated by the second term in (4.25), which is due to a small asymmetry in the fabricated SQUID junctions of a few percent. This influence can be mapped on a small bias current (a few percent of the critical current, say 5 nA) through the SQUID. Therefore, at $I_{sq} \approx 0$ the dephasing times can be $\left(\frac{120}{5}\right)^2$ times longer. Furthermore, the factor L_J^2, as defined in (4.24), is at 5 nA about a factor 2 lower than at 120 nA. For our parameters this allows for $\tau_\phi \approx 20$ μs, see also Fig. 4.7. We can also realize $R_l =$ 1 kΩ, work with a somewhat lower M or tune the qubit to $\frac{\varepsilon}{\nu} < 1$ to get longer dephasing times.

4.4.7 Comparison to Ohmic noise spectrum and the influence of resonance peaks

In the literature on dissipative two-level systems one often assumes Ohmic dissipation, corresponding to a purely resistive shunt across the junctions of the qubit. For a description of such a system one usually introduces an artificial exponential cut off at frequency ω_c, yielding $J(\omega)$ of the form

$$J(\omega) = \frac{\alpha}{\hbar^2}\omega \exp(-\frac{\omega}{\omega_c}). \tag{4.41}$$

To be able to relate our results to this literature we plot in Fig. 4.5 such a $J(\omega)$ which resembles the $J(\omega)$ due to the DC-SQUID. For the parameters as in Fig. 4.5 the resemblance is reasonable for a resistive shunt corresponding to $\alpha = 0.00062$, and a cut off $\omega_c = 0.5$ GHz. For low currents, as for the dashed line in Fig. 4.7 $\alpha = 1 \cdot 10^{-7}$. This corresponds to an extremely underdamped system, with a long dephasing time. However, very recent work by Wilhelm *et al.* [43] studied dephasing and relaxation rates for a structured environment, and found that the rates can deviate up to a factor of 50 for typical sample parameters. A detailed evaluation based on this theory is in progress.

4.4.8 Conclusions for DC-SQUID analysis

Both measurements schemes, with the C-shunted SQUID and the RC-shunted SQUID, can be engineered to cause relaxation and dephasing rates that are low enough for experiments on the coherent quantum dynamics of the qubits. The dependence of the relaxation rates on the factors $\frac{1}{\omega_{res}^5}\tan^2 f$ (for the C shunt) or $\frac{1}{\omega_{res}^3}\tan^2 f$ (for the C shunt) allow for in situ checking of theory for Γ_r, unless it is dominated by other contributions (e. g. the on-chip control lines) The dependence on the factor $\left(\frac{\varepsilon}{\nu}\right)^2 I_{sq}^2 \tan^2 f\ T$ gives several knobs for in situ checking of theory for Γ_ϕ, in a situation where this rate dominates the dephasing.

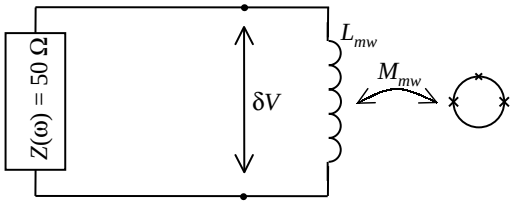

Figure 4.8: Circuit model for coaxial line that is inductively coupled to the qubit. The coaxial line is modeled as a 50 Ω impedance that is shorted near the qubit with an inductance L_{mw}. The qubit is coupled to this short with a mutual inductance M_{mw}. The noise that couples to the qubit results from Johnson-Nyquist voltage noise δV from the circuit's total impedance Z_t, formed by a parallel combination of the 50 Ω impedance and L_{mw}.

4.5 Relaxation and dephasing from on-chip control circuits

4.5.1 Dephasing and relaxation times due to the microwave leads

We will treat here the influence of noise from the microwave leads in a similar way as worked out for the SQUID. Here the total environmental impedance $Z_t(\omega)$ is formed by a 50 Ω coax, that is shorted at the end by a small inductance L_{mw}, see the circuit model in Fig. 4.8. This inductance L_{mw} has a mutual inductance M_{mw} to the qubit. The voltage noise is given by (4.19). The noise leads to fluctuations $\delta\varepsilon$ of the energy bias separation ε as follows. The current noise in L_{mw} is $\delta I_L = \frac{1}{i\omega L_{mw}}\delta V$. The qubit fluctuations in the flux Φ_q are then $\delta\Phi_q = M_{mw}\delta I_L$, and the fluctuations in the energy bias are $\delta\varepsilon = 2I_p\delta\Phi_q$. This gives for the fluctuations $\langle\delta\varepsilon\ \delta\varepsilon\rangle_\omega$

$$\langle\delta\varepsilon\ \delta\varepsilon\rangle_\omega = \frac{4\hbar}{\omega}\left(\frac{M_{mw}I_p}{L_{mw}}\right)^2 \mathrm{Re}\{Z_t(\omega)\}\coth\left(\frac{\hbar\omega}{2k_BT}\right) \tag{4.42}$$

and for the environmental spectral density (4.4) is now

$$J(\omega) = \frac{4}{\hbar\omega}\left(\frac{M_{mw}I_p}{L_{mw}}\right)^2 \mathrm{Re}\{Z_t(\omega)\}. \tag{4.43}$$

The $\mathrm{Re}\{Z_t(\omega)\}$ is that of a first order low-pass LR filter with a -3 dB frequency $\omega_{LR} = R/L$. For the L_{mw} to be effectively a short its impedance ωL_{mw} should

be small compared to 50 Ω at the frequency of the applied microwave radiation (typically 10 GHz), giving $L_{mw} \ll 1\,\mathrm{nH}$. This can be realized by making the length of the short line less than about 100 μm. This means that all relevant frequencies are below the -3 dB frequency ω_{LR}, and that for both relaxation and dephasing we can approximate

$$\mathrm{Re}\{Z_t(\omega)\} \approx \frac{\omega^2 L_{mw}^2}{R_{mw}} \tag{4.44}$$

with $R_{mw} = 50\,\Omega$. For $\omega < \omega_{LR}$, $J(\omega)$ is again Ohmic,

$$J(\omega) = \frac{4\omega}{\hbar}\frac{(M_{mw}I_p)^2}{R_{mw}}, \tag{4.45}$$

and with (4.7) we find for α

$$\alpha \approx \frac{4}{2\pi\hbar}\frac{(M_{mw}I_p)^2}{R_{mw}}. \tag{4.46}$$

Note that these results are independent of L_{mw}. A larger L_{mw} leads to enhanced voltage noise, but the resulting current noise is reduced by the same factor. For frequencies below ω_{LR} the current noise is just that of a shorted 50 Ω resistor. For frequencies higher than ω_{LR}, $\mathrm{Re}\{Z_t(\omega)\} \approx R_{mw}$, such that $J(\omega)$ has a very soft intrinsic $1/\omega$ cut off.

For the relaxation rate (4.5) as a function of the qubit's resonance frequency ω_{res} we now have

$$\Gamma_r \approx \frac{2\Delta^2}{\hbar^3\omega_{res}}\frac{(M_{mw}I_p)^2}{R_{mw}}\coth\left(\frac{\hbar\omega_{res}}{2k_BT}\right). \tag{4.47}$$

This has a much weaker dependence on ω_{res} than for the SQUID, results are plotted in Fig. 4.6. The results are plotted for $M_{mw} = 0.1\,\mathrm{pH}$ (further parameters as used for the SQUID calculations) and for this M_{mw} value the relaxation times are in the required range of about 100 μs. The value $M_{mw} \approx 0.1$ pH corresponds to a 5 μm loop at about 25 μm distance from the microwave line, and is compatible with the fabrication possibilities and the microwave requirements. With this geometry it is still possible to apply enough microwave power for pumping the qubit's Rabi dynamics at 100 MHz (i. e. pumping with an oscillating Φ_q of about 0.001 Φ_0, so with an oscillating current of $\frac{0.001\,\Phi_0}{M_{mw}} \approx 20\,\mu$A, corresponding to 20nW, i. e. −47dBm microwave power), while the dissipated microwave power in the attenuators at the mixing chamber remains well below 1 μW.

For the second term of the dephasing rate (4.6) we thus find for the qubit operated where $\varepsilon \approx \nu$

$$\Gamma_\phi \approx \frac{4}{\hbar^2}\frac{(M_{mw}I_p)^2}{R_{mw}}\,k_B T. \tag{4.48}$$

This is for all frequencies $\omega < \omega_{LR}$ independent of some relevant frequency scale ω_α. Using the same parameters as in the above calculation of the relaxation time we find $\alpha \approx 1 \cdot 10^{-7}$ and with $T = 30\,\mathrm{mK}$

$$\Gamma_\phi \approx 126\,\mu\mathrm{s}. \tag{4.49}$$

This is a very reasonable dephasing time for the first experiments. For the long term quantum computation goals this seems on the short side, and we have little parameters to play with! It in practice quite tedious to apply microwave technology with impedance levels much higher than 50 Ω, both for externally generated microwaves and on chip generators (it could for instance be increased using a planar transformer [37]). For our initial experiments, simplest option then seems to make M_{mw} very small. This, however, also requires higher microwave currents, and thereby more microwave dissipation on the mixing chamber. The cooling power per qubit will quite likely remain below 1 μW, so much stronger microwave signals from a larger distance is not an option. Moreover, making M_{mw} very small means that the control line is 100μm or further away from the qubit. It is then much harder to apply microwaves very locally to one specific qubit on a chip with several coupled qubits.

4.5.2 Conclusions for microwave dephasing and relaxation

Local control, an important advantage for the microfabricated qubit, is very hard to realize when low-impedance control lines are used. However, for layouts that can be used in the first experiments, Γ_r and Γ_ϕ have very promising values. The estimate for Γ_r is more robust than the estimate from the DC-SQUID analysis. This can be for engineering a reliable Γ_r, when the Γ_r from a C-shunted SQUID, for example, is very low.

4.6 Suppressing rates by freezing states and idle states

Bringing the qubit in an idle state ($\varepsilon = 0$) [15] can reduce dephasing, but not beyond Γ_r. Also, at $\varepsilon = 0$, Γ_r can be enhanced.

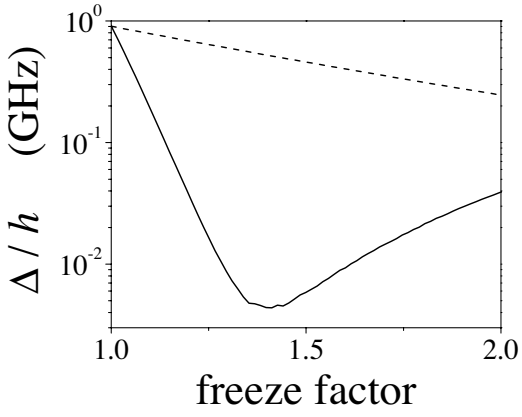

Figure 4.9: Numerically simulated suppression of Δ in qubits where one (solid) or three (dashed) of the junctions are realized as small DC-SQUIDs. The horizontal axis is the factor by which the Josephson energy of the relevant junctions is increased.

Freezing the qubit before measurement with a fast but adiabatic control current allows for much slower measurements, thus for weaker coupling to a damped SQUID with very high resolution. Moreover, it has the advantage that the tunnel coupling becomes so week that the Hamiltonian almost commutes with σ_z. This can improve the correlation between the outcome of σ_z measurements, and energy states in the case that the calculation states are energy eigen states. However, freezing requires that the qubit junctions are realized as small DC-SQUID's. This means that σ_x noise will be strongly enhanced. The Grifoni paper assumes dominant σ_z noise, so this may then no longer be valid. See also Fig. 4.9 for numerical estimates on the possible adiabatic suppression of Δ.

4.7 Discussion

We observed in our last experiment (Chapter 3)that $\tau_r \leqq 10\,\mu$s for $\omega_{res}/2\pi \approx 6$ GHz. This was checked by giving microwaves pulses of a few microseconds before the bias current reached the histogram. This barely agrees with an estimate using the theory presented here (only when one assumes that C_{sh} was a bit lower than estimated, say 1 pF instead of the estimates 2 pF, and that the resistors in the leads were not very effective at 6 GHz, such that R_l was 100 Ω instead

of 2 kΩ, the theory gives τ_r in the range of 10 μs). New experiments that are running at the moment of this writing, have pulsed microwave control with nanosecond resolution. Preliminary results indicate that the relaxation time is a few microseconds. With the theory in this chapter, we estimated a relaxation time longer than 100 microseconds for the current sample parameters. However, in this new experiment we also found that uncontrolled oscillations were present in the signal wires connected to the input of the amplifying electronics. After reducing these effects, the relaxation time increased by a factor of six. Further studies need to be made before conclusions can be reached.

The theory itself is also still in development. We already mentioned the efforts of Wilhelm *et al.* [43], aimed at analyzing rates for a structured environment (i. e. a sharply peaked $J(\omega)$). Furthermore, it is not clear whether the impedance can be described by a single temperature. At low frequencies, noise from parts in the system with a higher temperature can reach the sample.

Taken this all together, suggests that it is wise to design for τ_r which is on the high side of the required 100 μs. This is very well possible with the C shunt (but then one needs a second mechanism to avoid too slow relaxation, for example from coupling to the microwave lines). With the RC shunt it is only possible in combination with for example a reduction of M.

The authors thank D. Esteve, M. Grifoni, Y. Nakamura, P. C. E. Stamp, A. C. J. ter Haar, L. Levitov, T. P. Orlando, L. Tian, and S. Lloyd for help and stimulating discussions. Financial support by the Dutch Foundation for Fundamental Research on Matter (FOM), the European TMR research network on superconducting nanocircuits (SUPNAN), the USA National Security Agency (NSA) and Advanced Research and Development Activity (ARDA) under Army Research Office (ARO) contract number DAAG55-98-1-0369, and the NEDO joint research program (NTDP-98) is acknowledged.

References

[1] E. Schödinger, *Naturwissenschaften* **23**, 807-812, 823-828, 844-849 (1935).

[2] P. W. Anderson, in *Lectures on the Many-Body Problem*, E. R. Caianiello, Ed. (Academic Press, New York, 1964), vol. 2, pp. 113-135.

[3] A. J. Leggett, *Prog. Theor. Phys. Suppl.* **69**, 80 (1980).

[4] K. K. Likharev, *Sov. Phys. Usp.* **26**, 87 (1983).

[5] John Clarke, Andrew N. Cleland, Michel H. Devoret, Daniel Esteve, John M. Martinus, *Science* **239**, 992 (1988).

[6] S. Han, R. Rouse, J. E. Lukens, *Phys. Rev. Lett.* **76**, 3404 (1996).

[7] P. Silvestrini, V. G. Palmieri, B. Ruggiero, M. Russo, *Phys. Rev. Lett.* **79**, 3046 (1997).

[8] J. R. Friedman, V. Patel, W. Chen, S. K. Tolpygo, J. E. Lukens, *Nature* **406**, 43 (2000).

[9] C. H. van der Wal *et al.*, *Science* **290**, 773 (2000).

[10] A. J. Leggett, A. Garg, *Phys. Rev. Lett.* **54**, 857 (1985).

[11] C. D. Tesche, *Phys. Rev. Lett.* **64**, 2358 (1990).

[12] Y. Nakamura, Yu. A. Pashkin, J. S. Tsai, *Nature* **398**, 786 (1999).

[13] M. F. Bocko, A. M. Herr, M. J. Feldman, *IEEE Trans. Appl. Supercond.* **7**, 3638 (1997).

[14] L. B. Ioffe, V. B. Geshkenbein, M. V. Feigel'man, A. L. Fauchère, G. Blatter, *Nature* **398**, 679 (1999).

[15] Yu. Makhlin, G. Schön, A. Shnirman, *Nature* **398**, 305 (1999).

[16] J. E. Mooij *et al.*, *Science* **285**, 1036 (1999).

[17] T. P. Orlando *et al.*, *Phys. Rev. B* **60**, 15398 (1999).

[18] One could also measure on an ensemble of loops, as shortly discussed in Chapter 1.

[19] T. H. Oosterkamp *et al.*, *Nature* **395**, 873 (1998).

[20] A. J. Leggett *et al.*, *Rev. Mod. Phys.* **59**, 1 (1987); *Rev. Mod. Phys.* **67**, 725(E) (1995).

[21] N. Prokof'ev, P. Stamp, *Rep. Prog. Phys.* **63**, 669 (2000); cond-mat/0001080.

[22] N. V. Prokof'ev, P. C. E. Stamp, *Spin-bath mediated decoherence in superconductors*, submitted to *Phys. Rev. Lett.*, (2000); cond-mat/0006054.

[23] M. Grifoni, E. Paladino, U. Weiss, *Eur. Phys. J. B* **10**, 719 (1999).

[24] L. Tian et al., preprint (2001).

[25] A. Garg, J. N. Onuchic, and V. Ambegaokar, *J. Chem. Phys.* **83**, 3391 (1985).

[26] M. Tinkham, *Introduction to Superconductivity* (McGraw-Hill, Inc., New York, ed. 2, 1996).

[27] A. Cottet *et al.*, preprint (Saclay, 2000).

[28] A. Shnirman and G. Schön, *Phys. Rev. B* **57**, 15400 (1998).

[29] M. H. Devoret and R, J, Schoelkopf, *Nature* **406**, 1039 (2000).

[30] D. Vion, M. Götz, P. Joyez, D. Esteve, M. H. Devoret, *Phys. Rev. Lett.* **77**, 3435 (1996).

[31] P. Joyez, D. Vion, M. Götz, M. H. Devoret, D. Esteve, *J. Supercond.* **12**, 757 (1999).

[32] A. K. Jain. K. K. Likahrev, J. E. Lukens, J. E. Sauvageau, *Phys. Rep.* **109**, 309 (1998).

[33] D. S. Crankshaw, E. Trías, T. P. Orlando, submitted to the *Proceedigs of the Applied Superconductivity Converence 2000*, (IEEE, 2001); available through http://w3.ascinc.org/.

[34] M. H. Devoret, in *Quantum Fluctuations*, S. Reynaud, E. Giacobino, J. Zinn-Justin, Eds. (Elsevier Science, Amsterdam, 1997), pp. 351-386.

[35] U. Geigenmüller. *J. Appl. Phys.* **80**, 3934 (1996).

[36] W. T. Coffey, Y. P. Kalmykov, J. T. Waldron, *The Langevin Equation; with Apllications in Chemistry and Electrical Engineering*, (World Scientific, Singapore, 1996).

[37] M. Feldman, private communications.

[38] Yuriy Makhlin, Gerd Schön, Alexander Shnirman, submitted to *Rev. Mod. Phys.* (2000); cond-mat/0011269.

[39] L. Tian *et al.*, in *Quantum Mesoscopic Phenomena and Mesoscopic Devices in Microelectronics*, I. O. Kulik, R. Ellialtioğlu, Eds. (Kluwer Academic Publishers, Dordrecht, 2000), pp. 429-438; cond-mat/9910062.

[40] D. Vion, private communication.

[41] U. Weiss, *Quantum Dissipative Systems*, (World Scientific, Singapore, ed. 2, 1999).

[42] W. Wernsdorfer, D. Mailly, A. Benoit, *J. Appl. Phys.* **87**, 5094 (2000).

[43] F. K. Wilhelm *et al.*, preprint (2001).

[44] D. Esteve, private communications.

Chapter 5

Controlled single-Cooper-pair charging effects in a small Josephson junction array

Abstract

We report on measurements of single-Cooper-pair charging effects in small Josephson junction arrays, and the experimental techniques that were used. We succeeded in having complete control over the array's electrostatic parameters; offset charges were accurately compensated, and the poisoning of $2e$-periodic effects by quasiparticles was circumvented. This allowed for a controlled study of the array's coherent ground state. A few measurements gave results which were not fully $2e$-periodic due to interesting parity effects. The arrays are in the regime where the energy scales for the Josephson effect and single-charge effects are comparable.

5.1 Introduction

Josephson junction arrays consist of small superconducting islands that are connected by tunnel junctions. In arrays of junctions with a very small capacitance C, single-charge effects play an important role [1]; fluctuations in the number of excess Cooper pairs on the islands are suppressed by the Coulomb charging energy of the islands. In the regime where the energy scale for the single-charge effects $E_C{=}e^2/2C$ is comparable to the Josephson energy E_J of the junctions, several macroscopic quantum phenomena have been observed [2, 3, 4, 5, 6]. These are a

This chapter is based on Ref. 1 on p. 111.

consequence of the conjugation relations between the array's macroscopic charge and phase variables.

In the regime with $E_J \approx E_C$, a quantum mechanical description of the array is needed. The macroscopic ground state can be described as a coherent superposition of charge configurations with a well-defined number of excess Cooper pairs on each island [3, 7]. In systems with only a few islands, the electrostatic energy of each of the charge configurations can be controlled by means of gate electrodes that are capacitively connected to the islands. It is then possible to control the form of the ground state. In superconducting double-junction circuits, a $2e$-periodic modulation of the maximum supercurrent that can flow through the circuit has been observed [3, 4]. Van Oudenaarden has observed a $2e$-periodic superconductor to Mott-insulator transition in a linear array with six islands [6].

In practice, two phenomena hamper a controlled study of the coherent superposition of charge configurations. One is the presence of background charges; each island is polarized by a random offset charge, caused by, e. g., impurities in the underlying substrate. Also, parity effects can be a problem; the presence of quasiparticles in the circuit suppresses the formation of a coherent ground state [3, 8]. The offset charges must be compensated by gate-induced charges, and the presence of quasiparticles needs to be circumvented.

In this chapter we present experimental results from measuring single-charge effects in small Josephson junction arrays, with complete control over the electrostatic parameters. Results were $2e$-periodic in the induced gate charges (Fig. 5.1a). Along with results we report on the experimental techniques that were used. The array was designed for studying charge–fluxoid duality [7]. Experimental results in light of these phenomena will be presented in the next chapter, see also [9]. The arrays consist of two small superconducting islands connected to each other and to macroscopic leads by small Josephson junctions with $E_J \lessapprox E_C$ (Figs. 5.3 and 5.4). The voltage V_g on capacitively connected gates controls the gate-induced charge $n_g = C_g V_g / 2e$ (this definition assumes that offset charges have been compensated already). Another control parameter for the array is the magnetic flux Φ threading the loops, but in this chapter we will focus on charging effects and limit ourselves to the case with $\Phi = 0$. We performed measurements on five different arrays (Table 5.1). The arrays were studied by measuring the maximum supercurrent that can flow through the array, called the switching current.

5.2 Fabrication and experimental setup

The arrays with Al–Al_2O_3–Al junctions of about $(100\ \text{nm})^2$ were fabricated with standard e-beam lithography in a double-layer resist and shadow evaporation techniques [10, 11]. Two successive aluminum layers were deposited (35 and 55 nm) on thermally oxidized Si substrates by e-beam evaporation. We used aluminum of 0.9999 purity or higher, and evaporated in a vacuum below 10^{-7} mbar

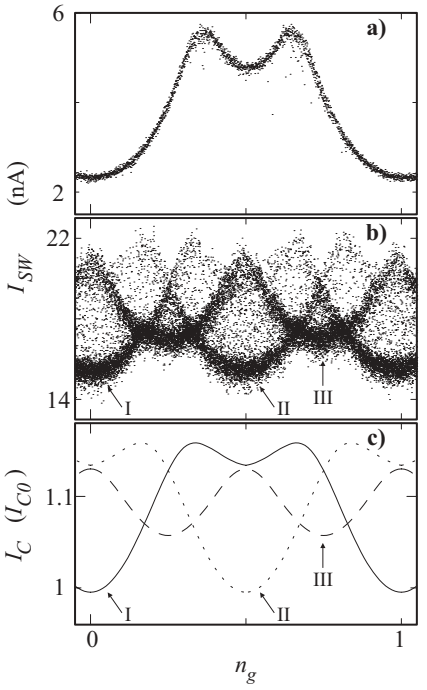

Figure 5.1: The switching current I_{SW} as a function of charge frustration. **a)** Results of 2000 individual switch events measured while slowly sweeping the induced charge n_g=$C_gV_g/2e$ on both gates simultaneously (array 3, Φ=0, T=70 mK). **b)** Results of 20000 individual switch events. Three levels appear due to parity effects, i. e., quasiparticles in the array (array 1, Φ=0, T=10 mK). **c)** Numerical simulations of the array's critical current I_C versus n_g (I_C in units of I_{C0}=$(2e/\hbar)E_J$), based on [7], with E_J/E_C=0.5. Trace I is for the (even–even) parity configuration, II is for (odd–odd), III is for (odd–even) and (even–odd).

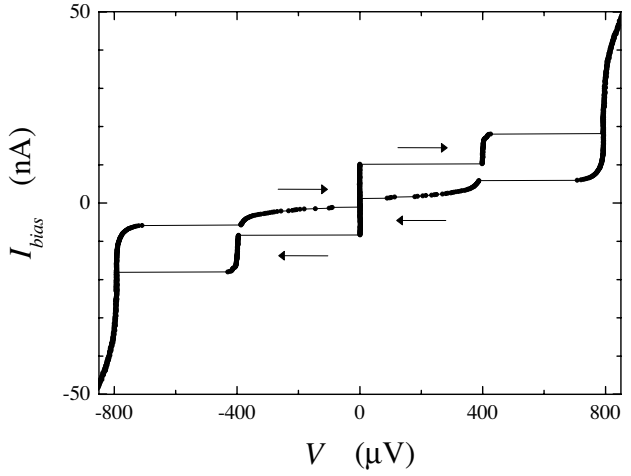

Figure 5.2: Current-voltage characteristic (IV) measured on array 1. The bias current I_{bias} where the array switches from the zero-voltage branch to a finite voltage is the switching current I_{SW}. Arrows indicate the direction of the hysteretic cycle in the IV.

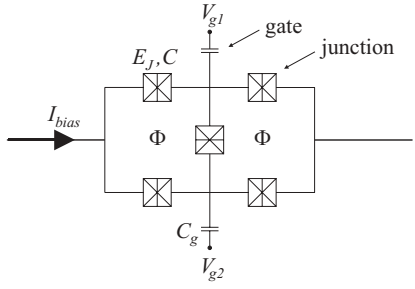

Figure 5.3: Schematic of the Josephson junction array. Two small superconducting electrodes are coupled to each other and to leads by small tunnel junctions. The junctions have equal Josephson coupling E_J and capacitance C. The voltage V_g on capacitively connected gates controls the gate-induced charge. The bias current I_{bias} is injected via macroscopic leads. A magnetic flux Φ can be applied to the loops.

(below 10^{-6} mbar during evaporation). The tunnel barriers were formed by exposing the first aluminum layer at room temperature to ≈0.1 mbar of pure O_2 for 5 min. The on-chip leads and pads for bonding were also made of aluminum and

deposited in this evaporation step. On arrays 2 and 3 we successively fabricated with a second lithography and evaporation step (60 nm SiO, 5 nm Ti, 25 nm Au) an on-chip CRC-network that was shunting the array. The layout was such that there was in the direct vicinity of the array an overlap of $(140\ \mu\text{m})^2$ with the array's bias leads on both sides. These two gold pads were connected by a 200-μm-long, 0.3-μm-wide gold line, which had a resistance of 3 kΩ at milliKelvin temperatures. The parallel plate capacitors had each a capacitance of about 10 pF [11]. This shunt network dissipates voltage oscillations created by the array at frequencies above $\approx$0.1 GHz, and is crucial for a clear observation of the zero-voltage supercurrent branch at low effective Josephson coupling [3]. With arrays 4 and 5, which did not have an on-chip CRC-environment, premature switching from the zero-voltage state occurred below 10 pA. These results were too noisy for observing charging effects.

The gates were surrounded by a grounded guard structure (Fig. 5.4a) to reduce the cross-capacitance between a gate electrode and the island on the other side of the array. With grounded guards the cross-capacitance was about 0.1 C_g. In a measurement where the guard was not grounded, but at the same potential as the gate electrode, the cross-capacitance was higher by a factor of 3.

Measurements on the arrays were performed in a dilution refrigerator with a base temperature below 10 mK. The samples were mounted on the cold finger in a microwave-tight copper box, surrounded by a sequence of low-temperature shields. All wires to the samples were filtered by copper powder filters at base temperature, and rfi-feedthrough filters at room temperature. The switching current was measured in a four-point setup. It was probed by dedicated low-noise electronics which ramps a bias current through the array, and records the value of the current at which the system switches from the zero-voltage supercurrent branch to a finite voltage. After switching the current is reduced to zero. A typical value for the ramp rate of the current was 10 nA/ms, at a repetition rate of 20 Hz. The voltage probes for the four-point wiring were connected on chip in the direct vicinity of the array (Fig. 5.4a). Voltages were amplified 20000 times by a battery-powered pre-amplifier in series with the dedicated electronics. With a noise floor of 0.4 μV RMS, the reference voltage for switching was set to 2 μV. The gates were connected via 1:100 voltage dividers at the mixing chamber (total resistance 1 MΩ, with a 150-Hz low-pass RC-filter). Additional optically decoupled 1:1 isolation amplifiers and 1 Hz low-pass RC-filters at room temperature improved the results of switching current measurements significantly (higher level, less scatter, and less parity effects).

5.3 Superconducting single-charge effects

Figure 5.1a shows a single period of the $2e$-periodic modulation of the switching current that we observed in arrays 2 and 3. The observed modulation is in very close agreement with results of numerical simulations (as level I in Fig. 5.1c, but with E_J/E_C as estimated for array 3), based on a quantum description of the array in the charge basis [7]. The presence of quasiparticles was successfully circumvented and, as will be discussed below, offset charges were compensated to within 0.01 of a $2e$ gate charge. Offset charges remained stable on a time scale of hours. This allowed for a study of the switching current while sweeping through the entire V_{g1}–V_{g2}-plane, and peak positions measured on arrays 2 and 3 demonstrated a clear honeycomb structure with a fundamental period of $2e$.

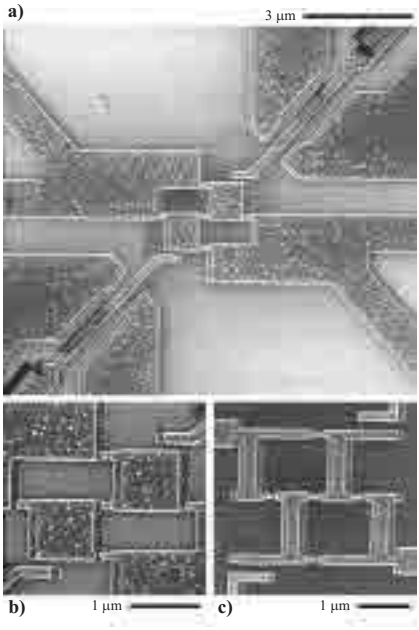

Figure 5.4: SEM-graphs of the array. In **a)** the two islands are in the center. From the top-left and bottom-right, leads are connected in a four-point setup. Two gate electrodes approach the array from the top-right and bottom-left, surrounded by grounded guard electrodes. The graphs below illustrate the difference in island shape between arrays 2 and 3 (graph **b)**), and arrays 1, 4 and 5 (graph **c)**).

Results from array 1, however (Fig. 5.1b), suffer from parity effects. We observed three distinct levels in the switching current as a function of gate charge, which we can relate to the presence of quasiparticles in the array. The array has two islands that can each have an even or odd charge state, giving four different parity configurations for the entire array. As illustrated in Fig. 5.1c, the presence of a quasiparticle on one of the islands is effectively the same as applying a gate charge of e. Level I (even–even) in Fig. 5.1b and 1c is equal to level II (odd–odd) shifted over a distance e. Level III is for the parity configurations (even–odd) and (odd–even). This interpretation was confirmed by measurements where both gates were swept simultaneously, but with a constant offset between n_{g1} and n_{g2}. Level III then split up into two different levels, again in very close agreement with simulations. The Saclay group observed very similar quasiparticle phenomena in an array with the same layout [12]. For each individual measurement of the switching current, the probability of finding the array in one of the four parity configurations was approximately equal. This indicates an interesting interplay between the measurement time scales and the time scales at which the parity of the array changes. It was indeed observed that the probability for measuring high levels of the switching current decreased with decreasing ramp rate of the bias current [12, 13].

Figure 5.5 illustrates how some parity effects remained present in arrays 2 and 3. Mostly around gate charges corresponding to $n_g{=}\frac{1}{2}$, the switching current was sometimes jumping between two distinct levels. The jumps were often to a value that corresponds to the level of the switching current at exactly e shifted in gate charge (Fig. 5.5c). Moreover, measurements in the normal state (superconductivity suppressed with a 1-T magnetic field) showed that the background charges were very quiet on the time scale of these jumps. This proves that jumps are due to parity effects, and not to random changes of offset charges in the background. An important difference with the parity effects of Fig. 5.1b is that the parity of the islands remains unchanged over many sequential switch events (Figs. 5.5b and 5.5c). Note that for each individual point in the traces of Figs. 5.1 and 5.5, the voltage over the array switched to the superconducting gap $2\Delta/e$. After each switch event, many quasiparticles are thus created in the array for a short time, but the parity configuration is usually not affected. This indicates that the parity effects involve tunneling of conduction electrons to localized states on the islands. This mechanism for parity effects was proposed by Eiles et al. after observing infrequent jumps of exactly e in the gate-charge dependence of a normal–superconductor–normal double junction circuit [14].

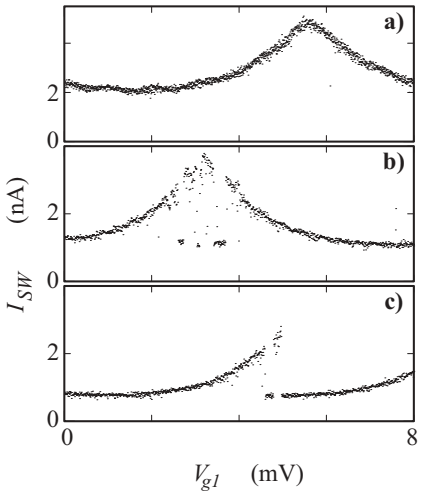

Figure 5.5: The switching current I_{SW} versus V_{g1}, with gate 2 at $n_{g2}\approx 0$. The V_{g1} voltage window corresponds to a gate charge of $2e$. In **a)**, $2e$-periodicity is not disturbed by quasiparticles (array 3, Φ=0, T=70 mK). In **b)** and **c)** $2e$-periodicity is disturbed by a quasiparticle jumping onto island 1, which results in two distinct levels in I_{SW} (array 2, Φ=0 Φ_0, T=30 mK). Graph **c)** illustrates that the additional level in I_{SW} is equal to the undisturbed level shifted over a distance e (4 mV).

The parity effects presented in Figs. 5.1b and 5.5 had a very weak temperature dependence up to $T\approx 150mK$. In array 3, e. g., the presence of quasiparticles in the array *decreased* when raising the temperature from 10 to 70 mK. Raising the temperature further, the parity effects changed drastically at $T^*\approx 150$ mK, in agreement with the odd–even free-energy model of Tuominen et al. [15, 16]. Here poisoning by thermally excited quasiparticles becomes dominant. The switching current turned e-periodic, and had much lower values. Also, the switching results had large scatter, instead of one or more distinct levels. To avoid quasiparticles in the system it is crucial to have the charging energy of the islands ($\approx E_C/3$) lower than the odd–even free energy difference D [15, 16]. At milliKelvin temperatures and for aluminum islands with dimensions as in Fig. 5.4, $D\approx\Delta$. Even though this requirement was satisfied in all the arrays (Table 5.1), the results of array 1 were strongly influenced by the parity effects, and also in arrays 2 and 3 some of the parity effects were observed. The argument that the occupation of odd charge states is very unlikely for $E_C/3 < \Delta$ assumes that the small superconducting

islands have a perfect BCS-gap. For small islands, however, it is hard to predict what the influence is of boundaries and impurities on the formation of the BCS-gap [17]. The islands in Fig. 5.4c have a thickness and width not much larger than the grain size of the evaporated aluminum. Also, due to the shadow evaporation technique, the island consists in fact of two islands on top of each other, connected by a very large tunnel junction [18]. In practice this may lead to quasiparticle states within the gap. For this reason, we changed the design of the islands for arrays 2 and 3 after the measurements on array 1.

The design of the island was changed from the branched structure of Fig. 5.4c (also the island shape of the device in Ref. [12], with parity effects) to the lumped shaped of Fig. 5.4b (also the island shape of the six-island arrays of Ref. [6], with little parity effects). This was done at the cost of a lower odd–even free-energy difference D due to the larger island volume. We found that in arrays 2 and 3 the quasiparticle presence was almost fully suppressed. This is an indication that the shape of mesoscopic islands plays a role in avoiding poisoning by quasiparticles. However, we cannot rule out that the on-chip CRC-environment in arrays 2 and 3 has influenced the relaxation rates for quasiparticles. We also cannot rule out that uncontrolled microscopic differences in the materials, e. g., impurities, have played a crucial role (array 1 was evaporated in a different setup than the other arrays).

The unexpected temperature dependence of quasiparticle poisoining was observed much more pronounced in later experiments in our group. In a linear Josephson junction array with six islands [5] and in superconducting double-junction circuits with a single island [19], $2e$ periodic behavior of the switching current was observed at temperatures around 100 mK. However, below 70 mK the switching current turned to e periodic behavior. This phenomena is not yet understood.

We developed a computer-controlled method which accurately compensates the offset charges, usually in a few minutes. We calibrated our gate charges by searching for gate values that give a minimum switching current for both gates simultaneously. This corresponds to finding the minimum in the honeycomb peak structure in a V_{g1}–V_{g2}-plane of $2e$ by $2e$. This was done in an iterative manner since the islands are capacitively coupled, and because of the presence of the small cross-capacitance. The gate capacitance of each island was determined accurately, such that we could sequentially sweep the voltage on one of the gates over a window corresponding to exactly $2e$. After the sweep the gate was left at the value for which the minimum in the switching current was found. When one

Array	E_J (μeV)	E_C (μeV)	E_J/E_C	Δ (μeV)	C_g (aF)	CRC-shunt	Filters and shielding	$e/2e$
1	71	$1.5 \cdot 10^2$	0.5	198	33	no	I and II	$e/2e$
2	31	$1.4 \cdot 10^2$	0.2	208	40	yes	II	2e
3	30	$1.5 \cdot 10^2$	0.2	209	40	yes	II	2e
4	16	$1.8 \cdot 10^2$	0.1	223	80	no	II	-
5	15	$1.9 \cdot 10^2$	0.1	220	80	no	II	-

Table 5.1: Properties of arrays 1–5. E_J was estimated from experimentally determined values of the tunnel resistance R and the gap Δ, using $E_J{=}h\Delta/8e^2R$. R and E_C were estimated from the differential resistance and the voltage offset in the high-bias IV [20]. Δ was directly measured in the low-bias IV. C_g was estimated from Coulomb oscillations in the normal state (applying a 1-T magnetic field) to avoid ambiguity about e or $2e$-periodicity. The last columns indicate the presence of an on-chip CRC shunt-network, what copper powder filter and shielding set was used, and whether results were e or $2e$-periodic. Filter set II proved effective for obtaining $2e$-periodicity from these measurements. Set I proved effective in the measurements of [4].

gate was at $n_g{\approx}0$, the modulation of the switching current by the other gate was as in Fig. 5.5a. We determined the minimum by searching for the maximum in the cross-correlation $\sigma[j]$ between the data and a phenomenological peak shape $\exp(-3.5|i - N/2|/N)$, where

$$\sigma[j]{=}\sum_{i=1}^{N} I_{SW}(V_g[i] - V_{off}[j]) \cdot \exp(-3.5|i - N/2|/N).$$

Here N is the number of measured switch events while sweeping over the $2e$-period, and i is an index for the sequence of measured I_{SW} at gate voltage $V_g[i]$. The index j is the running shift variable for the cross-correlation. The data set I_{SW} is shifted modulo the $2e$ gate-voltage window. We used $N{=}1000$. The advantage of this method is that it makes optimal use of all N measurements of a stochastic variable. Also, the method is very robust against a moderate presence of parity effects, as in Fig. 5.5b. We considered the offset charges successfully tuned away when the same offset voltages were found in five successive iteration steps. The criterion here was that the standard deviation of the five results was less then 0.01 of a $2e$-period. This accuracy was confirmed by independent observations from sweeping the gates over very long intervals.

In summary, we succeeded in measuring $2e$-periodic single-charge effects in a small Josephson junction array. The presence of quasiparticles in the array

was successfully suppressed in a few of the arrays. Our results indicate that processes on a long time scale, in which conduction electrons can be trapped in localized states in the islands, play an important role in the origin of parity effects in small superconducting islands. We developed a computer-controlled method which accurately compensates offset charges in the array.

We thank M. H. Devoret, P. Hadley, P. Lafarge and A. van Oudenaarden for stimulating discussions. This work was supported financially by the Dutch Foundation for Fundamental Research on Matter (FOM).

References

[1] For a review see *Single Charge Tunneling*, edited by H. Grabert and M. H. Devoret (Plenum Press, New York, 1992).

[2] W. J. Elion, J. J. Wachters, L. L. Sohn and J. E. Mooij, *Phys. Rev. Lett.* **71**, 2311 (1993).

[3] P. Joyez, P. Lafarge, A. Filipe, D. Esteve and M. H. Devoret, *Phys. Rev. Lett.* **72**, 2458 (1994).

[4] M. Matters, W. J. Elion and J. E. Mooij, *Phys. Rev. Lett.* **75**, 721 (1995).

[5] A. van Oudenaarden, S. J. K. Várdy and J. E. Mooij, *Czech. J. Phys.* **46**, suppl. S2, 707 (1996).

[6] Alexander van Oudenaarden, Ph. D. thesis, Delft University of Technology (1998).

[7] P. Lafarge, M. Matters and J. E. Mooij, *Phys. Rev. B* **54**, 7380 (1996).

[8] K. A. Matveev, M. Gisselfält, L. I. Glazman, M. Jonson and R. I. Shekhter, *Phys. Rev. Lett.* **70**, 2940 (1993).

[9] Caspar H. van der Wal and J. E. Mooij, submitted to *Phys. Rev. Lett.*

[10] G. J. Dolan and J. H. Dunsmuir, *Physica B* **152**, 7 (1988).

[11] E. H. Visscher, S. M. Verbrugh, J. Lindeman, P. Hadley and J. E. Mooij, *Appl. Phys. Lett.* **66**, 305 (1995).

[12] Vincent Bouchiat, Ph. D. thesis, Université Paris 6 (1997).

[13] Caspar H. van der Wal, internal report, Delft University of Technology (1996).

[14] T. M. Eiles, John M. Martinis and Michel H. Devoret, *Phys. Rev. Lett.* **70**, 1862 (1993).

[15] M. T. Tuominen, J. M. Hergenrother, T. S. Tighe and M. Tinkham, *Phys. Rev. Lett.* **69**, 1997 (1992).

[16] P. Lafarge, P. Joyez, D. Esteve, C. Urbina and M. H. Devoret, *Phys. Rev. Lett.* **70**, 994 (1993).

[17] Philippe Joyez, Ph. D. thesis, Université Paris 6 (1995).

[18] The intermediate oxide layer can usually be neglected in the analysis of single-electron devices with double-layer islands. In linear arrays double-layer islands can be avoided. Most of the $2e$-periodic results on double-junction circuits were measured on devices with a single-layer island [3, 4, 14, 15, 16].

[19] C. P. Heij, Ph. D. thesis, Delft University of Technology (to be published, 2001).

[20] P. Wahlgren, P. Delsing and D. B. Haviland, *Phys. Rev. B* **52**, R2293 (1995).

Chapter 6

Dual Charge and Vortex Superpositions in a Small Josephson Junction Array

Abstract

We studied the ground state of a small two-dimensional array of Josephson junctions, in which the charging energy is comparable to the Josephson coupling energy. Measurements of the array's critical supercurrent demonstrate that dual charge and vortex superpositions coexist in the array.

6.1 Introduction

Josephson junction arrays with underdamped low-capacitance junctions are model systems with non-commuting phase and number variables. The Josephson effect and single-charge effects have a competing influence on the array's ground state. We present an experiment on a small two-dimensional array that has a self-dual geometry: It can be described as two coupled islands with a high charging energy, but also as two coupled loops that can each contain a vortex (Fig. 6.1a). We succeeded in having experimental control over all magnetic and charge frustrations (Fig. 6.2). This allowed for a study of the array's quantum mechanical ground state, and our results demonstrate that charge and vortex superpositions occur in the array in a dual fashion.

We measured the array's critical supercurrent as a function of charge and magnetic frustration, symmetrically applied to both islands or loops. The charge frustration n_g of the two islands was controlled with capacitively coupled gate

This chapter is based on Ref. 9 on p. 111.

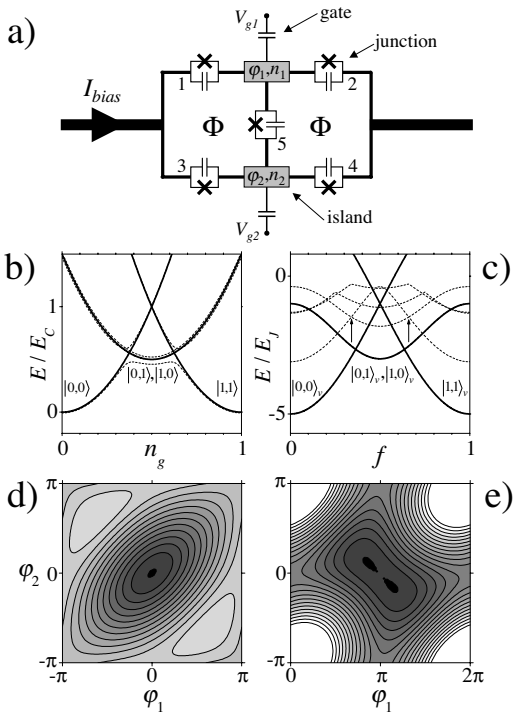

Figure 6.1: **a)** Schematic of the array. The Josephson junctions are modelled by the parallel combinations of the Josephson tunnel element (cross) and the junction capacitance. A bias current I_{bias} can be injected from macroscopic leads. **b)** The array's electrostatic energy vs. n_g (solid). The dashed lines are examples of eigen energies calculated for $E_J/E_C = 0.05$, $f = 0$ and $I_{bias} = 0$. **c)** The array's total Josephson energy vs. f (solid). The dashed lines are eigen energies calculated for $E_J/E_C = 2$, $n_g = 0$ and $I_{bias} = 0$. The arrows show that the distance between the level crossings is larger for the quantum levels. In **d)** and **e)** the total Josephson energy U_J vs. φ_1 and φ_2, on the same gray scale (black is low U_J). The plots are for $f = 0.364$, $I_{bias} = 0$, and $\delta = 0$ (d), and $\delta = \pi$ (e).

electrodes. The array's magnetic frustration $f = \Phi/\Phi_0$ was set by applying a magnetic flux Φ to the loops (Φ_0 is the flux quantum). The critical current as a function of n_g showed a periodic modulation with two maximums per period (Fig. 6.3a). The period corresponds to inducing a charge $2e$ on the islands. As a function of f we observed a periodic modulation with two minimums per

period (Fig. 6.3b), and the period corresponds to applying a flux quantum to each loop. In the n_g window between the maximums in Fig. 6.3a, the array has two different but degenerate charge configurations that are stable (one excess Cooper pair on the top island, or one on the bottom island in Fig. 6.1a). Similarly, in the f window between the minimums in Fig. 6.3b the array has two different stable phase configurations (a vortex in the left or the right loop), that are also degenerate. We will show that a study of the positions of the maximums and minimums in the critical current (Fig. 6.4) yields information about the array's ground state, and that this can be used to demonstrate superpositions of the degenerate charge and vortex states.

Until now superposition states have only been demonstrated in the most rudimental Josephson junction systems. Superpositions of single-charge states have been observed in systems with a single island [1, 2, 3], but such systems do not have multiple stable vortex configurations. In single loops with Josephson junctions, superpositions of persistent-current states have been demonstrated [4], but these systems are insensitive to the background charges and the two current states do not correspond to vortices at different geometric positions in an array. Our array has both charge and vortex characteristics, and our experiment links superconducting single-charge effects with vortex physics in larger arrays. In these larger systems, a small magnetic field induces vortices that behave as particles. The array's total Josephson energy is minimized for a certain distribution of vortices, where each vortex has a well-defined position. The charging energy, on the other hand, favors a state with a well-defined number of Cooper pairs on each island, in which the charges are localized and the junction phases have large quantum fluctuations. Background charges polarize each island, and this determines which Cooper-pair distribution has the lowest energy. The duality between these two pictures has drawn much attention (for a recent review see [5]). It has been supported by the observation of superconductor-to-insulator transitions, and several localization and quantum-interference effects in two-dimensional and quasi-one-dimensional arrays [5]. However, these studies have been limited by the fact that the charging effects could not be fully controlled: The background charges are in practice strongly disordered, and charge configurations with unpaired quasiparticles usually play a role.

6.2 Description of the array

We present results from three arrays, denoted by 1–3 (the same arrays and numbering as in Ref. [6], where experimental details have been reported). The islands are coupled to each other and to macroscopic leads by identical junctions that have Josephson coupling $E_J = \frac{\hbar}{2e} I_{co}$ and charging energy $E_C = e^2/2C$ (where I_{co} the critical current and C the capacitance of the junctions). We estimated E_J and E_C from the current-voltage characteristic and electron-microscope inspection [6]. Microwave spectroscopy yielded a better estimate for C for arrays 2 and 3 [7]. Array 1 had $E_J = 71\,\mu$eV and $E_J/E_C = 0.48 \pm 0.1$. Array 2 and array 3 (fabricated on the same chip and nominally identical) had $E_J = 31\,\mu$eV and $E_J/E_C = 0.27 \pm 0.03$. Measurements on array 3 were most accurate, and we will emphasize these results.

The arrays had Al-Al_2O_3-Al tunnel junctions and were fabricated with e-beam lithography and shadow-evaporation techniques. The junctions had an area of about $0.015\,\mu\text{m}^2$ and $C \approx 0.7\,$fF. The loops had an area of $1\,\mu\text{m}^2$. Measurements were carried out in a dilution refrigerator with rfi-feedthrough filters at room temperature and copper-powder filters at the temperature of the sample (10–70 mK). The arrays were current-biased (I_{bias}) in a low-impedance environment with a small but non-vanishing damping. The current-voltage characteristic had a clear supercurrent branch (Fig. 6.2a) , and the bias current I_{SW} where it switches from the supercurrent branch was used as a measure for the theoretical value of the array's critical supercurrent I_C [1].

Measurements of I_{SW} as a function of the voltages on the two gate electrodes showed a modulation that was $2e$ periodic in the induced charges (Fig. 6.2b). This shows that unwanted parity effects from unpaired quasiparticles were almost completely suppressed [6]. Previous studies of small two-dimensional arrays were hindered by these parity effects [8]. The observed honeycomb pattern in Fig. 6.2b was used to tune the gates to values where they compensate the influence of background charges in the tunnel barriers or the substrate with an accuracy of about 1 % [6]. The charge frustration n_g is thus defined as $n_g = C_g(V_g - V_{off})/2e$, where $C_g \ll C$ the gate capacitance, V_g the voltage on the gate electrode, and V_{off} the gate voltage that compensates the influence of background charges. We will concentrate here on symmetrically polarized islands, $n_{g1} = n_{g2}$, denoted by n_g. The critical current is periodic with period 1 in f and n_g, and we will therefore restrict ourselves to frustration values between 0 and 1.

The array's Hamiltonian is the sum of the Josephson and electrostatic energies

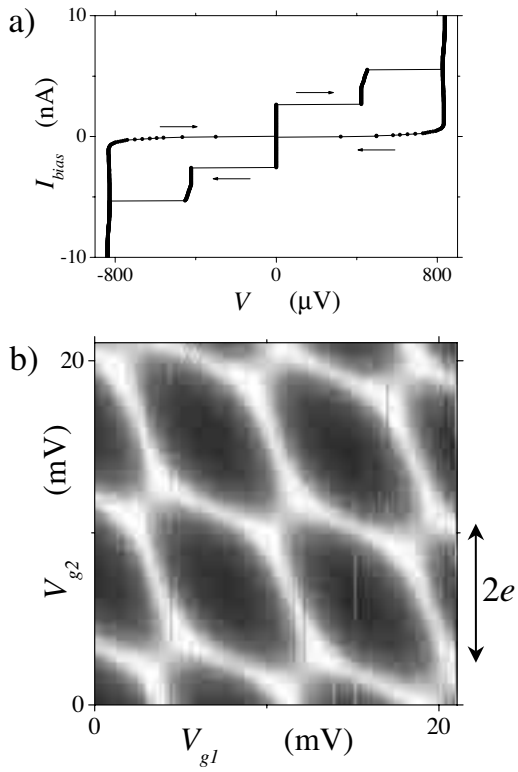

Figure 6.2: **a)** Current-voltage characteristic measured on array 3. Arrows indicate the direction of the hysteretic cycle. **b)** Gray scale plot of switching currents I_{SW} vs. gate voltages V_{g1} and V_{g2}, measured with $f = 0$ and $T = 70mK$ on array 3 (black is 0 nA, white is 6 nA, 250,000 switching events). The I_{SW} modulation is $2e$ periodic in the induced gate charges.

and has been worked out by Lafarge *et al.* [9]. The two loops have a very small self inductance, such that the fluxoid-quantization conditions for each loop act as constraints on the junctions' gauge-invariant phase coordinates γ_i. The system has three degrees of freedom and we use generalized coordinates that are sum and difference coordinates of the junction phases: $\varphi_1 = \frac{1}{2}(\gamma_1 - \gamma_2)$, $\varphi_2 = \frac{1}{2}(\gamma_3 - \gamma_4)$ and $\delta = \frac{1}{2}(\gamma_1 + \gamma_2 + \gamma_3 + \gamma_4)$, with the junctions numbered as in Fig. 6.1a (the direction of positive current is in each branch from left to right or from top to bottom). These variables have conjugate charge coordinates with commutation

relations $[\varphi_1, n_1] = i$, $[\varphi_2, n_2] = i$ and $[\delta, k] = i$. Here n_1 and n_2 are the number of excess Cooper pairs on the top and bottom island respectively, and k is the number of Cooper pairs that has been transferred through the array. The phase δ can thus be considered as the phase difference across the array, and φ_1 and φ_2 can be considered the phases of the two islands. The array's low-impedance environment with small damping causes δ to behave like a classical phase coordinate. The island coordinates have underdamped dynamics, and due to the low island capacitance both the charges (n_1, n_2) and the phases (φ_1, φ_2) are quantum variables. The bias current is related to δ by $I_{bias} = \frac{2e}{\hbar}\frac{\partial E_g}{\partial \delta}$, where E_g is the array's ground-state energy. I_C is the maximum of I_{bias} with respect to δ, and a measurement of I_C thus provides information about the ground state.

6.3 Results

Measurements of I_{SW} as a function of n_g (Fig. 6.3a) show a minimum at $n_g = 0$. At this point the array's electrostatic free energy E_{el} is lowest for the charge state $|n_1, n_2\rangle = |0, 0\rangle$ (if the array is in the zero-voltage state it is independent of k). This state is coupled to consecutive charge states, which allows for a supercurrent to flow. However, other charge states have a higher E_{el} (Fig. 6.1b), and charge fluctuations are suppressed. Here the Coulomb blockade of the supercurrent [10, 1, 2] is most effective and causes the minimum in I_{SW}. When increasing n_g from 0 to 1, the charge state with lowest E_{el} is first $|0, 0\rangle$, then $|0, 1\rangle$ and $|1, 0\rangle$ (degenerate), and near $n_g = 1$ it is $|1, 1\rangle$ (solid lines in Fig. 6.1b). For $C_g \ll C$ the transitions are at $n_g = \frac{3}{8}$ and $n_g = \frac{5}{8}$. Near these points the Coulomb blockade effects are minimal and there are maximums in I_{SW}. More interestingly, near the maximums the array switches from having a single state $|n_1, n_2\rangle$ with the lowest E_{el}, to a situation where two degenerate charge states have the lowest E_{el}. The ground state should be very sensitive to such a transition since it is a superposition of states $|n_1, n_2\rangle$ with the highest amplitudes for the $|n_1, n_2\rangle$ with lowest E_{el} [10, 1, 2].

We observed that the positions of the maximums in I_{SW} versus n_g depend on f. The positions of the maximums are the result of a competition between two effects. For n_g values around $n_g = \frac{1}{2}$, the ground state is close to the form $(|0, 1\rangle + |1, 0\rangle)/\sqrt{2}$, and has an eigen energy that is about $E_J/2$ lower than E_{el} due to the coupling of the central junction. Increasing E_J of the central junction results therefore in a larger n_g window where the ground state is of this form, and the distance between the maximums becomes larger as well. On the other

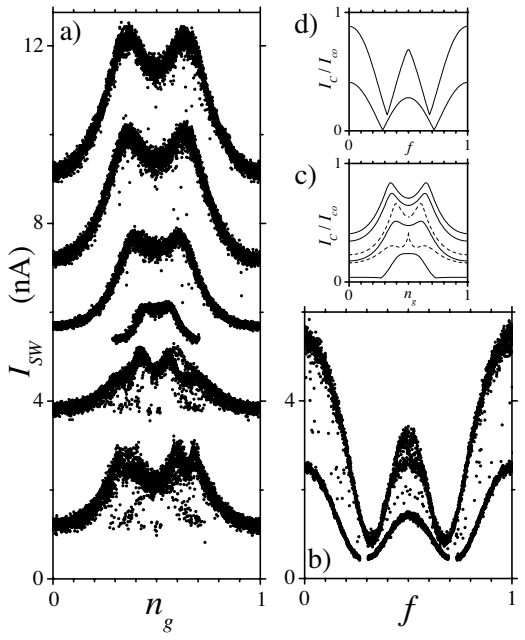

Figure 6.3: **a)** I_{SW} vs. n_g, for (top to bottom) $f = 0$ to $f = 0.5$ in steps of 0.1 (data 7 nA, 5.5 nA, 5 nA, 5 nA, 3 nA and no offset). **b)** I_{SW} vs. f, for $n_g = 0.36$ (top, 0.25 nA offset) and $n_g = 0$ (bottom, no offset). Data from array 3. The data points with low I_{SW} where $n_g \approx \frac{1}{2}$ and $f \approx \frac{1}{2}$ are due to residual parity effects [6]. Data points for very low I_{SW} are absent since they could not be recorded, $T = 70mK$. In **c)** and **d)** simulated I_C in units of I_{co} for $E_J/E_C = 0.27$. Solid lines in c) are for (top to bottom) $f = 0$, 0.1, 0.2, 0.3, and dashed (bottom to top, -0.05 offset) for $f = 0.4$, 0.5. In d) curves for $n_g = 0$ (bottom) and 0.36 (top, 0.05 offset).

hand, these two charge state are also coupled to the $|0,0\rangle$ and $|1,1\rangle$ states by the junctions 1–4. This results in the level repulsion at $n_g = \frac{3}{8}$ and $n_g = \frac{5}{8}$, as in Fig. 6.1b. Increasing E_J of the junctions 1–4 enhances the level repulsion, which causes the maximums in E_g to approach $n_g = \frac{1}{2}$ or to merge into one maximum. The maximums in I_C follow this pattern. For our array, the two effects are in balance for $f = 0$ (Fig. 6.3a). Increasing f from zero induces a persistent current in the array that flows through the outer branches of the array, i. e. through junctions 1–4, but not through the central junction. The switching current measures the array's ground state at finite bias current. The combination

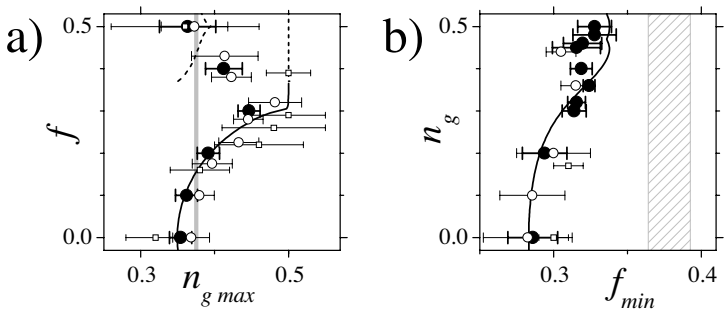

Figure 6.4: Measured and simulated positions of maximums in I_{SW} vs. n_g, and minimums in I_{SW} vs. f. Data from array 1 (squares), 2 (open circles) and 3 (solid circles). Errors bars indicate the uncertainty in absolute positions of maximums and minimums, uncertainty in the shifts of positions in one measured trace with respect another is about one order smaller. In **a)** positions of maximums $n_{g\,max}$ from data as in Fig. 6.3a, for different f. In **b)** positions of minimums f_{min} from data as in Fig. 6.3b, for different n_g. Solid black lines show simulated values for $E_J/E_C = 0.27$, the black dashed parts in a) represent the fact that I_C develops for $f \gtrapprox 0.37$ an additional peak structure. Gray areas indicate where $n_{g\,max}$ and f_{min} are expected for classical charging and Josephson effects.

of I_{bias} and the persistent current breaks the symmetry in the effective Josephson coupling for the top and the bottom island. For the bottom island, the bias current is compensated by the persistent current, while for the top island the bias current and the persistent current add up and reduce the effective Josephson coupling $-E_J \cos\gamma_i$ of junction 1 and 2. The overall effect is that the array has a lower I_{SW} due to the weak effective E_J in the upper branch, but that the strong coupling in the lower branch causes the two maximums to merge into a single maximum with increasing f. Around $f = 0.3$ a vortex enters the array (see also below), and at $f = 0.5$ the symmetry is restored since the flux-induced currents now lead to an equal reduction of the effective E_J for the two islands. Numerical calculations (as described in [9, 11]) of I_C (Fig. 6.3c) and the positions $n_{g\,max}$ of the maximums (Fig. 6.4a) agree very well with the measurements for $f \lessapprox 0.35$. For $f \gtrapprox 0.35$, the I_{SW} data is less reliable due to residual parity effects [6] that suppress I_{SW} at places where the maximums are expected (lower two traces in Fig. 6.3a).

Similarly, the critical current as a function of f was studied. We will first

analyze the case with $I_{bias} = 0$. For $f = 0$, the array's total Josephson energy U_J is lowest for $|\delta, \varphi_1, \varphi_2\rangle = |0, 0, 0\rangle$ (Fig. 6.1c,d). This corresponds to a phase configuration without vortices in the array, and it will be denoted as $|0, 0\rangle_v$. When increasing f from 0 to 1, the phase configuration with lowest U_J is for $0.364 < f < 0.636$ one of the two degenerate states $|\delta, \varphi_1, \varphi_2\rangle = \big|\pi, \pi \pm (f - \frac{1}{2})\pi, \mp(f - \frac{1}{2})\pi\big\rangle$, as indicated by the solid lines in Fig. 6.1c and the double-well potential in Fig. 6.1e (equivalent solutions exist for $\delta = -\pi$, the classical behavior of δ enforces one of the two cases). These states with $\delta = \pi$ correspond to phase configurations with a single vortex in the array [9], i. e. with a vortex in the right or the left loop. In Fig. 6.1c these two states are denoted as $|0, 1\rangle_v$ and $|1, 0\rangle_v$. For $f > 0.636$, the array returns to a vortex-free phase configuration with $\delta = 0$, but now with about one flux quantum induced in each loop, and this state can thus be denoted as $|1, 1\rangle_v$. At points close to $f = 0.364$ and $f = 0.636$, the band E_g versus δ has minimum amplitude, and δ can easily make multiple transitions of π. This leads to minimums in I_{SW} (Fig. 6.3b).

In the f window around $f = \frac{1}{2}$, the underdamped quantum behavior of φ_1 and φ_2 allows for tunnelling between the two classical solutions at the minimums in U_J in Fig. 6.1e. Moreover, comparison with U_J in Fig. 6.1d shows that φ_1 and φ_2 are here less confined. The f window in which the array's ground-state energy with $\delta = \pi$ is lower than that for $\delta = 0$ is therefore expected to be wider than the classical boundaries $f = 0.364$ and $f = 0.636$, see also Fig. 6.1c (for finite bias currents the classical boundaries move towards $f = \frac{1}{2}$, up to $f = 0.393$ and $f = 0.607$ for $I_{bias} = I_C$). The minimums in Fig. 6.3b are clearly further apart than expected classically. Moreover, the positions of the minimums f_{min} depend on n_g. Due to the classical behavior of δ (i. e. no coherent coupling to a vortex reservoir outside the array) we can interpret the positions of the minimums here directly as the point where the array makes the transition between a ground state without a vortex in the array and a ground state that is a superposition of the $|0, 1\rangle_v$ and $|1, 0\rangle_v$ state. A shift of the f_{min} corresponds to a shift of the position of this transition.

The shift of f_{min} is analyzed in a picture where the state of the array is analogous to a particle in a two-dimensional periodic potential [10]. The U_J in Fig. 6.1d is a unit cell for $\delta = 0$ and Fig. 6.1e for $\delta = \pi$. The influence of n_g becomes evident in a tight-binding description. This has been worked out in Ref. [11] for a system with a similar Hamiltonian. For $\delta = \pi$ the terms that couple one of the classical solutions with neighboring states is of the form $-t_1 - \sum_j t_2 \mathrm{e}^{i\mathbf{k}\cdot\mathbf{a}_j}$, where t_1 the coupling from intra-unit cell coupling, and the

sum over terms t_2 for inter-unit cell coupling. The length of the $\mathbf{k}$ vector is equal to n_g, and $\mathbf{a}_j$ is the position vector to the nearest-neighbor site. For $\delta = 0$, as in Fig. 6.1d, there is only inter-unit cell coupling. The coupling terms to the nearest-neighbor states are $-\sum_j t_3 \mathrm{e}^{i\mathbf{k}\cdot\mathbf{a}_j}$. The $\delta = \pi$ ground state will have a minimum energy for $n_g = 0$. Non-integer values of n_g cause a phase difference between t_1 and inter-unit cell coupling, and lead to a higher eigen energy. As a result the f window where $\delta = \pi$ becomes smaller. This effect dominates the shift in f_{min} since the array has $t_1 > t_2 > t_3$. For $n_g \approx \frac{3}{8}$, where Coulomb blockade effects are minimal, the minimums have moved in the direction where f_{min} is expected for classical behavior. An analysis with finite bias current is more tedious, but the overall picture remains valid. Numerical calculations of I_C (Fig. 6.3d) and the positions of the minimums f_{min} (Fig. 6.4b) agree again very well with the observations. From the observed positions and shifts of f_{min} we conclude that the array has around $f = \frac{1}{2}$ a ground state that is a superposition of two vortex states.

In conclusion, the experimental results in this chapter illustrate the duality between the charge and vortex description of two-dimensional quantum arrays of Josephson junctions. Superpositions of single-charge states and vortex states occur in the array in a dual fashion. When the coulomb blockade effects are partly lifted, the vortex behavior approaches the result for the classical Josephson effect. Tuning of the effective Josephson energy with a small magnetic field modulates the single-charge effects in a similar way. The results are in very good agreement with numerical simulations. The environmental impedance of the array has a significant influence on the level of the switching currents, and it can slightly renormalize the ratio of E_J/E_C [12]. However, our results are not based on a study if the amplitude of the switching current, but on the positions of maximums and minimums in the switching current. The observed phenomena are therefore very robust against the influence of environmental effects.

We thank P. Lafarge, M. H. Devoret, K. K. Likharev, T. P. Orlando, Y. Nakamura, P. Hadley, R. N. Schouten and C. J. P. M. Harmans for fruitful discussions, and the Dutch FOM for financial support.

References

[1] P. Joyez *et al.*, *Phys. Rev. Lett.* **72**, 2458 (1994).

[2] M. Matters, W. J. Elion, and J. E. Mooij, *Phys. Rev. Lett.* **75**, 721 (1995).

[3] Y. Nakamura, Yu. A. Pashkin, and J. S. Tsai, *Nature* **398**, 786 (1999).

[4] J. R. Friedman *et al.*, *Nature* **406**, 43 (2000); C. H. van der Wal *et al.*, *Science* **290**, 773 (2000).

[5] R. Fazio and H. S. J. van der Zant, to be published in *Phys. Rep.* (2001); cond-mat/0011152.

[6] C. H. van der Wal and J. E. Mooij, *J. Supercond.* **12**, 807 (1999).

[7] C. H. van der Wal, P. Kuiper, and J. E. Mooij, *Physica B* **280**, 243 (2000). These results were measured on array 2 at a later stage. During sample storage the junction resistance had increased from 21 kΩ to 28 kΩ.

[8] W. J. Elion, J. J. Wachters, L. L. Sohn, and J. E. Mooij, *Phys. Rev. Lett.* **71**, 2311 (1993); V. Bouchiat, Ph. D. thesis, Université Paris 6, 1997.

[9] P. Lafarge, M. Matters, and J. E. Mooij, *Phys. Rev. B* **54**, 7380 (1996). We found a missing factor 2 in the numerical code used for this article, the figures are for $E_J/E_C = 0.4$ instead of $E_J/E_C = 0.2$.

[10] D. V. Averin and K. K. Likharev, in *Mesoscopic Phenomena in Solids*, edited by B. L. Al'tshuler, P. A. Lee, and R. A. Webb (Elsevier, Amsterdam, 1991), Chap. 6.

[11] T. P. Orlando *et al.*, *Phys. Rev. B* **60**, 15398 (1999).

[12] P. Joyez, Ph. D. thesis, Université Paris 6, 1995.

Chapter 7

Quantum transitions of a small Josephson junction array

Abstract

We have experimentally studied a small Josephson junction array in the presence of microwave irradiation. The array has comparable energy scales for single-charge effects and the Josephson effect, resulting in a discrete set of macroscopic eigen-energy levels. Excitation of the array by low-power microwaves is possible at frequencies where the photon energy matches the level spacing. The microwave frequency and amplitude dependence show that the excitation mechanism involves resonant quantum dynamics of the array.

7.1 Introduction

In circuits of extremely underdamped Josephson junctions, discrete energy levels (DEL) are the result of the quantum mechanical interplay of the Josephson effect and the single-Cooper pair charging effect. The two effects are orthogonal. We study here such a system with comparable Josephson energy and charging energy. In this regime, the system can then be looked at as the equivalent of a particle, with a mass proportional to the junction capacitance C, whose phase coordinate γ (the phase degree of freedom of the Josephson junction) is confined by the Josephson potential $-E_J \cos\gamma$. Alternatively, the systems can be looked at as a network of islands with a high charging energy, with eigen states that

This chapter is based on Ref. 4 on p. 111.

are close to single-charge states of the islands. Due to the Josephson effect, the islands can exchange Cooper pairs. The systems has a discrete set of eigen states in both of these pictures. Recently the DEL of a device with a single superconducting grain coupled to leads via tunnel junctions have been demonstrated in experiments using microwave spectroscopy [1, 2, 3]. With such a circuit excited to a superposition of two energy states coherent charge oscillations have been observed [4].

7.2 Results

Here we study the quantum transitions between DEL of the array depicted in Fig. 7.1 [5, 6]. This experiment was performed on array 2 from Chapter 5. However, the experiment was performed at a later stage, and the junction quality had degraded. During sample storage the junction resistance had increased from 21 kΩ to 28 kΩ. We believe that this mostly affected the Josephson energy of the junction, and that the capacitance values that are derived from spectroscopy data in this chapter can be used for the accurate analysis of Chapter 6. Also, much more parity effects, of the type discussed in Chapter 5, were present in the data. Due to these parity effects the accurate tuning of the influence of offset charges, as in Chapter 5, was no longer possible. In this experiment, the influence of offset charges could be compensated with about 5% accuracy.

For the junctions the ratio of the Josephson coupling E_J to the energy scale for single-charge effects $E_C = e^2/2C$ was now estimated to be $E_J/E_C = 0.2$, with $E_C/h = 28$ GHz. The level spacing between the DEL can be tuned continuously by inducing a gate charge $n_g = C_g V_g/2e$ on the islands. The array was studied by measuring the switching current I_{SW} from the supercurrent branch in the IV (effectively the escape of a particle in the tilted washboard potential in Fig. 7.1). This method can be used for spectroscopy since I_{SW} is strongly reduced when the array is in an excited state [1, 2]. Note however that the analysis is complicated. For the ground band the relation $I_{bias} = (2e/\hbar)\partial E/\partial\delta$ between the bias current and the phase difference across the array δ is close to the form $I_{bias} \propto \sin\delta$, as shown in Fig. 7.1. From this picture it is clear that the level spacing ΔE changes, and the resonance condition $\Delta E = hf$ can be met, while adiabatically ramping the current for a switching current measurement.

Fig. 7.2 presents I_{SW} as a function n_g, measured in the presence of CW-microwaves. Additional low levels in I_{SW} around half integer values of n_g are due to the presence of an unpaired quasiparticle on one or both islands, effectively

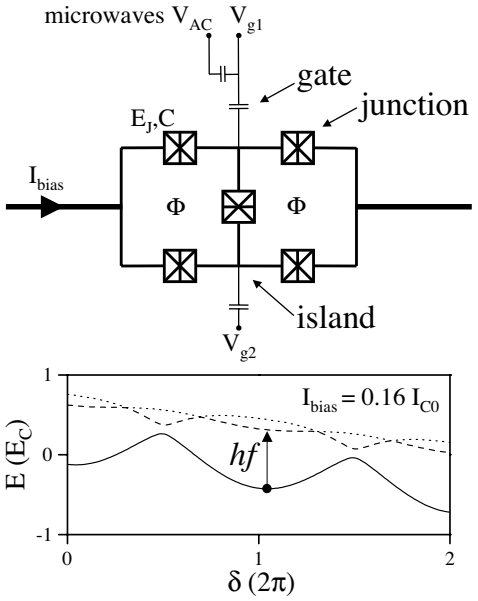

Figure 7.1: Top: Schematic of the array. Here we only consider the case of symmetrically induced gate charges for the top and bottom island $n_g = C_g V_g/2e$, and a magnetic flux $\Phi = 0$ applied to the loops. Bottom: The lowest three bands of the array as a function of the phase δ across the array, here calculated for $E_J/E_C = 0.3$ and $n_g = 0.37$ using [5]. At finite bias current the bands are tilted ($I_{C0} = (2e/\hbar)E_J$).

changing n_g with $\frac{1}{2}$ for that island [6]. Arrows indicate n_g-values where I_{SW} is strongly reduced, which is clearly frequency dependent. The dips move closer to $n_g = 0$ with increasing frequency f, in agreement with a larger level spacing ΔE between the ground state and the first excited state at $n_g = 0$ where Coulomb blockade effects are maximal. For the reasons mentioned above the width of the dips cannot be interpreted as the lifetime of the exed states. When n_g is applied with an asymmetry of $\Delta n_g = 0.15$ the level spacing between the first and second excited state is larger, and transitions to both the first and second excited state could be distinguished.

Measurements of the Bessel function behavior of the Shapiro step heights in the voltage biased IV were used to calibrate the microwave amplitude V_{AC}. This was possible without any change to the array's electromagnetic environment.

This showed that the data of Fig. 7.2 is typically recorded for $V_{AC} < hf/2e$, corresponding to an oscillating matrix element for transitions between the levels that is much smaller than the level spacing. This, together with the clear frequency dependence of the dips, indicates that the excitation mechanism involves resonant quantum dynamics, similar to AC-pulse induced Rabi dynamics in NMR.

We thank Kees Harmans and Terry Orlando for discussions, and the Dutch FOM for support.

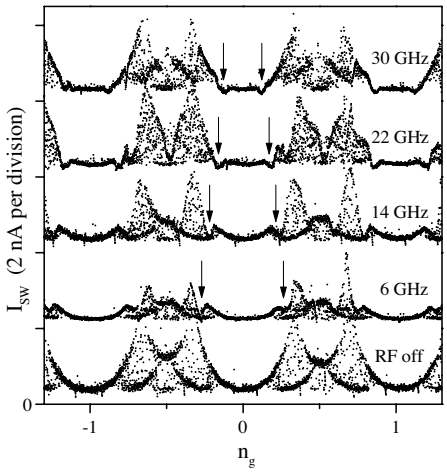

Figure 7.2: Measurements of the $2e$-periodic modulation of the switching current I_{SW} by the dimensionless gate charge n_g, measured with different microwave frequencies, at a temperature of 10 mK. Data sets are 2 nA offset for clarity.

References

[1] D. J. Flees, S. Han, J. E. Lukens, *Phys. Rev. Lett.* **78**, 4817 (1997).

[2] D. J. Flees, S. Han, J. E. Lukens, *J. Supercond.* **12**, 813 (1999).

[3] Y. Nakamura, C. D. Chen, J. S. Tsai, *Phys. Rev. Lett.* **79**, 2328 (1997).

[4] Y. Nakamura, Yu. A. Pashkin, J. S. Tsai, *Nature* **398**, 786 (1999).

[5] P. Lafarge, M. Matters, J. E. Mooij, *Phys. Rev. B* **54**, 7380 (1996).

[6] C. H. van der Wal, J. E. Mooij, *J. Supercond.* **12**, 807 (1999).

Summary

Quantum Superpositions of Persistent Josephson Currents

This thesis presents experimental research on Josephson junction devices that behave quantum mechanically. The devices are formed by micrometer-sized superconducting islands, that are interconnected by a Josephson tunnel junction: a thin insulating layer between two superconductors. With current microfabrication technology, it is possible to make very clean and well-defined junctions. The behavior of such high-quality junctions is defined by two parameters. One is the junction capacitance, which results from the parallel-plate geometry of the tunnel junctions. The second is the junction's Josephson coupling energy, which is a measure for the tunnel coupling between the two superconducting electrodes, and it determines the supercurrent that can flow through the junctions. The supercurrent through the junction is directly related to a phase coordinate of the junction. Circuits with Josephson junctions have charge and current coordinates that are conjugate variables. This leads to quantum mechanical behavior of these devices if the energy scale for the Josephson effect and charging effects are comparable. Due to the superconductivity in these devices, the dynamics is much better decoupled from a dissipative environment than that of other solid-states devices.

The research that is presented in this thesis aimed at investigating whether Josephson junction circuits can have quantum coherent dynamics with a long decoherence time. This question was inspired by three, partly overlapping research themes that are currently of interest in the scientific community. Firstly, if quantum coherent dynamics of Josephson junction circuits could be accurately controlled, these systems would be a promising candidate for realizing a quantum computer. An advantage of a quantum computer based on small Josephson junction circuits is that the technology for expanding such a system to a large-scale integrated computer is already available. Secondly, the current degrees of freedom of these circuits are macroscopic, in the sense that they correspond to the center-of-mass motion of a very large number of microscopic charge carriers.

Josephson junction circuits are therefore unique systems for testing the validity of quantum mechanics at a macroscopic scale. Thirdly, it is very interesting that these devices are artificially fabricated quantum systems. With the technology that is applied, it is possible to engineer and control them in a wide parameter range, and to couple the systems in a controlled manner to environmental degrees of freedom. This allows for detailed research on the boundary between classical and quantum physics, and decoherence.

We report research on two different devices. The first part of this thesis concentrates on a small loop with three Josephson junctions. The second part reports work on a small two-dimensional Josephson junction array with two coupled loops. The two systems have in common, that the loops carry persistent Josephson currents when a small magnetic field is applied to the loops.

The Josephson energy of the three-junction loop forms a double-well potential when the magnetic flux in the loop is close to half a superconducting flux quantum. The states at the bottoms of the two wells correspond to persistent-current states of opposite polarity. This system was realized in the regime where the junctions' Josephson energy was about a factor fifty larger than the energy scale for single-charge effects. For this ratio a subtle balance is struck in this device. The system's charging effects are still significant, and allow for quantum tunneling through the barrier between the two stable persistent-current states. At the same time, this large ratio allows for engineering the system such that it is very insensitive to the influence of background charges in the solid-state environment of the loop. We performed microwave-spectroscopy experiments which demonstrated that this system is an artificially fabricated quantum two-level system; we observed narrow resonance lines that resulted from microwave-induced quantum transitions between the quantum levels. An anti-crossing of the quantum levels proved that quantum superposition states of the two macroscopic persistent-current states occur in this system. The system was measured by placing it in a DC-SQUID magnetometer. The measurement process and the resulting noise is analyzed in detail.

The small two-dimensional arrays were studied in the regime where the energy scales for Josephson effect and single-charge effects were comparable. The arrays had a self-dual geometry: They can be described as two coupled islands with a high charging energy, but also as two coupled loops that can each carry a persistent current. The latter description corresponds to that of an array in which the meshes can contain a vortex. The arrays had a ground state with comparable quantum fluctuations in the charge and Josephson phase due to the

Heisenberg uncertainty relation between these coordinates. In this regime, the devices are very sensitive to the influence of background charges in the environment. However, with capacitively coupled gate electrodes we succeeded in obtaining accurate control over the single-Cooper-pair effects in this system. The Josephson effect could be controlled by applying a small magnetic field to the loops. This allowed for a controlled study of the trade-off between quantum fluctuations in the Josephson phase coordinates and charge coordinates of the array, and our results show that superpositions of charge and vortex states occur in the array in a dual fashion. Microwave spectroscopy experiments were used to demonstrate a discrete set of excited quantum levels in these devices.

From the research that is presented here one can conclude that it is possible to realize well-defined quantum systems with Josephson junction circuits. Quantum superpositions of charge and persistent-current states have been demonstrated, and transitions between quantum levels can be controlled with resonant microwave radiation. These results form a good basis for future experiments that investigate whether quantum coherent dynamics with a long decoherence time can be realized with these devices. This requires quantum-state control with pulsed microwaves. De technology for such experiments, as well as for experiments on circuits that contain multiple coupled quantum systems, is available.

Caspar van der Wal, Delft, June 2001

Samenvatting

Quantum Superposities van Persisterende Josephson-stromen

Dit proefschrift beschrijft experimenteel onderzoek aan schakelingen met Josephson-juncties die zich quantummechanisch gedragen. De schakelingen bestaan uit supergeleidende eilanden ter grootte van enkele micrometers, die onderling verbonden zijn met een Josephson-tunneljunctie: een dunne isolerende laag tussen twee supergeleiders. Met de huidige microfabricagetechnieken is het mogelijk zeer schone juncties te maken, met goed gedefinieerde eigenschappen. Het gedrag van zulke juncties wordt bepaald door twee parameters. Eén is de capaciteit van de junctie, die ontstaat door de parallelle-plaatgeometrie van de junctie. De tweede is de Josephson-koppelingsenergie; een maat voor de tunnelkoppeling tussen de twee supergeleiders. Deze bepaalt hoeveel superstroom door de junctie kan stromen. Deze superstroom is direct gerelateerd aan een fasecoördinaat van de junctie. Schakelingen met Josephson-juncties hebben fase- en ladingscoördinaten die geconjugeerde variabelen zijn. Dit leidt tot quantummechanisch gedrag van deze schakelingen als de energieschalen voor het Josephson-effect en ladingseffecten van dezelfde orde zijn. Door de supergeleiding in deze schakelingen, is de dynamica veel beter ontkoppeld van een dissipatieve omgeving dan voor de meeste vaste-stofschakelingen het geval is.

Het in dit proefschrift beschreven onderzoek was gericht op de vraag of Josephson-junctieschakelingen quantumcoherente dynamica kunnen hebben, met een lange decoherentietijd. Het beantwoorden van deze vraag draagt bij aan drie, elkaar gedeeltelijk overlappende onderzoeksthema's die nu in de belangstelling staan in de wetenschappelijke gemeenschap. Ten eerste zouden deze systemen een veelbelovende kandidaat zijn voor het realiseren van een quantumcomputer als quantumcoherente dynamica van Josephson-junctieschakelingen met grote precisie gecontroleerd zou kunnen worden. Een voordeel van een quantumcomputer op basis van deze schakelingen is, dat de technologie voor het uitbreiden van een dergelijk systeem tot een grote geïntegreerde quantumcomputer al beschikbaar is. Ten tweede zijn de stroomvrijheidsgraden van deze schakelingen macro-

scopisch; de stroom is het resultaat van de massa-middelpuntsbeweging van een zeer groot aantal microscopische ladingsdragers. Josephson-junctieschakelingen zijn daarom unieke modelsystemen om de geldigheid van quantummechanica voor macroscopische objecten te testen. Ten derde is het feit dat het kunstmatig gefabriceerde quantumsystemen zijn erg interessant. De gebruikte technologie staat toe de eigenschappen van de schakelingen in een groot parameterbereik te construeren, te controleren en te koppelen aan omgevingsinvloeden. Dit maakt deze systemen zeer geschikt voor onderzoek naar de grens tussen de klassieke- en quantumfysica en decoherentie.

We beschrijven onderzoek aan twee verschillende schakelingen. Het eerste deel van dit proefschrift richt zich op een kleine supergeleidende ring met daarin drie Josephson-juncties. Het tweede deel behandelt werk aan een klein tweedimensionaal Josephson-junctienetwerk, dat bestaat uit twee gekoppelde ringen met juncties. In de ringen van beide systemen treden persisterende Josephson-stromen op als een klein magneetveld wordt aangelegd in de ringen.

De Josephson-energie van de ring met drie juncties vormt een dubbele-putpotentiaal als de magnetische flux in de ring in de buurt van een half supergeleidend fluxquantum is. De toestanden op de bodems van de twee putten corresponderen met persisterende-stroomtoestanden van tegenovergestelde polariteit. Dit systeem was gerealiseerd met junctieparameters waarbij de Josephson-energie ongeveer een factor vijftig groter was dan de energieschaal voor enkele-ladingseffecten. Voor deze verhouding is een subtiele balans gerealiseerd in deze schakeling. De ladingseffecten in het systeem zijn nog steeds significant, en quantumtunnelen door de barrière tussen de twee stabiele persisterende-stroomtoestanden is mogelijk. Tegelijkertijd kan bij deze grote verhouding van de energieschalen het systeem zo worden geconstrueerd dat het zeer ongevoelig is voor de invloed van achtergrondladingen in de vaste-stofomgeving van de ring. Met microgolf-spectroscopie-experimenten is aangetoond dat dit systeem een kunstmatig gefabriceerd quantum-twee-niveausysteem is; we hebben zeer nauwe resonantie lijnen waargenomen die het gevolg zijn van microgolf-geïnduceerde quantumovergangen tussen de quantumniveaus. Een afstoting van de quantumniveaus toonde aan dat quantum superpositietoestanden van de macroscopische persisterende-stroomtoestanden in dit systeem voorkomen. Metingen aan het systeem werden verricht door het in een DC-SQUID-magnetometer te plaatsen. Het meetproces en de resulterende ruis zijn geanalyseerd.

De kleine tweedimensionale netwerken zijn bestudeerd in het regime waar de energieschalen voor het Josephson-effect en enkele-ladingseffecten van gelijke

grootte waren. De netwerken hadden een zelfduale geometrie: Ze kunnen worden beschreven als twee gekoppelde eilanden met een hoge ladingsenergie, maar ook als twee gekoppelde ringen die ieder een persisterende stroom kunnen dragen. De tweede beschrijving correspondeert met die van een netwerk waarvan de mazen een vortex (wervelstroom) kunnen bevatten. Deze netwerken hadden een grondtoestand met quantumfluctuaties van vergelijkbare grootte in de ladingen en fasen van de juncties, door de Heisenberg-onzekerheidsrelatie tussen deze coördinaten. In dit regime zijn de schakelingen erg gevoelig voor de invloed van achtergrondladingen in de omgeving. Met capacitief gekoppelde gate-elektrodes is echter nauwkeurige controle over de enkele-Cooper-paareffecten in dit systeem gerealiseerd. Het Josephson-effect kon worden gecontroleerd door een klein magneetveld in de ringen aan te brengen. Hierdoor kon de balans tussen quantumfluctuaties in de Josephson-fasecoördinaten en de ladingscoördinaten van het netwerk nauwkeurig worden gecontroleerd en bestudeerd. De resultaten tonen aan dat superposities van ladings- en vortextoestanden op duale wijze voorkomen in deze netwerken. Microgolf-spectroscopiemetingen zijn gebruikt om aan te tonen dat deze netwerken overgangen kunnen maken naar geëxciteerde quantumniveaus.

Op basis van het hier beschreven onderzoek kan worden geconcludeerd dat met Josephson-junctieschakelingen goed gedefinieerde quantum systemen kunnen worden geconstrueerd. Quantum-superpositietoestanden van ladings- en persisterende-stroomtoestanden zijn aangetoond, en overgangen tussen quantumniveaus kunnen worden gecontroleerd met resonante microgolfstraling. Deze resultaten vormen een goede basis voor vervolgexperimenten die uitsluitsel moeten geven over de vraag of langdurige quantumcoherente dynamica kan worden gerealiseerd met deze systemen. Hiervoor moeten de quantumtoestanden worden gecontroleerd met gepulste microgolven. De technologie voor dergelijke experimenten, en voor het realiseren van experimenten aan een aantal gekoppelde quantumsystemen, is beschikbaar.

Caspar van der Wal, Delft, juni 2001

Curriculum vitae

Caspar H. van der Wal

6 Feb. 1971	Born in Hengelo (Ov.), the Netherlands.
1983-1989	VWO at the Bataafse Kamp in Hengelo (Ov.).
1989-1990	Fulbright exchange student at Slippery Rock University, USA.
1990-1996	M.Sc. in Applied Physics at Delft University of Technology. Graduate research in the Solid State/Quantum Transport group of prof. dr. ir. J. E. Mooij. Subject: Superconducting single-charge effects in small Josephson junction devices.
1996	Student research internship at Stanford University, USA, in the group of Prof. Y. Yamamoto. Subject: Manipulating and measuring quantum fluctuations in a small Josephson junction circuit.
1996-2001	Ph.D. research at Delft University of Technology in the Solid State/Quantum Transport group of prof. dr. ir. J. E. Mooij. Subject: Quantum superpositions of persistent Josephson currents, a research project aimed at realizing quantum coherent dynamics and quantum computation with Josephson junction devices.

List of publications

1. *Controlled single-Cooper-pair charging effects in a small Josephson-junction array*
   Caspar H. van der Wal, J. E. Mooij, *J. Superc.* **12**, 807 (1999).

2. *Josephson persistent-current qubit*
   J. E. Mooij, T. P. Orlando, L. Levitov, Lin Tian, Caspar H. van der Wal, Seth Lloyd, *Science* **285**, 1036 (1999).

3. *Superconducting persistent-current qubit*
   T. P. Orlando, J. E. Mooij, Lin Tian, Caspar H. van der Wal, L. S. Levitov, Seth Lloyd, J. J. Mazo, *Phys. Rev. B* **60**, 15398 (1999).

4. *Quantum transitions of a small Josephson-junction array*
   Caspar H. van der Wal, P. Kuiper, J. E. Mooij, *Physica B* **280**, 243 (2000).

5. *Decoherence of the superconducting persistent-current qubit*
   Lin Tian, L. S. Levitov, J. E. Mooij, T. P. Orlando, Caspar H. van der Wal, Seth Lloyd, in *Quantum Mesoscopic Phenomena and Mesoscopic Devices in Microelectronics*, I. O. Kulik, R. Ellialtioğlu, eds. (Kluwer Academic Publishers, Dordrecht, 2000), pp. 429–438; cond-mat/9910062.

6. *Quantum superposition of macroscopic persistent-current states*
   Caspar H. van der Wal, A. C. J. ter Haar, F. K. Wilhelm, R. N. Schouten, C. J. P. M. Harmans, T. P. Orlando, Seth Lloyd, J. E. Mooij, *Science* **290**, 773 (2000).

7. *Macroscopic quantum superposition in a three-Josephson-junction loop*
   Caspar H. van der Wal, A. C. J. ter Haar, F. K. Wilhelm, R. N. Schouten, C. J. P. M. Harmans, T. P. Orlando, Seth Lloyd, J. E. Mooij, submitted to *the MQC2-workshop proceedings*, Naples, 14–17 June 2000.

8. *Macroscopic quantum superposition of current states in a Josephson-junction loop*
   F. K. Wilhelm, C. H. van der Wal, A. C. J. ter Haar, R. N. Schouten, C. J. P. M. Harmans, J. E. Mooij, T. P. Orlando, Seth Lloyd, submitted to *Sov. Phys. Usp.*, conference proceedings of *"Mesoscopic and strongly correlated electron systems"*, Chernogolovka, 9–16 July 2000.

9. *Dual charge and vortex superpositions in a small Josephson-junction array*
   Caspar H. van der Wal, J. E. Mooij, submitted to *Phys. Rev. Lett.* (2001).

10. *Engineering decoherence in Josephson persistent-current qubits: Measurement apparatus and other electromagnetic environments*
    Caspar H. van der Wal, F. K. Wilhelm, C. J. P. M. Harmans, J. E. Mooij, in preparation for *Eur. Phys. J. B* (2001).

11. *Solid start for solid-state quantum bits* (perspective)
    Caspar van der Wal, Leo Kouwenhoven *Physics World* **12**, 21 (July 1999).